Computer assisted development and optimization of a variable dielectric barrier discharge

Dissertation zur Erlangung des akademischen Grades
Doktor-Ingenieur (Dr.-Ing.) der Fakultät für Informatik und
Elektrotechnik der Universität Rostock

vorgelegt von
Robert Bansemer, geb. am 01.03.1991 in Bergen aus Greifswald

Rostock, 05.02.2020

https://doi.org/10.18453/rosdok_id00002782

Tag der Einreichung: 12.02.2020
Tag der Verteidigung: 30.09.2020

Gutachter:
Prof. Dr. Ursula van Rienen, Universität Rostock
Prof. Dr. Klaus-Dieter Weltmann, Universität Greifswald
Prof. Dr. Gerrit M.W. Kroesen, Technische Universiteit Eindhoven

Abstract

Physical plasmas are used in biomedical applications to combine a multitude of active agents in order to influence the treated biological system. The promotion of healing of chronic wounds by decontaminating them and actively re-initiating and stimulating the endogenous healing mechanism is one important application area besides others. Although wound healing application of physical plasmas is already established in certain clinics' daily routine, further development and understanding of the background is desirable. This is motivated especially by the circumstance that wound healing is both a very individual and a very dynamic process. Furthermore, plasma treatment routines in this field are not standardized up to now, which makes approval and reimbursement by health insurance providers more difficult.

In the frame of the present work, the aim of enhancing biomedical applications of plasma is addressed by complementing the range of available plasma source concepts by a new approach. Contrary to most established devices, the solution introduced here focuses on the production of reactive oxygen and nitrogen species (RONS) as the only active agents. This qualifies the device not as a basis to aim for a certification for clinical practice, but rather for basic biomedical research. While for the former field of application, the restriction to RONS is not desirable in the first place, the latter can benefit from an unelaborate handling, a robust control mechanism and the potential for further, demand-based enhancements.

The device is based on a dielectric barrier discharge operated in ambient air at reduced pressure. This allows the generation of either an ozone-dominated output gas chemistry or an exclusive production of nitrogen oxides including nitric oxide. Gas pressure and temperature have found to be the dominating factors controlling the output gas composition. Furthermore, crucial chemical processes for the ozone- to nitric oxide-transition have been identified using a plasma chemical model. The model also revealed that a constructive coupling of pressure and flow rate as realized in the presented concept improves the response of key reactions to pressure changes.

For enhancing the practical usability of the identified plasma chemical process control mechanisms, an electrical diagnostics method tracking the gas temperature has been developed. It overcomes the difficulty in determining the gas temperature in a fully-integrated device even without gas flow. The approach used to realize this diagnostics is the connection between temperature and voltage drop over the discharge. A laboratory prototype implementing the investigated concept and the developed diagnostics has been designed and manufactured as a technology demonstrator to conclude the project.

Zusammenfassung

Physikalische Plasmen werden in biomedizinischen Anwendungen genutzt, um kombiniert über mehrere Mechanismen auf das zu behandelnde biologische System einzuwirken. Zu den wichtigsten Anwendungsgebieten zählt die Förderung der Heilung chronischer Wunden durch Dekontamination und aktive Wiedereinleitung und Stimulation der endogenen Heilungsmechanismen. Obwohl physikalische Plasmen für Wundheilungsanwendungen bereits Einzug in den Alltag einiger Kliniken gehalten haben, ist eine weitere Entwicklung und Erforschung zugrundeliegender Mechanismen wünschenswert. Das folgt vorrangig daraus, dass Wundheilung sowohl sehr individuell als auch sehr dynamisch abläuft. Außerdem sind Plasmaprozesse in diesem Anwendungsbereich bisher nicht standardisiert, was die Zulassung und die Kostenerstattung durch Krankenkassen erschwert.

Die vorliegende Arbeit verfolgt das Ziel der Weiterentwicklung biomedizinischer Anwendungen von Plasmen, indem die Auswahl der verfügbaren Plasmaquellenkonzepte um einen neuen Ansatz ergänzt wird. Im Gegensatz zu den meisten etablierten Geräten legt die hier vorgestellte Lösung den Schwerpunkt auf eine Produktion reaktiver Sauerstoff- und Stickstoffspezies (RONS) als einziger bereitgestellter Wirkstoff. Das legt eine Nutzung durch Anstreben einer klinische Zulassung weniger nahe, die vordergründige Eignung besteht für Anwendungen in der biomedizinischen Forschung. Während die Beschränkung auf RONS in der klinischen Nutzung kaum anzustreben ist, profitieren Laboruntersuchungen von unkomplizierter Handhabung, einem robusten Steuerungsverfahren und dem Potenzial für bedarfsabhängige Erweiterungen.

Das Gerät basiert auf einer dielektrischen Barriereentladung, die in Umgebungsluft bei reduziertem Druck betrieben wird. Das ermöglicht die Erzeugung einer Ozon-dominierten Gaszusammensetzung, aber auch eine ausschließliche Produktion von Stickoxiden einschließlich Stickstoffmonoxid. Druck und Temperatur des Prozessgases zeigten sich als dominierende Faktoren zur Steuerung der produzierten Gaszusammensetzung. Darüber hinaus wurden die entscheidenden chemischen Prozesse für den Übergang von der Ozon- zur Stickstoffmonoxidproduktion durch Nutzung eines plasmachemischen Modells identifiziert. Das Modell zeigt außerdem, dass die im untersuchten Konzept vorherrschende konstruktive Kopplung von Druck und Gasflussrate das Ansprechen der wesentlichen Reaktionen auf Druckänderungen unterstützt.

Um die praktische Nutzbarkeit der aufgezeigten plasmachemischen Kontrollmechanismen zu verbessern, wurde eine elektrische Diagnosemethode zur Messung der Gastemperatur entwickelt. Diese überwindet die Schwierigkeit der Gastemperaturmessung in einem voll-integrierten Gerät auch ohne Gasfluss. Der verwendete Ansatz zur Umsetzung des Diagnoseverfahrens ist der Zusammenhang von Temperatur und Spannungsabfall über der Entladung. Ein Funktionsmuster, das das untersuchte Konzept und die entwi-

ckelte Diagnostik implementiert, wurde als Technologiedemonstrator zum Abschluss des Projekts konstruiert und gefertigt.

Danksagung

Über die lange Zeit, die die Verwirklichung der vorliegenden Arbeit in Anspruch genommen hat, konnte ich immer auf umfassende Unterstützung zählen. Besonders danke ich Prof. Dr. Ursula van Rienen für das in mich gesetzte Vertrauen und die Begleitung meiner Promotion an der Universität Rostock von der Anfangsphase über das Zulassungsverfahren bis hin zur vorliegenden Monografie. Sehr positiv bleibt auch das Engagement von Prof. van Rienen für die Einbeziehung meiner Beiträge in die jährlichen Treffen ihrer Arbeitsgruppe in Erinnerung.

Für die exzellente fachliche Betreuung meiner Arbeit von Seiten des INP Greifswald danke ich Prof. Dr. Klaus-Dieter Weltmann. Auch im INP durfte ich auf ein einladendes und innovationsfreundliches Arbeitsumfeld treffen, wofür ich meinen Kolleginnen und Kollegen sowie Prof. Weltmann als Institutsdirektor danke. Besonders hervorheben möchte ich, wie sehr Diskussionen mit Dr. Jörn Winter und Dr. Ansgar Schmidt-Bleker immer wieder dazu beigetragen haben, dass aus Überlegungen Konzepte und später Lösungen wurden. Eine von Ansgars vielen Ideen hat die Grundlagen, auf denen diese Arbeit aufbaut, überhaupt erst geschaffen.

Für die Bereitschaft, meine mehr oder weniger gut vorbereiteten Probevorträge zu ertragen, danke ich meinem Bürokollegen und guten Freund Alexander Pogoda. Die Gespräche zwischen Alex und mir, die durch Kaffee beflügelt von Schreibtisch zu Schreibtisch geführt wurden, brachten öfter tragfähige Ideen und Lösungen hervor. Die eher durch Bier hinterfütterten Gespräche, die wir an Samstagen geführt haben, waren diesbezüglich nicht immer genau so ergiebig, wurden deshalb aber nicht weniger von mir geschätzt. Meine fast drei Jahre dauernde Tätigkeit als Doktorandensprecher des INP an der Seite von Katja Zocher ist gelegentlich wirklich in Arbeit ausgeartet, hat aber trotzdem Spaß gemacht. Dafür entscheidend war die großartige Zusammenarbeit mit Katja, ihre Ideen und ihre Bereitschaft, diese auch über Hindernisse hinweg umzusetzen. Dabei waren wir uns nicht immer einig, wovon unsere Vorhaben oft profitiert haben.

Mein Dank für die praktische Umsetzung meiner Zeichnungen, Pläne und fixen Ideen gilt der mechanischen Werkstatt des INP um Peter Gransow. Dabei halfen regelmäßig auch Diskussionen im Voraus, technologisch sinnvolle Lösungen einzuplanen und so Fehlversuche zu vermeiden. Für die umfassende Unterstützung beim Erstellen des Platinenlayouts für das Funktionsmuster zur Arbeit danke ich dem INP-Elektroniklabor um Norbert Lembke.

Letzte hilfreiche Anregungen nach Fertigstellung der Arbeit von meinem Kollegen Ansgar und meinem Partner Per-Ole habe ich dankbar angenommen. Beide haben korrekturlesenderweise kleinere Unzulänglichkeiten wie Tippfelher aufgedeckt. Über fachliche Aspekte hinaus danke ich meinen Eltern Bianca und Uwe für den Rückhalt über die gesamte Zeit meines Studiums und meiner Promotion.

Contents

List of Acronyms

ADC	analog-digital converter
API	application programming interface
CAP	cold atmospheric plasma
CE	*conformité européenne*, european conformity
CFD	computational fluid dynamics
DBD	dielectric barrier discharge
DUT	device under test
EU	European union
FEM	finite element method
FTIR	Fourier-transform infrared
FVM	finite volume method
IR	infrared
LCD	liquid-crystal display
MPC	multi-pass cell
OES	optical emission spectroscopy
QCLAS	quantum cascade laser absorption spectroscopy
RNS	reactive nitrogen species
RONS	reactive oxygen and nitrogen species
ROS	reactive oxygen species
RF	radio frequency
SI	*système international d'unités*, international system of units
TDLAS	tunable diode laser absorption spectroscopy
UART	universal asynchronous receiver-transmitter
UV	ultra-violet
VDBD	Venturi-dielectric barrier discharge
VEDF	vibrational energy distribution function

List of Symbols

Symbol	Unit	Description
a	m^{2}	area
A	m^{-1}Pa^{-1}	Gas constant to interpolate α
$A(\tilde{\nu})$	1	absorbance
$a(\tilde{\nu})$	m^{2}	absorptivity
A_c	m^{2}	geometric cross section
$a_i(\tilde{\nu})$	m^{2}	absorptivity of species i
A_r	m^{3}s^{-1}* m^{6}s^{-1}†	reaction rate scaling parameter
b	V	voltage axis intercept
B	Vm^{-1}Pa^{-1}	Gas constant to interpolate α
$B(\tilde{\nu})$	Vm	single-beam spectrum
c	ms^{-1}	speed of light
C	1	arbitrary constant
$\tilde{c}$	m^{-3}	concentration
c_cal	VKPa^{-1}	calibration constant
C_cell	F	cell capacitance
C_d	F	capacitance of dielectrics
C_g	F	gas gap capacitance
$\tilde{c}_i$	m^{-3}	concentration of species i
c_p	JK^{-1}	specific heat capacity at constant pressure
d	m	absolute value of distance
$\vec{d}$	m	distance
$D(\delta)$	1	interferometer boxcar function
e	C	elementary charge
E	J	energy
$\vec{E}$	Vm^{-1}	electric field
E_0	Vm^{-1}	norm of external electric field
E_a	J	activation energy
E'	Vm^{-1}	electric field norm caused by electron avalanche
e_cgs	g$^{1/2}$cm$^{3/2}$s^{-1}	elementary charge, explicitly stated in cgs units
$\mathcal{F}$		Fourier transform operator
f	m	perimeter
f_i		i-th basis function coefficient
$f(\vec{r})$		function of the location

* 2nd order reactions

† 3rd order reactions

Symbol	Unit	Description
$f(v)$	1	electron velocity distribution
$f(\tilde{\nu})$	1	interferometer sinc function
g	$\mathrm{ms^{-2}}$	gravitational acceleration
$\vec{g}$	N	gravity
$G(S)$		gain term compiled from S
h	Js	Planck constant
$\tilde{h}$	$\mathrm{Wm^{-2}K^{-1}}$	heat transfer coefficient
H	J	enthalpy
i	1	index
$I(\tilde{\nu})$	W	radiation intensity
$I_0(\tilde{\nu})$	W	background radiation intensity
k	$\mathrm{m^3s^{-1}}$	electron collision rate coefficient
$\tilde{k}$	$\mathrm{Wm^{-1}K^{-1}}$	heat conductivity
$k(T)$	$\mathrm{m^3s^{-1}}{}^{*}$ $\mathrm{m^6s^{-1}}{}^{\dagger}$	heavy particle collision rate coefficient
k_B	$\mathrm{JK^{-1}}$	Boltzmann constant
l	m	absorption length
L	m	characteristic length
$\tilde{L}$		arbitrary operator
$L(S)$		loss term compiled from S
n	1	reaction rate curvature parameter
$\vec{n}$	1	normal vector
N	$\mathrm{m^{-3}}$	particle density
$\tilde{N}$	1	number
$\tilde{N}_0$	1	initial number
$\mathrm{Nu_L}$	1	Nusselt number
p	Pa	pressure
$\vec{p}$	Cm	dipole moment
q	C	charge
$\vec{q}$	$\mathrm{Wm^{-2}}$	heat flux
Q	$\mathrm{m^3s^{-1}}$	gas flow rate
$Q(t)$	C	external charge
Q_diag	C	charge values on diagonal through Q(V)-plot
q_max	C	maximum transferred charge
Q_max	C	maximum external charge
Q_min	C	minimum external charge
r	m	radius
$\tilde{r}$		residual
$\vec{r}$		location
R	$\mathrm{JK^{-1}mol^{-1}}$	gas constant
$R(t)$	Ω	time-dependent resistance
$\mathrm{Ra_L}$	1	Raleigh number
Re	1	Reynolds number

* 2nd order reactions

† 3rd order reactions

Symbol	Unit	Description
$s(\vec{r})$		source term
S		species density set
$\mathbf{S}$	$\mathrm{s^{-1}}$	velocity gradient
$S(\delta)$	V	interferogram signal
t	s	time
T	K	gas temperature
$T(\tilde{\nu})$	1	transmittance
T_{cal}	K	calibration temperature
T_{ext}	K	ambient temperature
t_{R}	s	residence time
$\vec{u}$	$\mathrm{ms^{-1}}$	flow velocity
U	$\mathrm{ms^{-1}}$	average flow velocity norm
u_{b}	V	burning voltage
$u_{\mathrm{g}}(t)$	V	gas gap voltage
$\overline{u_{\mathrm{g}}}$	V	average gas gap voltage in active phase
$u_{\mathrm{g,ext}}$	V	gas gap voltage at discharge extinction
u_{char}	V	characteristic voltage
v	$\mathrm{ms^{-1}}$	velocity
$V(t)$	V	external voltage
v_{d}	$\mathrm{ms^{-1}}$	electron drift velocity
V_{max}	V	maximum external voltage
V_{min}	V	minimum external voltage
w	$\mathrm{CV^{-1}}$	charge weighting factor
w_i		i-th weighting function
x	m	path
X		arbitrary species in reaction set
x_{a}	m	start of path
x_{b}	m	end of path
α	$\mathrm{m^{-1}}$	Townsend's coefficient for ionization
α_{m}	$\mathrm{s^2A^2m^{-1}kg^{-1}}$*	material coefficient
β_{m}	$\mathrm{s^2A^2m^{-3}kg^{-1}}$†	material coefficient
γ	1	secondary electron emission coefficient
δ	m	path difference
$\tilde{\delta}$	1	Kronecker delta
Δ	m	maximum path difference
ϵ	1	emission coefficient
η	Pas	dynamic viscosity
λ	m	wavelength
μ_{e}	$\mathrm{m^2V^{-1}s^{-1}}$	electron mobility
$\tilde{\nu}$	$\mathrm{m^{-1}}$	wavenumber
ρ	$\mathrm{kgm^{-3}}$	mass density
$\sigma(v)$	$\mathrm{m^2}$	cross section

* exemplarily for a transversal electromagnetic wave, equals $\mathrm{mH^{-1}}$

† exemplarily for a transversal electromagnetic wave, equals $\mathrm{Fm^{-1}s^{-2}}$ or $\mathrm{Sm^{-1}s^{-1}}$

τ	Pa	shear stress
φ_i		i-th basis function
Ω		domain for computation

1. Introduction and objective

Electrical facilities and devices have increasingly been affecting daily life since the 19$^{\text{th}}$ century. Some notable examples are the gradual establishment of communication systems and electrical lighting. The telegraph was invented in the early 1830s [1], and in the second half of the 19$^{\text{th}}$ century, the telephone came up as a more modern alternative. First switching centers were found in New York in 1877/78 and Paris 1879, although the system could hardly gain acceptance in the beginning [2]. Also in 1879, the incandescent bulb had been improved to reach a reliability that made it suitable for practical application [3]. The large-scale usage of lightbulbs was made possible 1882, when the first direct current electrical power plant was put into operation in New York [1, 3]. The development of the marketable incandescent bulb and a standardized system of generators, cables, meters, sockets and switches designed for 110 V DC were closely linked to each other. Around the same time, patents pioneering for a more flexible AC based system were originally issued in Europe. They provided the basis for a serious technological and commercial competitor to the incompatible DC system only a few years later, and eventually prevailed against DC based solutions for most application scenarios. The competition between DC and AC based systems for electrical power distribution was the prototype for a multitude of following rivalries about prevalent technical standards from the viewpoints of technology, economy and marketing [3]. From this period of time on, inventions relying on electricity have distinctly been improving quality of living.

Beyond that, electrical engineering soon started to make life not only more comfortable, but in average also longer. In Germany, life expectancy at birth in the year 1820 was comparably high for that time: It was 41 years, while the life expectancy in France was lower with 37 years, in Italy only 30 years could statistically be expected. Since that time, the life expectancy has increased significantly. In 1900, it ranged from 43...47 years for the three mentioned countries, to rise further to 77...78 years in 1999 [4]. The multitude of factors influencing this development justifies a dedicated field of research, however one of the aspects behind this pleasant trend was facilitated by electrical engineering and marked the advent of an interdisciplinary cooperation of electrical engineering with medicine and chemistry.

An example from Berlin, Germany, in the year 1866 reveals the background: 5457 people died from cholera, that was 0.8 % of the town's overall population. Cholera outbreaks occasionally happened at that time, the last major epidemic in Germany was 1892 in Hamburg [5]. Contaminated drinking water was one of the major propagation mechanisms for the disease, consequently sand filters for the drinking waters helped curbing the spread of cholera. Obviously, the efficiency of such filters is too limited to permanently ensure high hygienic standards. Chlorine based sewage water decontamination has been introduced in Hamburg in 1893 in one plant to control a typhoid epidemic

- it's not like cholera was the only problem. Later, the technique was adapted also for fresh water decontamination [6]. It is distinctly more effective than sand filters, but chlorine is an environmental toxin whose existence in the drinking water is undesirable as well. Therefore, the introduction of a new technology for an efficient, residue-free water decontamination was necessary.

1.1. Plasmas for decontamination and medicine

A brief historical overview

In 1907 in Nice, France and in 1910 in St. Petersburg, Russia, the first facilities for large-scale fresh water treatment based on ozone (O_3) were installed [7,8]. These systems were based on the dielectric barrier discharge (DBD) principle, that was known since 1857 as a device to produce O_3 [9], shortly after ozone was discovered and named [10]. By now, thousands of DBD-based large-scale ozone generators are in use, primarily for water treatment [11].

To form the basis for this, a thorough investigation and characterization of DBDs was performed. One notable step in this process was for example the inquiry of information about the influence of gas velocity, input voltage and frequency on the produced O_3 concentration in 1922 [12]. Ten years later, the segmentation of the discharge process in air DBDs in individual microdischarges was verified experimentally using photographic plates [13]. In the subsequent decade in 1943, it was found that a sinusoidally driven air DBD runs through two active and two inactive ("dark") phases during one voltage period, where the voltage drop over the gas gap u_g is approximately constant during the active phases. Moreover, the electrical diagnostic using the Q-V-plot ("Lissajous figure") to obtain effective capacitances and the dissipated power was introduced [14]. The successive investigation and enhancement of DBDs for the production of chemical species continues up to date [15–18] and yields enhancements both for the classical operation [19–21] and special operation modes such as the homogeneous DBD [22]. On the whole, DBDs have occupied a multitude of applications and processes to date [7,11,17,23,24].

Recent applications

Retrospectively, the application of DBDs for generating ozone figuratively speaking "fired the starting pistol" for the development of further applications of non-thermal plasmas. While ozone was already primarily used to decontaminate water, the ability to inactivate microorganisms was used in later applications as well. A notable step towards a usage on a broader field of applications is the decontamination of non-conducting, non-biological surfaces and containers that was patented in 1968 [25]. As a further development, a selective impact on living cells was made possible later, allowing an application on living tissue as well.

Nowadays, different concepts relying on plasmas near ambient temperature, summarized as cold atmospheric plasma (CAP) sources, are established for several related applications on this field: Sterilization (elimination of all microorganisms and their dormant stages), disinfection (inactivation of elimination of microorganisms, less effective than sterilization), decontamination (cleansing from microorganisms or unwanted material) and regulation of inflammatory processes in living tissue [26–33]. As a technological basis, DBDs ignited in a volume or in a surface are used as well as jet plasmas and microwave driven plasmas. Using any of these technologies, reactive oxygen and nitrogen species (RONS) play a key role to achieve the desired effects in synergy with ultraviolet (UV) radiation, electric fields and accumulated charge [26, 27, 31–34]. Remarkable examples for RONS are O_3, various nitrogen oxides (NO_x) as well as hydrogen peroxide (H_2O_2). Among different CAP sources, the composition and concentration of produced RONS differs significantly. Depending on the concept in use, either NO_x or oxygen species such as atomic oxygen (O), singlet oxygen (O_2*) or O_3 can be dominant [35–40].

Treatment concepts allowing an effective inactivation of bacteria can be developed based on both an O_3 and a NO_x dominated plasma chemistry [41], however a NO_x-dependent inactivation is only efficient in acidic conditions. This motivates the assumption that the actual disinfective effect in such a case is caused by peroxynitrous acid (ONOOH) that is formed from NO_x depending on the pH value [42–45].

An application of any device in clinical practice in the EU requires a CE-certification as a medical device *and* the verification of the desired biomedical effects by clinical trials and systematic case reports. Three devices fulfilling both requirements are commercially available as of 2018, namely the kINPen® MED (neoplas tools GmbH, Greifswald, Germany), the Adtec SteriPlas (Adtec Plasma Technology, Adtec Europe, Hunslow, UK) and the PlasmaDerm® (CINOGY GmbH, Duderstadt, Germany).

The kINPen® is an argon jet working with a radio frequency (RF) voltage of about 1 MHz that is pulsed at 2.5 kHz in the MED version. Although it is working with argon as well, the SteriPlas implements a substantially different concept. It forms a plasma torch using a 2.45 GHz microwave signal [46]. As a DBD with the treatment target as the second electrode, the PlasmaDerm® works in the open atmosphere with voltage pulses of up to 10 kV at a repetition rate of 300 Hz [47].

Plasma medicine provides remarkable biomedical effects such as a decrease of bacterial load in chronic wounds [48, 49] and an influence on mammalian cells, e.g. a stimulation of tissue regeneration [32]. However, it has only recently left its research-only state for clinical applications. The kINPen® MED as the first jet device with a CE-certification as a medical device became available in 2013. A recently developed standard for plasma medical treatments to ensure safety of and provide comparability between different devices using different technological approaches is DIN SPEC 91315. The standardized requirements include patient leakage current, temperature, thermal output, UV radiation and antimicrobial efficacy [50].

1.2. Concept and objective

Plasma medical treatment concepts by now rely on devices that operate with parameters that are fixed to a great extent [46]. This allows generating a well-defined and reproducible composition of therapeutically active agents. However, the present devices do not allow an adaption of the treatment parameters to realize a multi stage treatment.

Advantages from adaptive parameters could arise for the treatment of chronic wounds such as diabetic leg ulcers. The fluids in these ulcers typically feature pH values above 6 [51, 52]. This suggests using a decontamination based on an O_3 dominated chemistry, because the pH is too high to effectively produce ONOOH from NO_x that could otherwise be used as well. A treatment step supporting the actual wound healing could follow in the decontaminated environment, however O_3 cannot be expected to be effective for this task. Now, a production of NO_x seems more expedient because in particular NO is involved in cell communication and wound healing. Moreover, it can be anti-inflammatory and limit cell apoptosis [32, 33]. This motivates the development of a plasma source concept that is capable of providing either an O_3 or a NO_x dominated chemistry. The latter can be generated in an air discharge or by a noble gas plasma jet, where the surrounding air is crucial for RONS production [53].

A shielding gas device for a noble gas jet has been developed in the recent past that allows tuning the produced species composition. This is achieved by specifically influencing reaction pathways leading to the formation of species via tuning the available educt concentration. It performs excellent in tuning the species output, but requires both a noble gas and a shielding gas from a bottle or similar source [35, 54]. Another known approach with similar complexity is tuning power, gas composition and flow rate in a noble gas jet [55]. For the user, an operation independent from bottled gases would be a substantial advantage.

Without requiring any externally supplied gas except ambient air, the “portable microwave air plasma” can produce either O_3 or NO. Therefore, the latter device already reaches the primary goals that are to be met with the concept under development. Its efficiency to promote healing of artificial, acute wounds has been shown already [56]. Developing an alternative concept based on a completely different technological approach is still seen as desirable for an application as a basis to develop effective multi-stage treatment concepts for chronic wounds.

To allow an optimal treatment in such cases, an enhancement of the operating parameters given by the basic device could be desirable. As an example, an admixture of additional humidity to the process gas could promote the formation of ONOOH [57]. Different device concepts feature distinct differences in their suitability to include enhancements as proposed in the example, therefore the availability of an alternative technological approach is desirable.

For an efficient production of ozone, DBDs are not the only, but the most proven and established plasma source concept. Devices reaching high gas temperatures such as microwave plasma torches [58] or spark discharges [59] can efficiently produce NO. In DBDs in air, NO can be detected in the active zone as well, but it reacts rapidly with O_3 to NO_2 and O_2 [60]. If the formed amount of O_3 is higher than the amount of NO, all of the latter will be converted in a few seconds. Under certain circumstances, it is possible that the formed NO concentration is high enough to convert all O_3, eventually leading to the presence of NO after the reaction [41].

The production of NO and its subsequent reaction with O_3 is well known for ozonizers

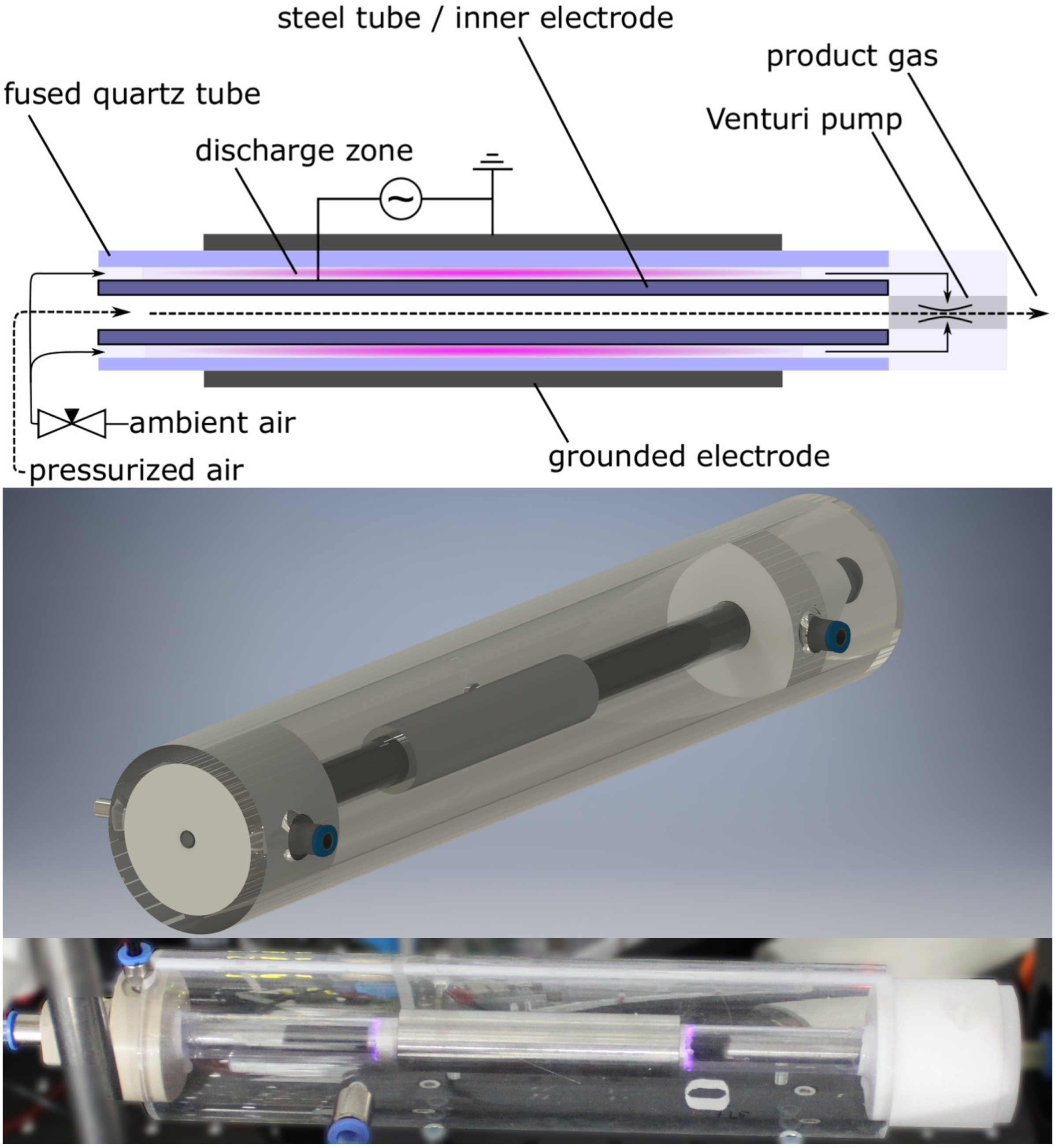

Figure 1.1.: First, coaxial prototype of the VDBD with integrated Venturi pump. Sketch taken with permission from [16], © IOP Publishing Ltd.

and named “discharge poisoning”. This poisoning effect is less pronounced for higher values of pressure [61]. By implication, a controlled further reduction of pressure should promote the NO_x poisoning and, at a certain point, even lead to a domination of produced NO_x over O_3. This could serve as a basis for a device that can be instantaneously switched from an O_3 to a NO production without requiring a supply of bottled gases.

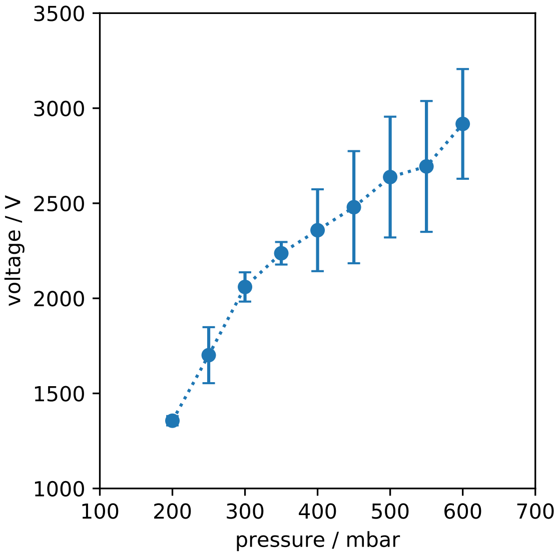

Figure 1.2.: Breakdown voltage for different pressure values. Taken with permission from [16], © IOP Publishing Ltd.

Initial prototype

A primary aspect of the concept under development is the operation at reduced process gas pressure. As a flexible, economic and robust means to decrease the gas pressure, a Venturi pump is used. The first prototype is set up coaxially with a built-in Festo VN-05-H Venturi pump as shown in figure 1.1. At the inlet, an adjustable Festo GRO-QS-6 throttle valve causes a pressure drop. This design allows an operation in a pressure range of 200...600 mbar, while the minimum voltage for operation increases with high pressure as shown in figure 1.2. In the center of the device, the main gas flows through an 8 mm thick stainless steel tube to the pump. The tube is used as the powered electrode that is cooled by the inner gas flow to enhance the usable power range for continuous operation. A tube of fused quartz confines the process chamber to the outside and acts as a dielectric barrier preventing an arc discharge. It has an inner diameter of 11 mm, resulting in a process chamber width of 1.5 mm. Another stainless steel tube with a length of 88 mm outside the dielectric is used as a ground electrode.

At the output of the device, a mixture of the processed gas and the driving gas for the Venturi pump streams out. This has two essential consequences: First, the obtainable concentration of species is limited due to the dilution of the processed gas. Second, the output gas remains close to ambient temperature also in the case that the processed gas experienced a certain temperature increase in the active zone. The dilution is not a major issue for the design. Due to the spatially separated species production, power density or temperature in the active zone can be increased to compensate for the dilution without any concern about harming the treatment target. In contrast, the low output gas temperature does have a practical implication: It allows applications directly at living tissue where heating or a temperature above 40 °C is not necessarily tolerable.

A high-voltage source being appropriately powerful to make use of these options was utilized, namely the HVGEN10AC v3.1 from Voltagezone Electronics. This flyback transformer-based module is fed with a direct voltage, but lacks a respective built-in

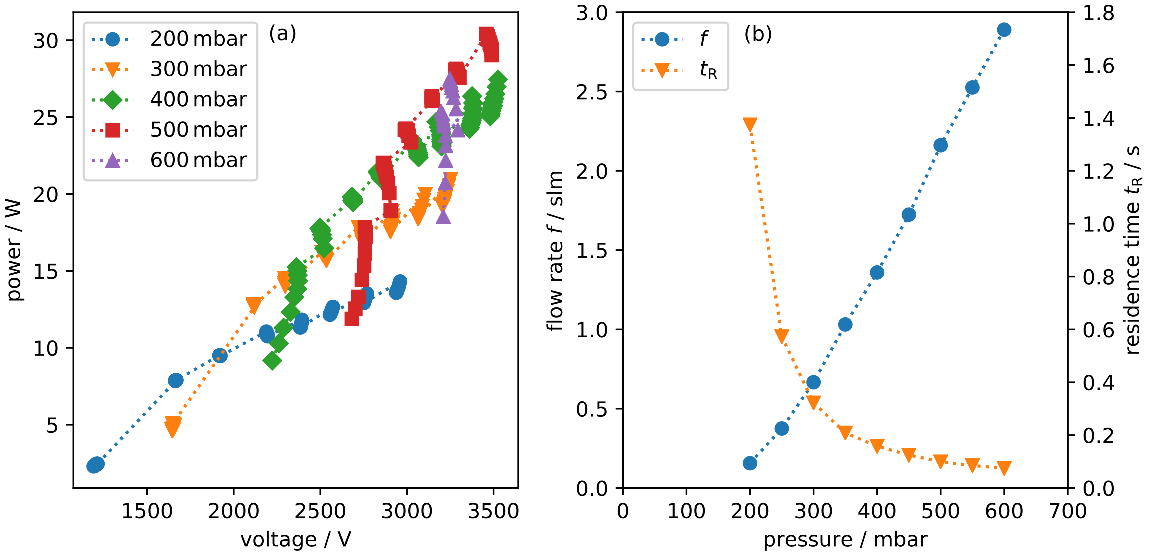

Figure 1.3.: (a) Correlation between voltage amplitude and dissipated power in the first prototype, (b) Correlation between pressure and gas flow and the resulting residence time in the active zone. Taken with permission from [16], © IOP Publishing Ltd.

supply. Instead, it can be used with ordinary PC-controlled laboratory voltage supplies, allowing a straightforward inclusion in PC-based control algorithms. The device provides a sinusoidal signal with a frequency of about 30 kHz and an amplitude of up to 13 kV_{pp} at a maximum power rating of 50 W.

To operate the Venturi pump with peak efficiency, a main gas pressure of 5.5 bar is used. This leads to a flow of pressurized air of 11 standard liters per minute (slm). The correlation between gas pressure and flow in the process chamber was measured using a Leybold CTR 100 pressure sensor and a Brooks Instruments ball flow meter. In figure 1.3, the obtained results are depicted together with the correlation between voltage amplitude and dissipated power. The latter quantities were determined using two Tektronix P6015A high voltage probes, one for the electrode voltage measurement and one to measure the voltage drop over a 1 nF capacitor in the ground line. A Tektronix DPO 2024B oscilloscope was used to capture the signals and provide them to a PC where they were processed with an algorithm explained in chapter 2.4.2.

Prototype optimized for simulations

The prototype presented before is suitable to demonstrate the VDBD concept and to serve as a device under test (DUT) for basic investigations. For a more detailed analysis including computational fluid dynamics (CFD) simulations, the complicated design however does not seem appropriate, at least not as a starting point. For this reason, a simple, horizontally and vertically almost completely symmetric device as shown in

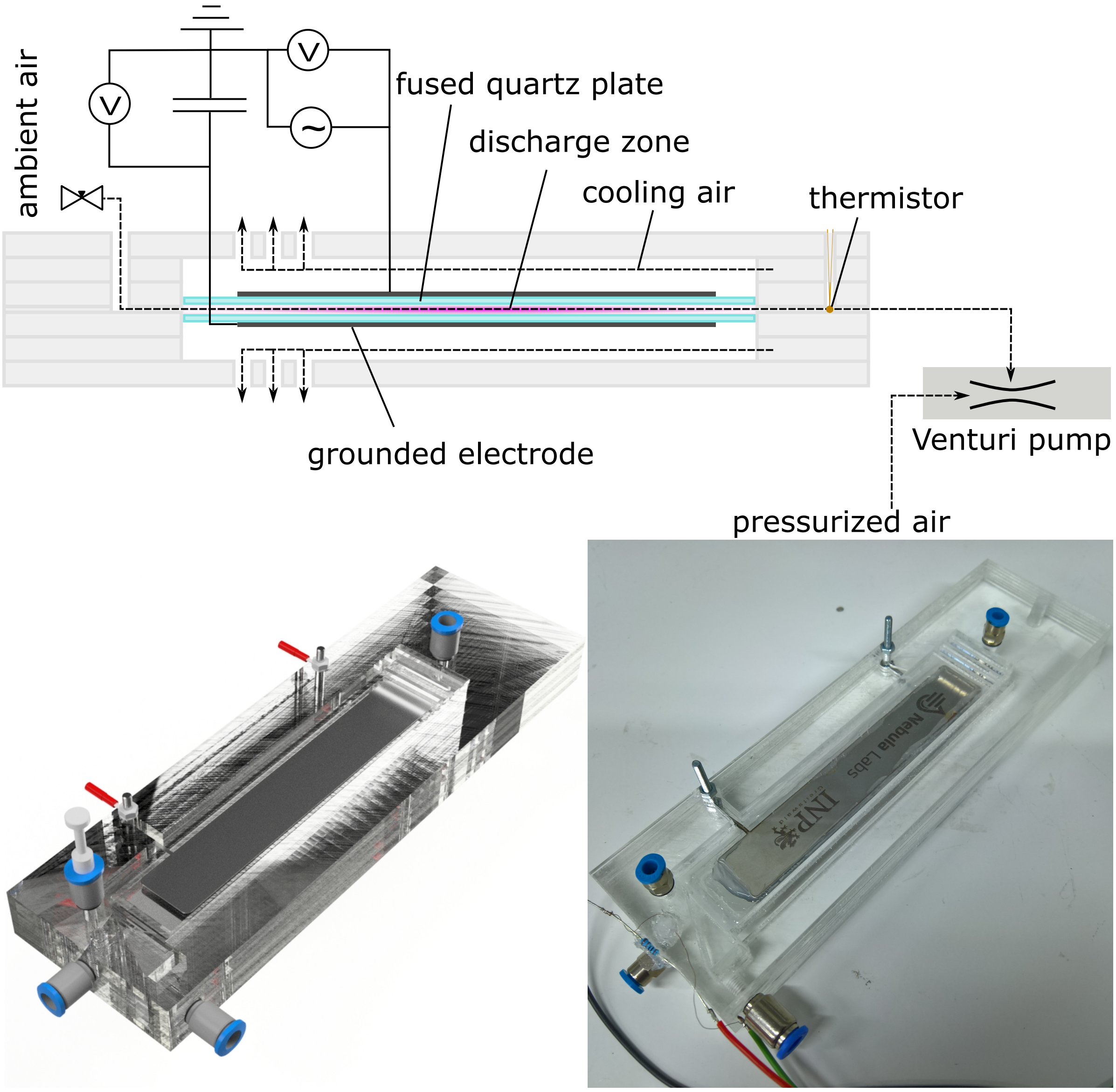

Figure 1.4.: Planar prototype design optimized for simulations. The Venturi pump is not embedded anymore, and a thermistor allows verifying calculated temperature values. Sketch taken with permission from [62], © IOP Publishing Ltd.

figure 1.4 has been designed. In addition to provide a means for detailed investigations, this device version is intended to evaluate a manufacturing method that could potentially be used for a later, more sophisticated prototype. Therefore, all essential parts are designed planar and have been manufactured using a laser cutter. This includes the electrodes made from 0.3 mm thick stainless steel, dielectrics made of fused quartz with a thickness of 2 mm and a poly(methyl methacrylate) (PMMA) housing. The latter consists of several parts with a material thickness of 3 mm each. Ethyl acetate is used to solvate the plate surfaces and therefore to allow joining them together to a sandwich-like module. The mechanical connection between dielectrics and electrodes is ensured by applying silicone sealant.

An integration of a Venturi pump is not provided in this version, instead an external Vaccon VP00-060H module can be connected. Both the throttle valve at the inlet and the electrical equipment have been transferred from the initial prototype with only a minor adaption: The usage of a 10 nF capacitor in the ground line causes a voltage drop low enough to be measured with a standard Tektronix TPP0200 voltage probe. In the initial prototype, a capacitance that is lower by a factor of 10 requires a high-voltage probe instead. A second TPP0200 probe is used to determine the voltage drop over the built-in TDK B57540G1 thermistor that is connected in series to a fixed resistor and a 5 V power supply. The oscilloscope has been upgraded to a Tektronix DPO 4104 in order to allow a more convenient operation, although the sample rate was retained at 1 GS/s to provide an appropriate ratio of record length and captured time.

Using these two setups, the VDBD concept will be investigated regarding its ability to produce either an O_3 or a NO_x-dominated output gas composition. Strategies to control the chemical output as well as a technical implementation will be developed. Established methods of reaction kinetics modeling, absorption spectroscopy and electrical measurements and circuit modeling will be applied to obtain the necessary data. Thus, the foundation for the presented project is a good knowledge of the state of the art and a sound understanding of relevant methods.

2. Technological background and state of the art

In order to allow elaborating an expedient strategy for calculations and measurements, basic considerations about available techniques and methods are necessary. Experimental results will be used as a starting point for all investigations. Generated concentrations of RONS such as O_3 and NO need to be measured reliably, therefore this section presents physical principles and their implementation to obtain this data. Subsequently, the generation of RONS from air is outlined both from a plasma chemical and a technological point of view.

2.1. Molecules and their interaction with radiation

Atoms and molecules can absorb electromagnetic radiation of certain wavelengths λ. The corresponding energy $E = hc/\lambda$ transferred during these processes is stored as internal energy, where h is the Planck constant and c the speed of light. Atoms are the basic building blocks of molecules and consist of an atomic nucleus and electrons. The basic structure was known already in the very beginning of the 20^{th} century resulting from the work of Ernest Rutherford. It postulates the nucleus to have a size in the order of $10^{-14}\,\text{m}$ and concentrate almost the complete atom mass, while the electrons orbit in a shell in the order of $10^{-10}\,\text{m}$ around it. The experimentally observed absorption of radiation at discrete wavelengths could however not be described with Rutherford's model. Moreover, it was not consistent with findings in the fields of mechanics and electrodynamics. The first model approaching an experimentally replicable description of the electron behavior was made public in 1913 by Niels Bohr. It assumes that the electrons orbit around the nucleus in discrete distances. These are calculated based on a quantization of the electrons' orbital angular momentum. Absorption of radiation was explained by the transition of an electron to a larger and therefore higher-energetic orbit. This already allowed calculating the spectra of atoms and ions with one single electron, i.e. H, He^+ and Li^{2+}. Describing the electrons in more complex atoms requires a quantum mechanical treatment based on solving the Schrödinger equation. This yields discrete wave functions for the electrons corresponding to discrete energy levels [63]. If a photon with an energy equal to the energy difference between two levels encounters the atom, it can be absorbed. In this process, one electron leaps to a higher energy level, which means that the atom is then in an excited state. Excited atoms can emit radiation by falling back to a lower energy level [64].

Molecules consist of two or more electromagnetically interacting atoms. They can

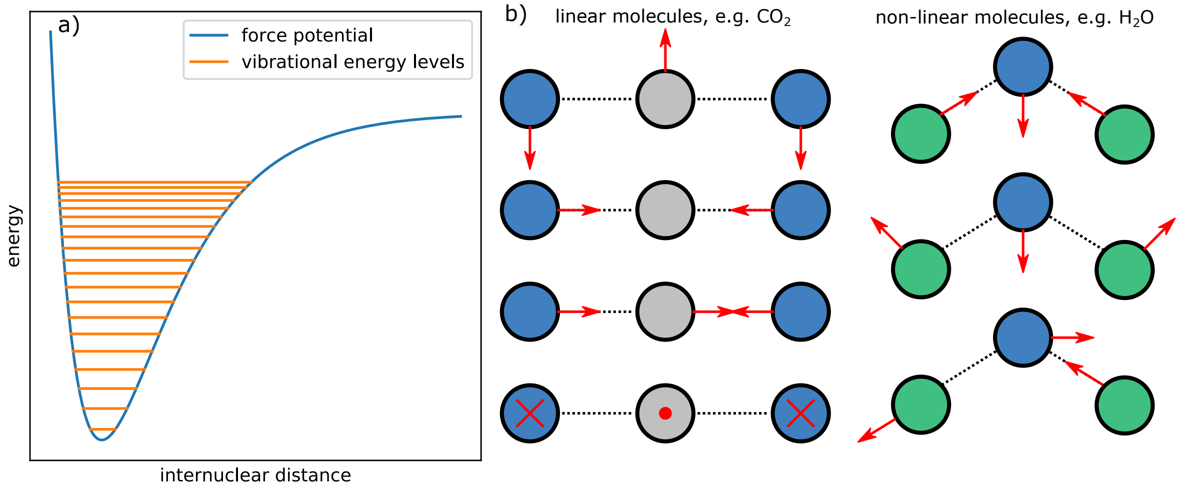

Figure 2.1.: a) Vibrational energy levels in a molecule. b) Vibrations in a linear and in a non-linear molecule, cf. [63].

be electronically excited similar to atoms, and provide an additional mechanism for the absorption of radiation that involves a net change in the dipole moment

$$\vec{p} = |q| \cdot \vec{d}. \tag{2.1}$$

Here q is the charge and $\vec{d}$ is the distance. Changes in $\vec{p}$ generate an electric field that allows photons (or in other words: electromagnetic waves) to interact. Oscillations and rotations in the molecule can be associated with a dipole moment change and can therefore be excited by radiation. The possible oscillation and rotation states are quantized, and the possible energy values can again be calculated by solving the Schrödinger equation [63]. Figure 2.1a) depicts possible energy levels for vibrations in a molecule qualitatively. Each level in itself is further divided in sub-levels corresponding with rotational states (not shown in the figure). Different vibrations that can be excited in linear and non-linear molecules are schematically shown in figure 2.1b). In the spectrum, the transitions between vibro-rotational states can be seen as discrete absorption lines in the absorption spectrum of an IR-active molecule.

Basics of spectroscopic measurements

The shape of the individual absorption lines is determined by two line broadening mechanisms. Doppler broadening is caused by the variation of velocity of individual molecules relative to the infrared beam and is therefore temperature dependent. It causes a Gaussian line profile. For measurements above 1 mbar, collisional broadening influences the line shape as well. This pressure and temperature dependent effect is caused by intermolecular collisions and - considered individually - leads to a Lorentzian profile. In a pressure range between 1 and 100 mbar, both broadening mechanisms are effective simultaneously, leading to a line shape determined by the convolution of the two aforementioned shapes called a Voigt profile. At distinctly higher pressure, e.g. under ambient conditions, Doppler broadening is typically negligible due to the pronounced dominance of collision broadening [65].

In order to calculate a particle density from an absorption spectrum, Beer's law is applied. It correlates the transmittance T of a sample with an absorption coefficient a. The transmittance is defined as the wavenumber-dependent ratio of radiant power after it traveled through the sample I to the respective value before it entered I_0. Using an absorption coefficient a, the absorption length l and the concentration $\tilde{c}$, Beer's law can be stated as

$$T(\tilde{\nu}) = \frac{I(\tilde{\nu})}{I_0(\tilde{\nu})} = 10^{-a(\tilde{\nu})\cdot l\cdot \tilde{c}}, \tag{2.2}$$

where $\tilde{\nu} = \lambda^{-1}$ is the wavenumber. The investigation aims at fitting concentration values for various species to spectra in one single process step, therefore it is necessary to bring equation 2.2 in a form that allows such a procedure. Converting the transmittance to an absorbance

$$A(\tilde{\nu}) = \log_{10}\left(T(\tilde{\nu})^{-1}\right) = a(\tilde{\nu})\cdot l\cdot \tilde{c} \tag{2.3}$$

serves as the first step towards the desired formula. For a mixture of $\tilde{N}$ components, the overall absorbance is then

$$A(\tilde{\nu}) = \sum_{i=1}^{\tilde{N}} \left(a_i(\tilde{\nu})\cdot l\cdot \tilde{c}_i\right) \tag{2.4}$$

[66]. This requires the absorptivity to have a unit of (concentration·length)$^{-1}$, i.e. m^2 as the standard unit according to the SI system [65].

To attribute features in the spectra to specific functional groups, correlation tables can be used. A more convenient and precise method to determine the composition of a sample is fitting known spectra from calculations or reference measurements to the signal under investigation [67]. This approach can serve as the basis for a very efficient work flow, because a reference database can be directly accessed using a public API [68]. Moreover, it allows a direct quantitative analysis.

The state of the art approach to measure absolute molecule densities is absorption spectroscopy [69], what however is a generic term. The actual technology to apply needs to be carefully chosen based on the species of interest, the desired temporal and spatial resolution, the necessary detection limit and constructive properties of the DUT. In the frame of the present project, the desired detection limit needs to be traded off against the possibility to measure *in situ*. Directly in the process chamber, a large variety of relevant processes could principally be observed, but the absorption length would not be more than a few centimeters. In the far-field, a multi-pass cell with an optical path of many meters can be used instead. Therefore, an investigation of the resulting output gas in the far field will be given priority over *in situ* investigations of the actual discharge.

The spectroscopic method to be chosen furthermore needs to provide a broad overview about produced species. This discards methods providing information only in a narrowly confined wavelength range such as quantum cascade laser absorption spectroscopy (QCLAS) [70] and tuneable diode laser absorption spectroscopy (TDLAS) [71]. Here,

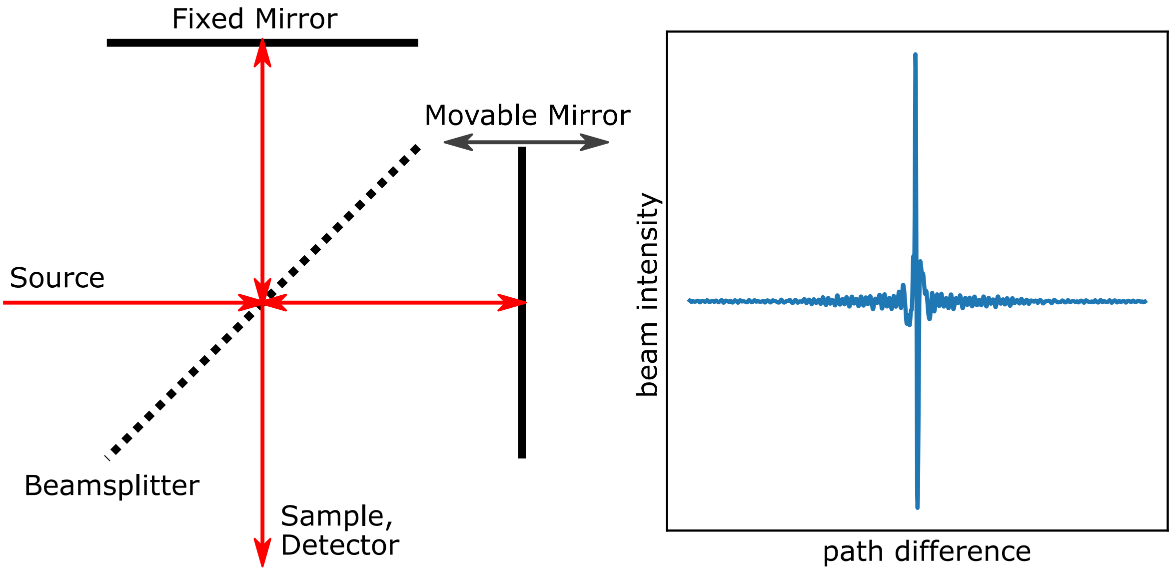

Figure 2.2.: Schematic setup of a Michelson interferometer and a section of an exemplaric, measured interferogram of a black body-type radiator.

a broadband system working in a continuous wavelength range featuring an absorption of all species of interest needs to be used instead. In the desired species (O_3, NO, NO_2, N_2O, N_2O_5, H_2O_2, HNO_2 and HNO_3), vibrational and rotational modes usable for diagnostics can be excited. Fourier-transform infrared (FTIR) spectroscopy is a proven method for their detection [69, 72–74].

2.2. Fourier-transform infrared spectroscopy

The Michelson interferometer

The usual technological realization of the described measurement method relies on two-beam interferometers based on a concept developed by and named after Albert A. Michelson. A Michelson interferometer divides the radiation into two parts that subsequently travel along different paths. Finally, the beams are recombined again, routed through the sample and onto a detector. The length of one path in the interferometer is varied what allows recording an interferogram of the beam intensity

$$S(\delta) = \int_{-\infty}^{\infty} B(\tilde{\nu}) \cos(2\pi\tilde{\nu}\delta) \mathrm{d}\tilde{\nu} \tag{2.5}$$

as a function of the path difference δ [65]. The included wavenumber-dependent quantity $B(\tilde{\nu})$ contains both the signal to be measured and the instrument function. The simplest form of a Michelson interferometer together with a resulting exemplaric interferogram is shown in figure 2.2.

Coming from the source, the radiation is partially reflected onto a fixed, conventional mirror by a semi-transparent mirror called *beamsplitter*. The rest of the radiation travels to another mirror that is movable to introduce a path difference. After being reflected by the respective mirrors, the two partial beams are recombined again at the beamsplitter, where interference between them can occur. The recombined radiation travels in two directions; back to the source and through the sample to the detector. Both of these beams contain equivalent information, but separating the output beam from the incoming one at the source side is difficult. Therefore, only the output perpendicular to the source beam is used. This is also the beam containing all the input power if the movable mirror is positioned in the same distance to the beamsplitter as the fixed one.

If reflected by the beamsplitter, the signal phase changes by 90°, while the transmitted signal is not altered. On the plane mirrors, a phase change of 180° occurs. Consequently, both the beams routed to the fixed and the movable mirror changed their phase by 270° when they emerge in the direction of sample and detector. As they are in phase, the interfere constructively *on the way to the detector*. No power is reflected back to the source because the beam from the fixed mirror undergoes a total phase change of 360° when reflected back to the source, while the one from the movable mirror changes by 180°. Therefore, both beams are opposite in phase and interfere destructively[1] *on the way back to the radiation source.*

The opposite case can be observed at an optical path difference of $\lambda/2$ (corresponds to moving the mirror by $\lambda/4$). Here, an additional phase shift of 180° is introduced which leads to a destructive interference for the radiation directed to the detector. At path differences of λ or multiples of it, constructive interference occurs again. The fact that destructive and constructive interference of radiation with different wavelength appears at different mirror positions suggests that the interferogram contains spectral information. Indeed, the transmittance spectrum of the sample can be calculated using Fourier transformation, after a few peculiarities have been taken into account.

Side-effects of the measurement

The path difference accessible for recording $S(\delta)$ is constructively limited by the interferometer, where the minimum and maximum path difference be $-\Delta$ and Δ, respectively. Consequently, only a section of the (theoretically boundless) interferogram can be measured. This is equivalent to multiplying $S(\delta)$ with a boxcar function

$$D(\delta) = \begin{cases} 1 & \text{if } -\Delta \leq \delta \leq \Delta \\ 0 & \text{if } \delta > |\Delta| \end{cases} , \tag{2.6}$$

what affects its spectrum. Corresponding to the multiplication with $D(\delta)$ in the position domain is a convolution with the Fourier transform of $D(\delta)$ in the frequency domain, i.e. a convolution with

$$f(\tilde{\nu}) = \mathcal{F}\{D(\delta)\} = 2\Delta \mathrm{sinc}(2\pi\tilde{\nu}\Delta). \tag{2.7}$$

Consequently, a line at a discrete wavenumber in the correct spectrum is mapped to a sinc function as the shape of $f(\tilde{\nu})$ as well. This leads to signal components at wrong

---

[1] What, on a more basic physical level, simply means that the photons travel in a different direction and, naturally, does not refer to their destruction.

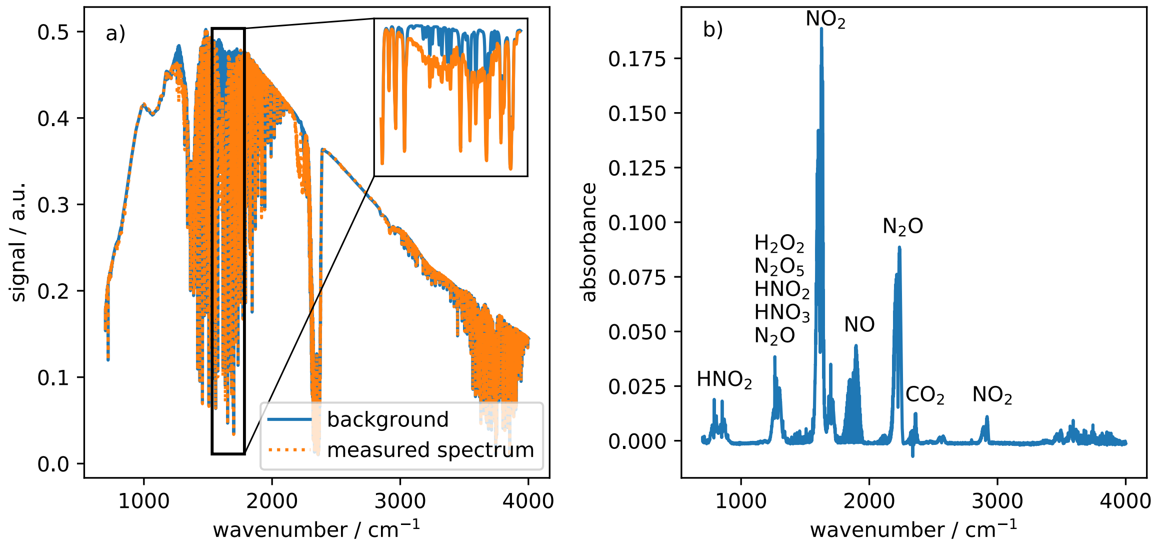

Figure 2.3.: a) Uncorrected transmittance spectrum of a gas sample measured using an FTIR spectrometer and corresponding background spectrum (instrument function). b) Resulting absorbance spectrum of the sample after background correction.

wavenumber positions corresponding to the side lobes of the sinc function. The procedure used to avoid this is called apodization. An apodization function is multiplied with the recorded interferogram in order to substitute the unwanted, constructively given boxcar function with a one that is less disruptive in the spectrum. This can for example be a triangular function that has a spectrum in the form of a sinc^2 function. The latter has considerably lower side lobe amplitudes compared to the sinc function.

Another potential issue are aliasing effects caused by the discretization of the spectrum; a sample rate sufficiently high according to the Nyquist-Shannon sampling theorem allowing for the desired maximum wavenumber is necessary. In contrast, for the user of an FTIR spectrometer, no challenges occur regarding the wavenumber calibration. The latter takes place internally using a He-Ne-Laser [65, 66].

Example spectrum

Figure 2.3a) shows a section from a measured transmittance spectrum of a gas sample containing various RONS in air. A background spectrum in “pure” air has been measured before to capture the instrument function and the absorption caused by H_2O and CO_2. Dividing the measured spectrum $I(\tilde{\nu})$ by the background $I_0(\tilde{\nu})$ yields the transmittance of the RONS to be measured remains. Figure 2.3b) shows it after the conversion to an absorbance spectrum using equation 2.3. The individual absorption bands are labeled with the respective absorbing species. All of them were generated from air that due to its composition can be used to produce a multitude of different products in plasma processes.

2.3. Relevant non-thermal plasma chemistry in air

General considerations

Atmospheric air consists of a variety of different chemical substances and compounds, primarily molecular nitrogen (N_2, 78 %), molecular oxygen (O_2, 21 %), argon (Ar, 0.93 %) and water vapor (H_2O, concentration highly variable) [75]. Without an additional energy input, the components are stable in the mixture. In contrast, high-energetic electrons that are present in non-thermal gas discharges can initiate entire reaction networks. By colliding with other constituents of the plasma, electrons can dissociate molecules, form electronically excited states of atoms and molecules and ionize neutral components. An important parameter for these processes is the ratio of the frequency of collision events per particle relative to the flux of incident interaction partners. It depends on the kinetic energy and therefore on the relative velocity v of the particles and is called cross section $\sigma(v)$ of the interaction partners.

For most atoms and molecules in the ground state, the cross section for electron impact ionization is non-zero only for higher energies that, according to the expectable electron energy distribution, can only be provided by a small proportion of the available electrons. In comparison, the energy necessary to ionize an excited metastable atom or molecule is distinctly lower and the ionization cross section is higher. Therefore, stepwise ionization processes including an intermediate excited state are significant despite the density of excited states being typically much lower than of the respective ground state particles [23]. Ionization processes are the primary charge carrier production mechanism and hence crucial for the sustainment of the plasma. The excited states, atoms and ions produced by electron impact initiated processes react further with each other as well as with electrons and with the initial gas components. This eventually leads to vast reaction networks.

In order to describe the involved reactions, rate coefficients are defined. For electron collision processes, these are

$$k = \int \sigma(v) v f(v) \mathrm{d}v \tag{2.8}$$

where $f(v)$ is the electron velocity distribution, although v generally refers to a relative velocity: In non-thermal plasmas, the heavy particles can usually assumed to be at rest with respect to the electrons. Determining $f(v)$ for electrons in plasmas is challenging and its approximation, e.g. by a Maxwellian or a Druyvesteyn distribution, can introduce substantial inaccuracies. To overcome this, a numerical approximation of $f(v)$ is possible [76]. In contrast, the velocity distribution of heavy particles can be expressed reliably as a Maxwellian distribution. This allows collisions among heavy particles to be described by rate coefficients depending on the gas temperature T in form of the modified Arrhenius law

$$k(T) = A_\mathrm{r} (T/\mathrm{K})^n \exp\left(-\frac{E_\mathrm{a}}{k_\mathrm{B} T}\right) \tag{2.9}$$

[23]. Here, A_r is a scaling parameter and n describes the growth of k with temperature, thus it is a curvature parameter. Furthermore, the activation energy for the process E_a and the Boltzmann constant k_B are included in the calculation.

Essential modeling approaches

Established modeling techniques calculate the dynamics of charged particles coupled to the electric field distribution, what yields a self-consistent description of the problem. Fluid models as a notable example solve the continuity equations for the charged species coupled to the Poisson equation, often one-dimensionally. Enhanced by a suitable reaction set describing neutral particles in ground and excited states, this can allow modeling chemical processes reliably depending on the prevailing conditions [11, 77]. In order to facilitate the obtaining of relevant results faster and thus to provide a basis for system solutions suitable for industry, a simpler alternative needed to be introduced. This demand is met by reaction kinetic approaches that can substantially reduce computational costs. Here, the modeled reactions are triggered by a chemical input instead of a co-simulated electrical field.

Extensive models for plasmas in air include neutrals, excited states and ions summing up to more than 50 species and almost 600 reactions [78] or even over 1000 reactions to model conditions in the open environment around a helium jet [79]. Depending on the phenomena to investigate, reduced sets of species and reactions can be used as well, in particular when water vapor is not taken into account. Reaction sets with 21 [80] or - to investigate a particular hypothesis - 4 [81] reactions can be found in the literature among others.

Almost all models include ozone (O_3), nitric oxide (NO) and nitrogen dioxide (NO_2). Molecular oxygen (O_2) and atomic oxygen (O) - the latter resulting from the preceding dissociation of O_2 - form O_3. This involves an arbitrary third collision partner and is therefore most efficient at higher pressure - at low pressures, O_3 is only produced in surface reactions [82]. Also molecular nitrogen (N_2) reacts with O what leads to the formation of NO and atomic nitrogen (N). The so-formed reactive species O_3 and NO can further react to NO_2 and O_2. The reaction of NO_2 with O again forms NO and O_2. This very simple scheme of formation and destruction mechanisms for reactive species outlines a starting point to find suitable reaction sets to explain, improve and control plasma-chemical phenomena in air. Figure 2.4 gives a graphical overview about the mentioned reactions.

To include an initial formation of O, two ways are common: The first is explicitly enhancing the reaction set with suitable electron impact reactions and equations describing the energy balances for the electrons and heavy particles. The rate coefficients for electron reactions are commonly approximated by mean-field approaches in this case [78]. The second option is to introduce an artificial source term of O to overcome the necessity to determine the electron energy distribution. However, a reasonable formation rate for O needs to be known in this case. Generally, compiling suitable reaction sets by identifying important processes to include in the model and choosing the correct reaction rates for them are among the main challenges in plasma chemical modeling.

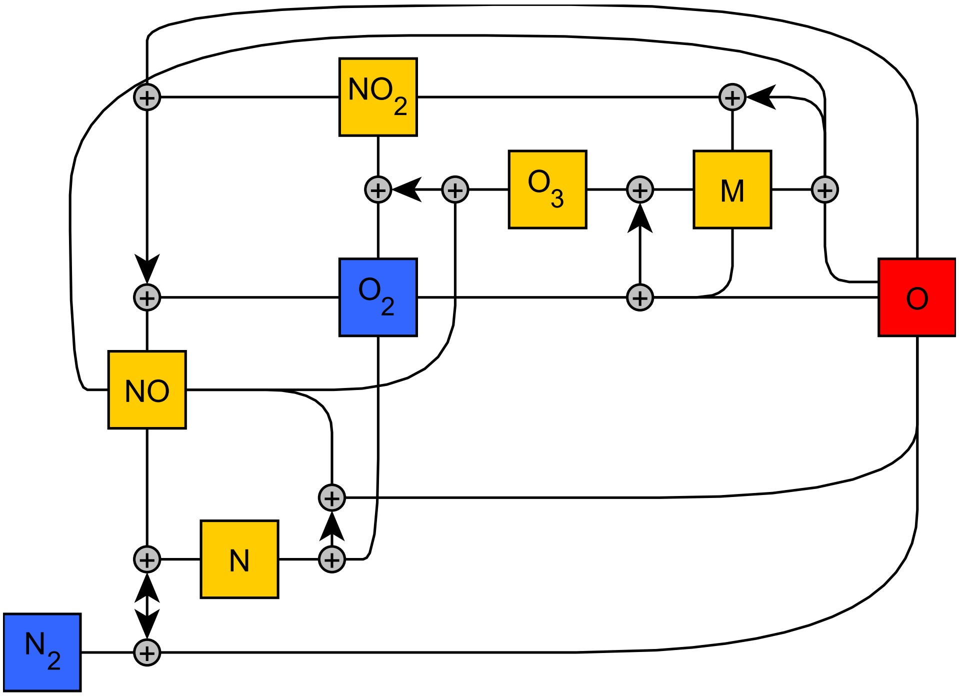

Figure 2.4.: Simplified reaction network based on N_2 and O_2, triggered by O.

Apart from that, reducing the dimensionality can substantially simplify the modeling process and is entirely usual. In many cases, processes are investigated using equations that only depend on time and assume spatial homogeneity. These models are called zero-dimensional. Systems with a pronounced spatial structure however are often investigated in one or two spatial dimensions, accepting an increase in computational costs. Although the zero-dimensional approach already simplifies the problem substantially, the system of differential equations representing the chemical reactions is still non-linear and can as well feature time-dependent source terms.

Concerning the complexity, plasma systems involving liquids surpass gas-phase-only reactors by far. Various additional processes are coupled to the gas phase discharges, which already tend to behave inconveniently in the presence of water vapor. Among the mechanisms to take into account are multiphase species transport, mass and heat transfer, interfacial reactions as well as liquid chemistry. Nevertheless, both models of gas plasmas interacting with liquids and plasmas in liquids have been established in the past years, where the former processes are better understood than the latter [57]. The present work does not cover interactions with liquids.

Worth noting are the timescales being characteristic for the different mentioned processes. Many charged particles have a lifetime of a few nanoseconds or less, while reactions among neutral components can distinctly affect the species compositions even after several seconds. A particularly efficient method to include the combined effect of both very dynamic and slow processes is the usage of two coupled models. The latter are solved iteratively while the diffusion of long-lived species acts as the coupling mechanism and the timescales for the virtual reactors themselves are independent [78].

Plasma chemical modeling efforts in this work focus on a simple gas phase reaction kinetic model to support the FTIR measurements in section 3.3. The model will not aim at establishing a comprehensive theoretical counterpart to the experiments. Instead, the question to be answered will be which reaction pathways are crucial to explain (and therefore control) phenomena of interest. Thus, a set of coupled equations for the relevant heavy-particle reactions will be compiled and solved.

2.4. Dielectric barrier discharges

The behavior of gas discharges at atmospheric pressure is dominated by particle collisions, what leads to a tendency to equilibrate electron and gas temperature. Dielectric barrier discharges (DBDs), also known as “silent discharges” are among the most common plasma source types that still remain in a non-thermal regime at atmospheric pressure.

2.4.1. Construction and basic properties

DBDs feature an insulating material between the electrodes that avoids the formation of a spark or arc discharge, but precludes a direct voltage operation. Using sinusoidal voltages with frequencies in the kHz range is common, alternatively higher frequencies or pulsed signals can be used depending on the envisaged purpose.

A large range of applications including surface treatment, pollutant degradation and radiation generation relies on DBD systems in very different configurations. Electrodes can be designed planar, both symmetric or asymmetric, and positioned in a variety of different ways relative to one or two dielectrics. This allows the formation of discharges in a volume or on a surface of the reactor. Curved or structured electrodes and dielectrics allow an even larger creative leeway. The choice of materials for the dielectric and possibly for electrodes in contact with the discharge needs to fulfill technological and plasma-chemical requirements. Certain reactive components can erode or corrode the surfaces. Moreover, the dielectrics themselves can wear out as a result of partial discharges [83]. Typical examples for the dielectric material are glass (including quartz) and ceramics (such as aluminium oxide Al_2O_3), among others [11, 17].

The DUTs to be investigated regarding their RONS output have been constructed concomitant to the investigations presented in this work. Both of them are DBDs and represent two common basic designs among the large variety of different constructions established for different purposes. A schematic cross section of the coaxial design presented in section 1.2 is shown in figure 2.5a, while figure 2.5b shows the cross section of the planar device also presented in section 1.2. The sketches illustrate that the coaxial prototype has only one dielectric that covers the ground electrode, while the signal electrode is in contact to the plasma. The planar design uses two dielectrics, however the basic electrical properties of both designs are very similar.

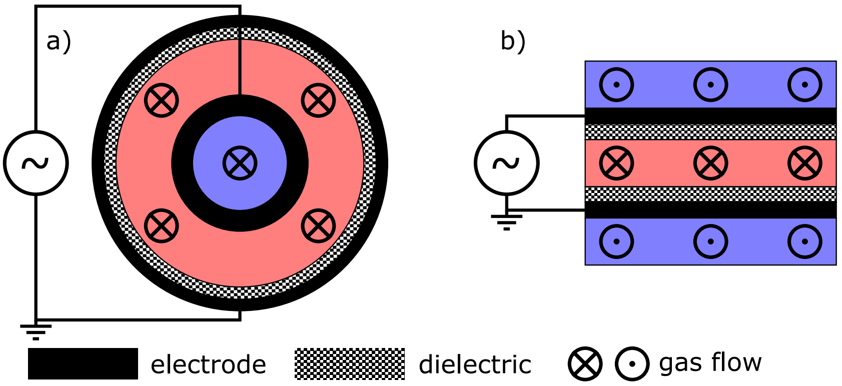

Figure 2.5.: Cross section of the two dielectric barrier discharge types used to investigate the VDBD concept. Regions in blue contain cooling air, the red regions are filled with process gas.

Both versions are intended for operation in air at medium and normal pressure, what involves the formation of filaments in the plasma. This is caused by the spatial charge distribution in electron avalanches that creates an additional electric field and hence promotes the formation of additional avalanches in its proximity. Therefore, ionized regions grow to distinct, constricted plasma channels, so called filaments or microdischarges. A multitude of microdischarges spreads over the barrier, where a higher voltage amplitude will lead to a larger number of discharges rather than an increase in charge transferred per single filament. The duration of a microdischarge in air at atmospheric pressure is in the range of 10...100 ns and involves a charge transfer of 0.1...10 nC [17].

2.4.2. Electrical modeling of DBDs

A typical feature of DBDs is the self-pulsing operation that is facilitated by charge accumulation on the dielectrics' surfaces. The accumulated charge creates an electric field opposed to the externally applied one. This lets the discharge extinguish in extrema of the external voltage when the absolute value of the corresponding electric field stops increasing. In the subsequent half-cycle, the accumulated charge supports the re-ignition [17].

Typical electrical diagnostics setups for DBDs are based on the recording of voltage V and - via a capacitor in the ground line - charge Q. Evaluating the so-called Q-V-plot (sometimes called “Lissajous figure”) that is exemplary shown in figure 2.6a) in DBDs is established since 1943 [14]. It avoids the necessity of using high bandwidth probes and oscilloscopes. A correct current measurement in contrast would require resolving very steep slopes caused by incepting and decaying microdischarges. The self-pulsing operation finds expression in the Q-V-plot as an alternation of slopes in the figure; in inactive phases, the slope is comparably low and equals the capacitance of the complete cell without a discharge C_{cell}. In phases where microdischarges occur and the device therefore is active, the slope is equal to the dielectrics' capacitance C_{d} or slightly below. Beyond the capacitances, other characteristic values of the DBD can be deduced from

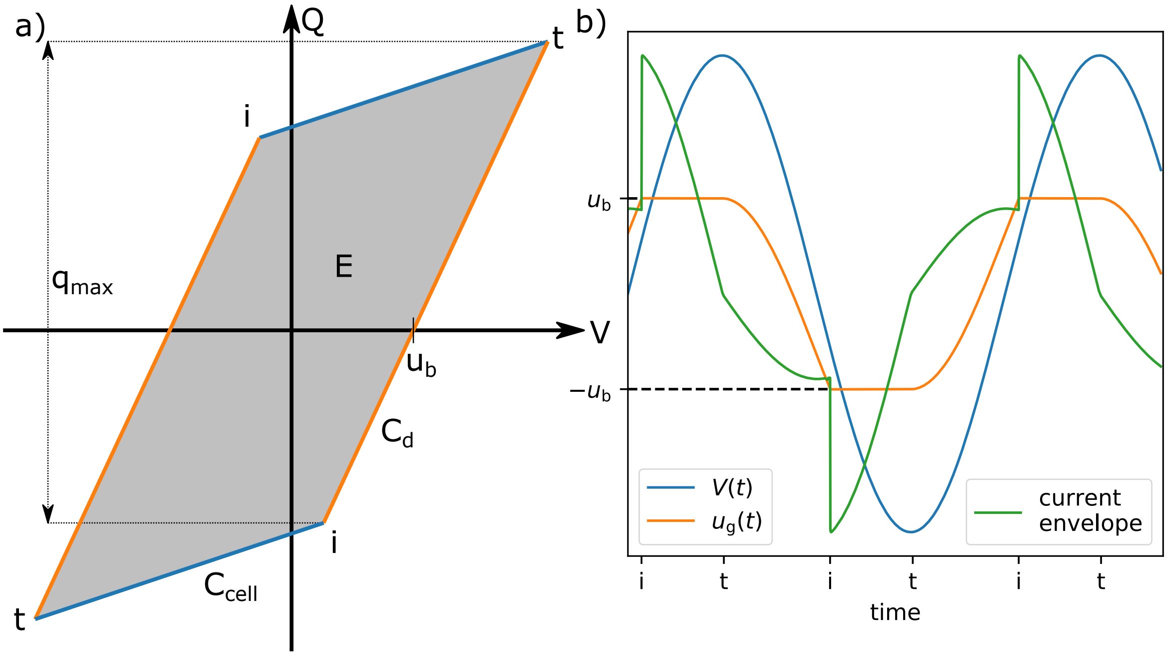

Figure 2.6.: a) Schematic Q-V-plot of a DBD b) External voltage, current and gas gap voltage during DBD operation. “i” and “t” mean “inception” and “termination”.

the Q-V-plot; namely the energy E dissipated in one period, the maximum charge transferred through the gas gap $q_{\max}$ and the burning voltage u_b.

Approaches for modeling the electrical behavior can cover essential physical effects such as the self-organized formation of filaments [84]. However, for a basic characterization, electrical lumped element models are usually preferred. They need to represent the self-pulsing behavior and distinguish at least the dielectrics and the gas gap. For the case of two dielectrics, the latter are usually combined to one capacitive element. Figure 2.7 shows the simplest representation of a sine-driven DBD by an equivalent circuit commonly found in the literature [11,85,86]. It uses a time-dependent resistor $R(t)$ to model the conductivity of the discharge. An explicit description of this component is usually not necessary, because the voltage over it can simply be calculated by subtracting the voltage drop over C_d from the overall voltage $V(t)$. The capacitance C_d represents the dielectrics, while C_g describes the capacitance of the gas gap. Thus, the total capacitance of the cell can be calculated as

$$C_{\text{cell}} = \frac{C_g C_d}{C_g + C_d}. \tag{2.10}$$

During the inactive phases, $R(t)$ is infinitely large, consequently C_g alone describes the gas gap in these phases. Figure 2.6 shows $V(t)$, $u_g(t)$ and the current resulting from the equivalent circuit.

For the case that microdischarges do not spread over the complete electrode cross section in the active phases, the presented equivalent circuit cannot deliver an adequate

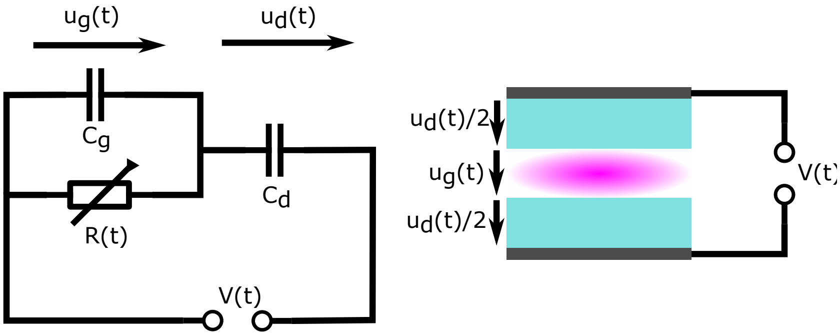

Figure 2.7.: The simplest equivalent circuit suitable to represent a sine-driven DBD with a sketch allocating the partial voltages in the physical setup. Taken with permission from [62], © IOP Publishing Ltd.

description. Instead, this operating mode, that is usually linked to electrode voltages not much above the minimum operating voltage, requires one additional branch in the equivalent circuit to represent the fraction of the electrode cross section that is not covered by discharges [87].

A crucial prerequisite for the application of the presented equivalent circuit (and for enhanced versions of it as well) is a reliable knowledge about the dielectrics' capacity C_d [88]. A simple analytical determination of this quantity is possible provided that edge effects can be neglected [89–91]. One alternative approach is the measurement of C_d based on multiple Q-V-plots measured at different external amplitudes. This, however, only works if the discharge extinction voltage does not change over the external amplitude [88, 92]. Another, simpler method is the evaluation of the slopes of the Q-V-plot in the active phases [7, 93, 94].

Using this information, the voltage over the gas gap, that in the active phases equals the voltage over the discharge, can be calculated as

$$u_\mathrm{g} = V(t) - \frac{Q(t)}{C_\mathrm{d}}. \tag{2.11}$$

3. Influencing the produced species composition

Based on the Venturi-DBD concept and the physical, chemical and technological basics presented before, a device continuously tunable from an O_3- to a NO-production is to be developed. As the initial step towards this goal, fundamental scientific mechanisms influencing the produced species composition need to be identified. With the laboratory prototype presented in section 1.2, a suitable device under test (DUT) is already available. It offers a variety of input parameters that are potentially useful to influence the concentration and composition of produced RONS. While the dissipated electrical power as well as the gas flow rate are common variable parameters in a multitude of different RONS sources, the influence of pressure variations in a range of 200...600 mbar has hardly been investigated, at least considering this order of magnitude. In order to investigate the effects caused by different parameters including the pressure as well as their sensitivity, an experimental setup to investigate the output gas has been realized.

It revealed that the electrical input power does not directly define the output gas composition in the given general parameter range. Instead, it is a crucial parameter to adjust the gas temperature that determines whether primarily O_3 or NO is produced. The temperature necessary to obtain a particular RONS composition is pressure dependent. Consequently, two essential parameters need to be controlled jointly to set a specific mixture.

3.1. Initial characterization

The key information to characterize the VDBD concept is the concentration and composition of produced reactive species. For their detection in the far field, a FTIR spectrometer (Vertex 80v by Bruker, USA) was used. The device does not analyze a gas sample in the DUT, but instead the gas collected in a multi-pass cell (MPC). To allow the detection of low species densities, the MPC routes the infrared radiation several times through its volume of about 15 l, leading to an overall absorption length of 32 m. In order to transport the gas sample into the MPC, a vacuum pump is connected to the MPC outlet. The pressure difference between MPC and the outlet of the DUT then causes a gas transport through the cell. As the DUT, the initial VDBD prototype was used and operated at different pressure levels. To obtain a first overview, for each pressure value, the electrode voltage amplitude and hence the dissipated power was varied. By recording spectra in a wavenumber range of 700...4000 cm^{-1}, the species ozone (O_3), nitrogen dioxide (NO_2), nitric oxide (NO), nitrous oxide (N_2O), dinitrogen

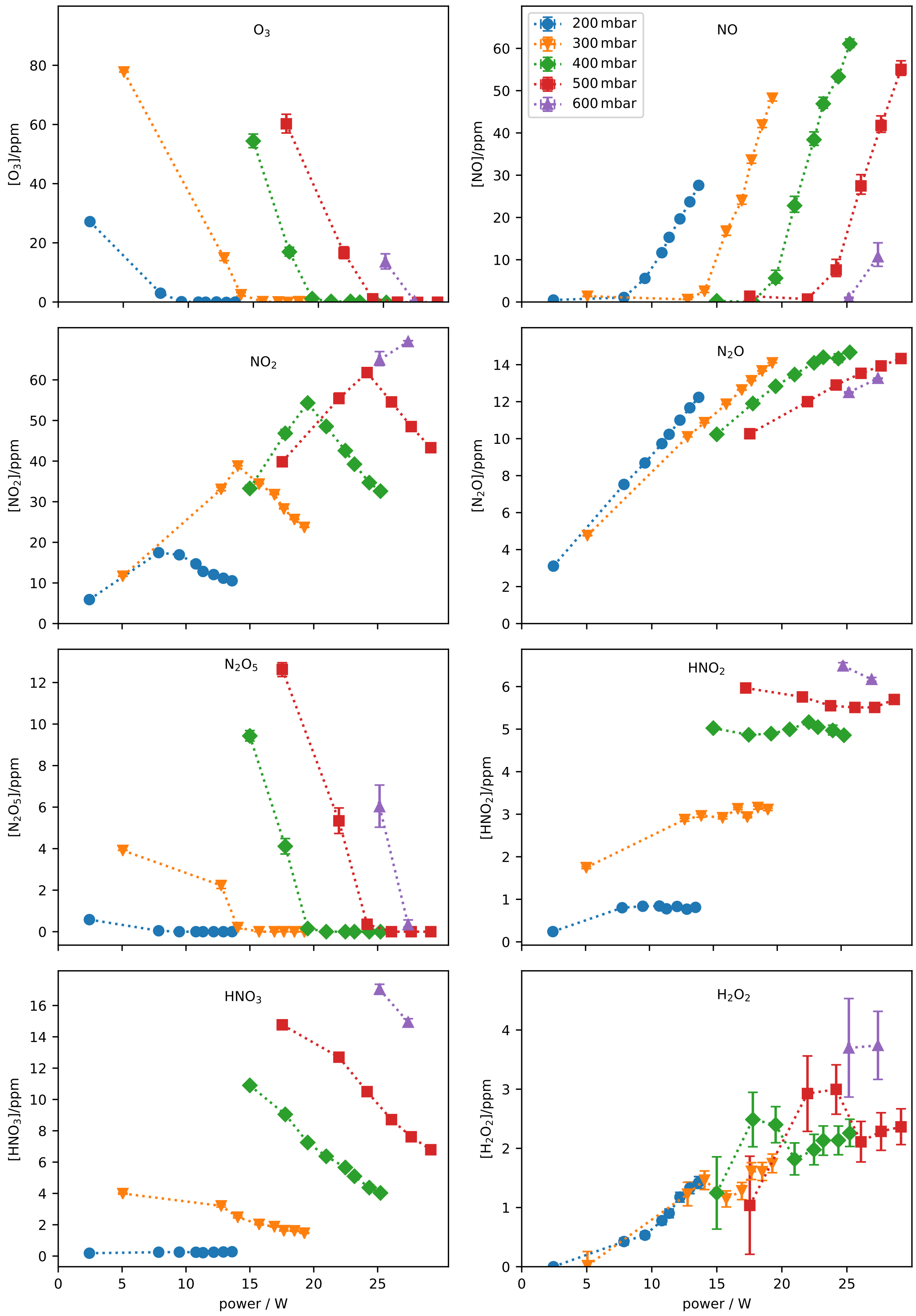

Figure 3.1.: Concentration of RONS in the output gas after five minutes of operation. Taken with permission from [16], © IOP Publishing Ltd.

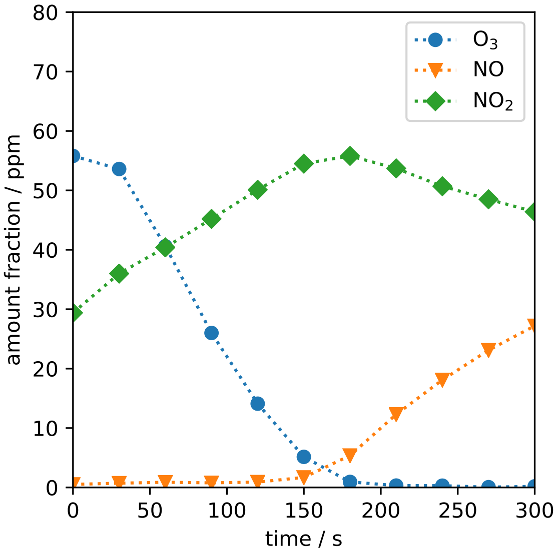

Figure 3.2.: Measured concentration of the three most abundant species over time at 400 mbar and 21 W. Taken with permission from [16], © IOP Publishing Ltd.

pentoxide (N_2O_5) and nitric acid (HNO_3) could be identified and quantified. After the DUT was in operation for five minutes, this lead to the species concentrations depicted in figure 3.1.

By increasing the dissipated power, the produced O_3 density $[O_3]$ is decreased, whereas $[NO_2]$ is increased. At a certain pressure-specific power level, the production of O_3 completely vanishes and $[NO_2]$ reaches a maximum. Even higher input power levels cause a decrease in NO_2 production, but lead to the formation of NO in the far field. By increasing the pressure, both the produced amount of O_3 and NO_2 is increased, while an inverse effect can be observed for NO and N_2O. The density of the latter species never rises above 16 ppm and thus remains lower compared to $[O_3]$, $[NO_2]$ and [NO] with up to 60...80 ppm in each case. N_2O_5 can be found in the VDBD output gas in comparably low maximum densities around 4...13 ppm and with a power dependence comparable to that of O_3.

Both N_2O and N_2O_5 were detected and quantified using their absorption in the range between 1220 and 1360 cm^{-1}. In addition to the two mentioned compounds, HNO_3 absorbs in the same range, but considering only these three species, no adequate replication of the measured signal could be achieved. Instead, HNO_2 and H_2O_2 needed to be taken into account as well. No densities above 7 ppm could be detected for these two species, so that both do not heavily contribute to the overall amount of produced species. Despite, their inclusion decreases the confidence interval of $[N_2O]$, $[N_2O_5]$ and $[HNO_3]$ determined by the fit, because the absorption profile of the three more abundant species would otherwise be fitted also to lines that actually belong to HNO_2 and H_2O_2.

More important for the aim of the investigation are O_3, NO_2 and NO, therefore the complete spectra dataset for these three species has been exemplarily checked for consistence and plausibility. This also includes spectra recorded before the envisaged waiting time of five minutes. The waiting time before the measurement was intended to ensure a stationary gas composition in the MPC. Based on the volume of and the gas flow through the cell, it can be assumed that the gas in it is almost completely replaced after two minutes. A longer time ensures that a certain mixing effect in the MPC is allowed for. However, an analysis of the complete recorded dataset revealed that the concentration of the investigated species remained dynamic until five minutes elapsed. This is depicted in figure 3.2 and motivates an investigation of possible reasons for that dynamics.

A similar dependence of the concentration of RONS on time and the applied power was reported by Pavlovich *et al.* for a surface DBD [41]. Yet, this device differs from the VDBD in some essential aspects. While the VDBD operates on a gas flow, the device from Pavlovich *et al.* treats a stagnant gas volume. Moreover, in contrast to the VDBD, it allows measuring the gas composition almost in situ. For this purpose, infrared radiation from an FTIR spectrometer is routed through the device directly below the discharge zone. Despite, only relatively stable species were detected. Over time, a transition from an O_3- to a NO_x-dominated chemistry could be achieved, while the input power determined the time after which a transition occurs. To explain the mechanism behind the O_3- to NO_x-transition, an approach presented by Shimizu *et al.* was quoted. It stresses the influence of vibrationally excited nitrogen ($N_2(\nu)$), while a substantial influence of the gas temperature was precluded because the surface DBD investigated in both cases hardly warms up [81]. Observations from the first measurement sessions however suggest that this does not necessarily hold for the VDBD. Therefore, the gas temperature needs to be considered in the present measurement setup as well.

3.2. Influence of gas temperature

In order to measure the gas temperature in a non-equilibrium discharge, several methods are already established. Recent publications reveal the tendency that the usage of fiber-optical probes becomes a standard method for this application [74, 89]. With that, it partially supersedes the temperature determination from emission spectra that is used routinely as well [95–97], but potentially leads to an overestimation of temperature [98].

An accessible process chamber is a prerequisite for both of the methods. A mechanical access allows inserting the fiber optical probe and an optical access transparent in a suitable wavelength range (e.g. around 391.4 nm in the first negative system of ${N_2}^+$) allows capturing emission spectra. The initial DUT designated for the first investigations of the VDBD concept does not facilitate any means for gas temperature measurement though. For a supersession by a new design, the characterization of the concept is still too fragmentary; it cannot be ensured yet that a time-consuming (and thus expensive) new development and manufacturing leads to a sustainably useful result. Therefore, establishing a temperature measurement is so far limited to finding a suitable workaround.

In general, the temperature distribution in the device is expected to be strongly inhomogeneous [99, 100]. In the discharge zone, the power that actually causes the heating is dissipated, consequently the temperature will be the highest in this region. A constant value however cannot be expected, because the process gas enters the device at ambient temperature and is gradually heated while it passes the discharge zone. The signal electrode located in the center of the device is made of stainless steel and hence has a high thermal conductivity. This helps limiting the temperature, but also distributes the heat along the flow direction and therefore mitigates the temperature inhomogeneity. To the outer side, the process chamber is confined by quartz glass that is thermally insulating

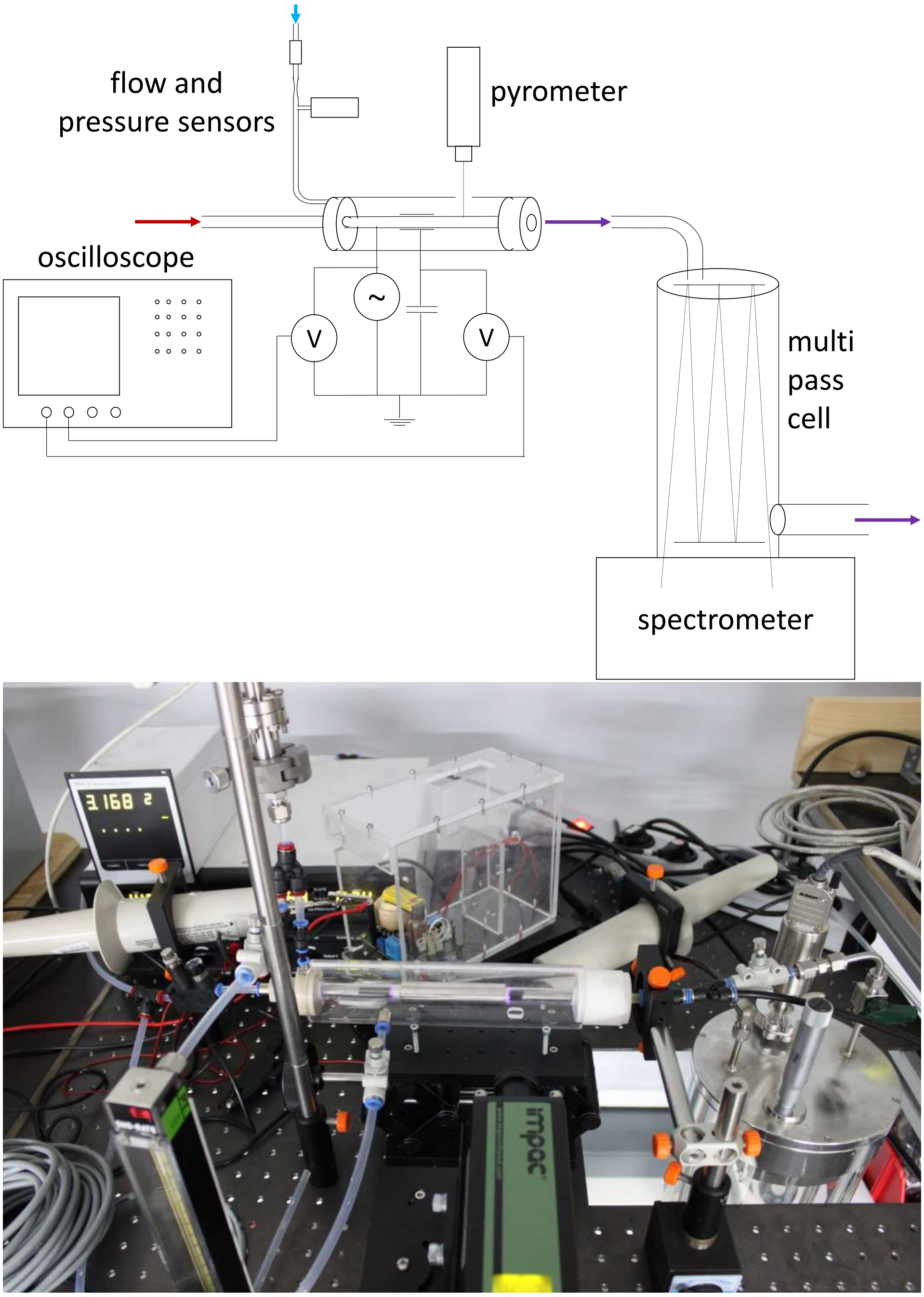

Figure 3.3.: Complete setup used to investigate temperature, species output and dissipated power in the DUT. Sketch taken with permission from [16], © IOP Publishing Ltd.

to a larger extent than the steel electrode in the center. Consequently, the outer region is expected to heat up less.

Due to the inhomogeneity, it needs to be validated carefully that the temperature is measured at a point where it is most meaningful for the present investigation. The location in the DUT where the temperature influences plasma chemical processes is directly in the discharge zone, however this region is not accessible. On the surface of the inner electrode, the temperature as a continuous quantity can expected to be the same as in the adjacent gas. Therefore, measuring the surface temperature on the inner electrode in the DUT can provide values that can expected to be in good agreement with the gas temperature.

For the surface temperature measurement, a pyrometer (LumaSense IMPAC IP 140) was used in a setup that is entirely depicted in figure 3.3. In a distance of 3 mm to the active zone, the pyrometer measured the radiation in a wavelength range of 2...2.8 µm from a spot of 0.6 mm diameter. The wavelength range ensured that the dielectric in the beam path cannot substantially influence the measurement; quartz is highly transparent in this range. Due to the good thermal conductivity of the steel electrode, the fact that the point of measurement was slightly outside the active zone seemed to be tolerable. Soot was applied on the surface using a candle around the spot where the measurement took place. This ensures that the emission coefficient can be reliably approximated with $\epsilon \approx 0.95$.

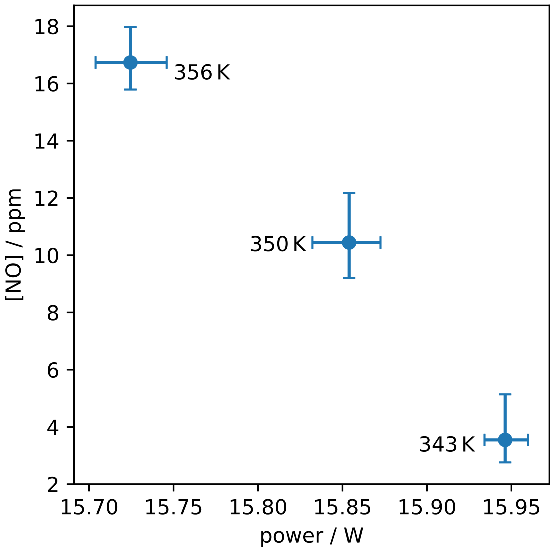

Figure 3.4.: Measured NO concentration with rising temperature. The input power remains approximately constant. Taken with permission from [16], © IOP Publishing Ltd.

In the device, a distinctly lower value for ϵ was set purposely to allow a measurement of temperatures below the designated lower display limit of 100 °C. The calibration was performed on a heated steel plate with a comparable sooted surface and a fiber-optical probe (FOTEMP1-OEM). Figure 3.4 shows that there is a substantial influence of temperature on the production of NO. This motivates a further investigation about the influence of pressure, temperature and dissipated power.

3.3. Pressure and temperature as decisive parameters

Using the measurement setup depicted in figure 3.3, the correlation between temperature and species concentrations has been investigated. Figure 3.5 shows the results for the three most abundant species, with one notable difference to figure 3.1: Not only one

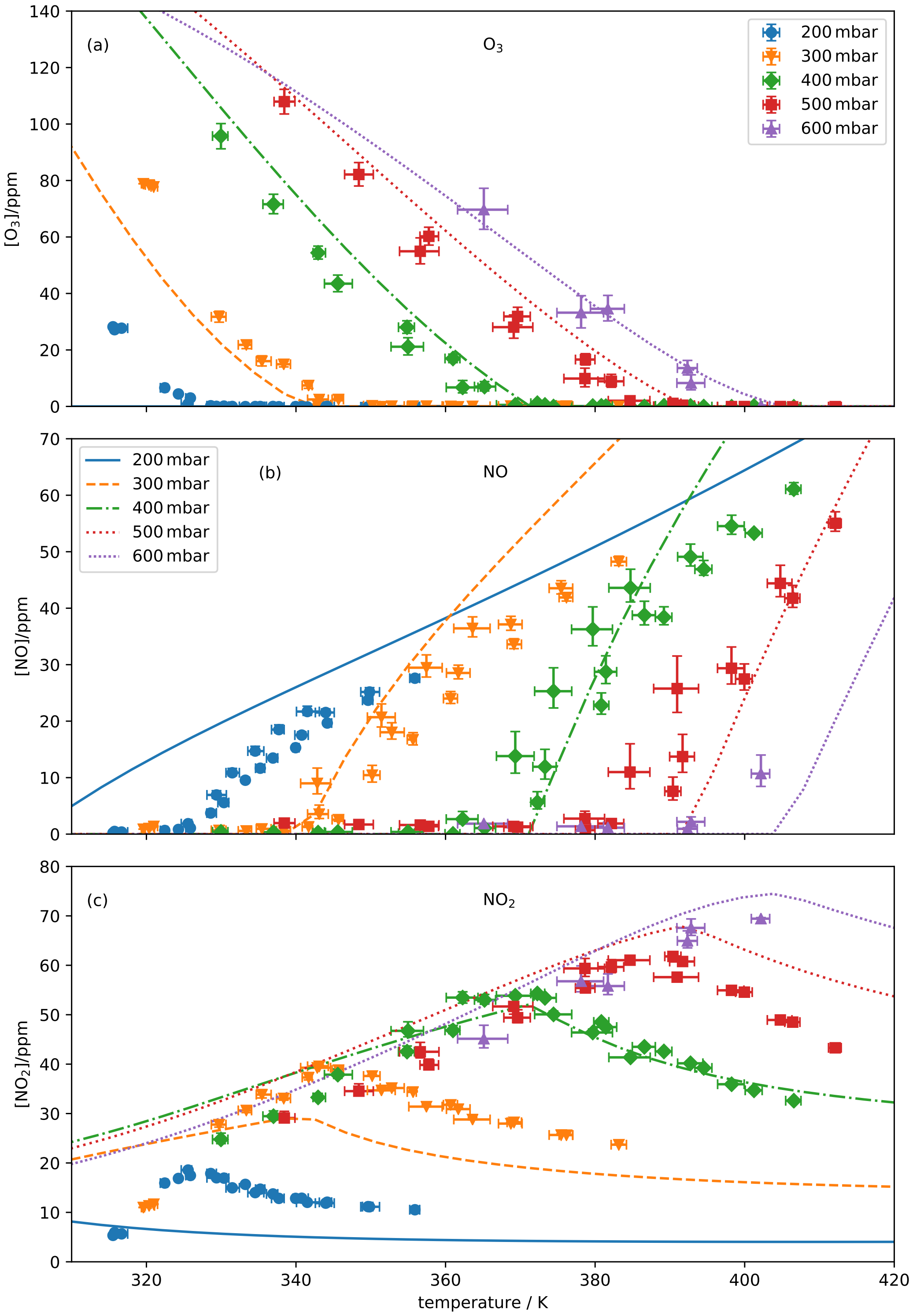

Figure 3.5.: Concentration of O_3, NO and NO_2 depending on the temperature. All power levels used in the experiments are considered in the plot, the measured temperatures are depicted by markers. Lines show simulated results scaled by a factor of (a) 2, (b) 4 and (c) 1.5, respectively. Taken with permission from [16], © IOP Publishing Ltd.

value captured after five minutes of operation is depicted, but three values for each measurement session. These were recorded in the time span beginning two minutes after the start-up and ranging over three minutes. The respective three data points represent different temperature values, a time dependence beyond this was not observed. Moreover, the measurements were repeated using the input power values already used for figure 3.1. The data for all power levels is included in figure 3.5.

Consequently, pressure and temperature seem to be decisive for the transition from an O_3 to a NO production. The input power determines the time necessary for a heat-up to the pressure-dependent transition temperature. Moreover, it influences the produced species concentration. This is in good agreement with the findings of Pavlovich *et al.*, except that the VDBD heats up and the gas temperature seems to have a substantial influence on the species production in this case. To solve the question which mechanisms are dominant for the O_3 to NO transition, a reaction kinetics model has been set up. The obtained results are in very good agreement to the measurements regarding the pressure-dependent transition temperature. In contrast, the absolute densities are underestimated, although they are in the correct order of magnitude. Therefore, the corresponding curves in figure 3.5 have been scaled by factors of 2 for O_3, 4 for NO and 1.5 for NO_2.

3.3.1. Modeling the basic process

Reaction kinetics models are an established tool to simulate and analyze chemical processes. Consequently, numerous simulation platforms support generating and computing these models with varying functionality. For the present task, a seamless integration of customized fit and post-processing routines is crucial for an efficient workflow. This allows a comparison to the measured values, in particular with regard to the O_3 to NO transition temperatures, in order to validate and compare the suitability of different reaction sets.

A Python-based reaction kinetics solver written by Ansgar Schmidt-Bleker was found to be an ideally suited tool for the present investigation [16]. It defines classes for the individual species and parameters as well as for reactions and complete reaction sets. The latter are used as an argument to instantiate a study, where the provided class includes methods to compile and solve the system of coupled differential equations that follows from the reaction set. Routines performing basic scientific computing tasks are imported from the Python libraries *SciPy* [101] and *SymPy* [102].

A collection of helpful post processing methods can be accessed from another class in the reaction kinetics solver, but as the program is available as well-structured Python code, customized analysis routines can easily be integrated as well. The most relevant enhancement used here is that the simulated O_3 to NO transition temperatures were calculated as the temperature value where the quasi-stationary O_3 and NO concentrations are equal. This served as the basis to fit the pressure evolution of O_3 to NO transition temperature to the measured data using the parameters discussed below.

Table 3.1.: Reaction set used for the kinetic model to describe the O_3 to NO transition. M is an arbitrary collision partner.

	Reaction	Rate / (cm^3s^{-1} or cm^6s^{-1})*	Reference
(R1)	$N_2 + O \longrightarrow NO + N$ and $N_2(\nu) + O \longrightarrow NO + N$	$7 \cdot 10^{-15}$	fit
(R2)	$N + NO \longrightarrow N_2 + O$	$2.09 \cdot 10^{-11} \cdot \exp\left(-\frac{100}{T_g}\right)$	[103]
(R3)	$N + O_2 \longrightarrow NO + O$	$1.5 \cdot 10^{-12} \cdot \exp\left(-\frac{3600}{T_g}\right)$	[103]
(R4)	$O + NO + M \longrightarrow NO_2 + M$	$1 \cdot 10^{-31} \cdot \left(\frac{300}{T_g}\right)^{1.6}$	[104]
(R5)	$O_3 + NO \longrightarrow O_2 + NO_2$	$1.4 \cdot 10^{-12} \cdot \exp\left(-\frac{1310}{T_g}\right)$	[105]
(R6)	$O + NO_2 \longrightarrow NO + O_2$	$5.5 \cdot 10^{-12} \cdot \exp\left(-\frac{188}{T_g}\right)$	[105]
(R7)	$O + O_2 + M \longrightarrow O_3 + M$	$3.4 \cdot 10^{-34} \cdot \left(\frac{300}{T_g}\right)^{1.2}$	[106]

* Second and third order reactions, respectively

Description of model, reaction set and reaction rates

The reaction kinetics solver calculates the individual species densities $[X] \in S$ in a species density set S over time. For this purpose, reactions producing X and reactions consuming X are compiled into gain terms G and loss terms L, eventually resulting in

$$\partial_t[X] = G(S) - L(S). \tag{3.1}$$

The species density set for the present investigation is $S = \{[O], [O_3], [N], [NO], [NO_2]\}$.

Plasma chemistry in air is very complex in general, recognizable by very extensive models necessary to simulate processes such as the discharge inception in long air gaps [107]. An important reason for this high effort is a crucial influence of humidity. For air DBDs under relatively dry conditions, much simpler reaction sets are known from Rajasekaran *et al.* [80] and Shimizu *et al.* [81], among others. In the present investigation, the reactions that primarily cause the observed temperature and pressure dependent O_3 to NO transition should be identified. To achieve this, the small reaction set shown in table 3.1 is sufficient.

Reaction set and reaction rates (R1) is the only reaction in the set that explicitly includes an excited state, namely vibrationally excited nitrogen $N_2(\nu)$. Neglecting this species would reduce the considered mechanisms for NO production to the not-extended Zeldovich process (R1 and R3) as well as the dissociation of NO_2 (R6) that was formed from NO before (R4 and R5). It is unlikely that this would allow obtaining meaningful results because the Zeldovich mechanism is known to require distinctly higher gas temperatures [108]. Moreover, an influence of $NO_2(\nu)$ as an explanation for the NO production at lower temperature is already known from Shimizu *et al.* [81]. Therefore, in (R1) two reactions are combined whose individual influence cannot be distinguished based on the available information. An individual consideration would require knowing the vibrational energy distribution function (VEDF). An assumption about their shape could be made and used to fit a vibrational temperature. For the present task, this method would not have any advantage over a direct fit of the reaction rate for (R1) and the latter approach seems more expedient. Therefore, different from all other reactions, (R1) was considered with a fictitious reaction rate that was obtained from a fit to experimental data.

Energy input and residence time The equation system is solved in a volume element co-moving with the average gas flow. For the complete process, a constant temperature is assumed in the first instance. Depending on the flow rate, the considered volume element resides in the discharge for a certain time t_R. The pressure-dependent value of t_R has already been determined during the device development and is depicted in figure 1.3. During t_R, a source term for atomic oxygen O was included in the simulation to model the energy input. The production rate of O was set to a constant value that was used as a second fit parameter besides the rate of (R1). Both the O production rate and the reaction rate for (R1) were fitted to the pressure-dependent transition temperature from O_3 to NO production.

Results and reaction pathways As a result of this fitting strategy, the model is able to simulate the pressure-dependent transition temperature very accurately, but underestimates the concentration of all the three most abundant reactive species. However, the calculated concentrations are still in the same order of magnitude as the measured ones. Figure 3.5 compares measurement and simulation, while the simulated densities of O_3, NO and NO_2 are corrected by a factor of 2, 4 and 1.5, respectively.

By investigating the reaction pathways, it becomes apparent that (R1) is the dominant NO formation mechanism. (R2) is counteracting as the most effective NO decomposition process, bringing NO, N and O in an equilibrium. With a lower rate compared to (R1), (R3) acts as an additional formation mechanism for NO. In an environment containing O and O_3, NO is not stable. This is evident from reactions (R4) and (R5) that both produce NO_2. The corresponding back reaction is (R6). Comparing both formation mechanisms of NO_2 considered in the model, (R5) has a higher influence, although the NO_2 production rate via (R4) is in the same order of magnitude. For the lowest considered pressure of 200 mbar near the maximum temperature, (R4) becomes even more effective than (R5). The formation of O_3 is modeled in (R7) that is one of two three-body reactions besides (R4).

Distinguishing the influences of pressure and residence time The presence of three-body reactions explains the distinct pressure-dependent behavior of the model, but interestingly this is not the only reason for the pressure dependent output. This becomes apparent from an altered model version that sets $[O_2]$ and the density of the arbitrary

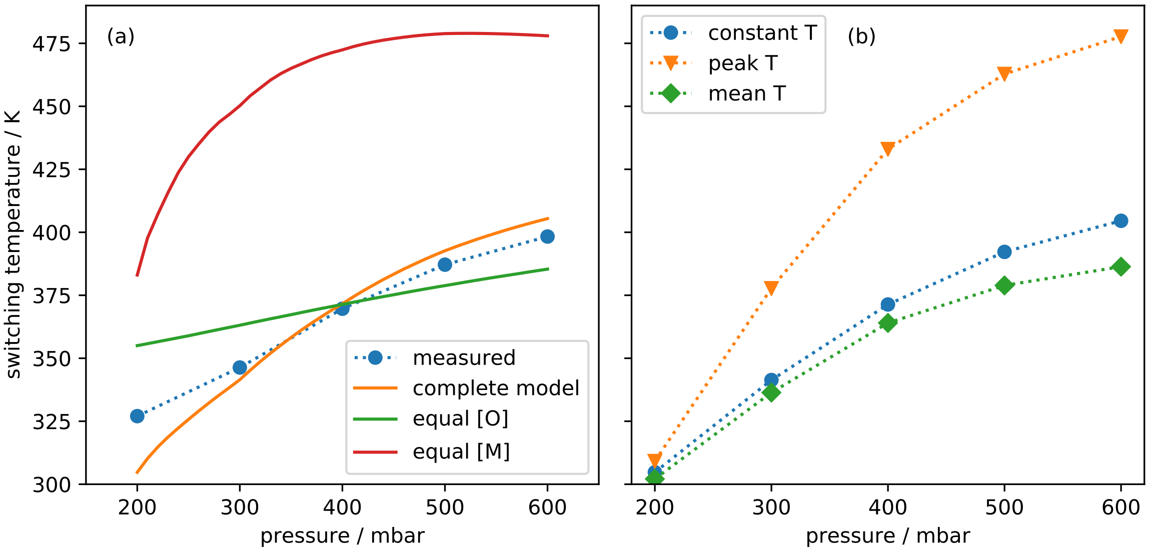

Figure 3.6.: (a) Comparison of O_3 to NO switching temperatures from the measurement and the different model versions. (b) Original model (constant T) in comparison to peak and average value in the model version assuming a linearly increasing temperature. Taken with permission from [16], © IOP Publishing Ltd.

collision partner M for (R4) and (R7) constant using the values prevailing at atmospheric pressure ($[M] = 2.5 \cdot 10^{19}\,\mathrm{cm}^{-3}$, $[O_2] = 5.0 \cdot 10^{18}\,\mathrm{cm}^{-3}$). The altered model still generates results that are qualitatively pressure dependent as a consequence of a primary constructive aspect of the device in investigation: Both gas flow and pressure are set jointly using the throttle valve at the inlet.

As a result from the coupling of pressure and flow rate, the residence time of species in the active zone is coupled to the pressure as well. This has been depicted during the characterization of the device already in figure 1.3 and considered in the model as duration of the initial O production. Consequently, the simulation uses a constant input power, but a pressure dependent input energy. Another altered version of the model sets the residence time and hence the input energy constant. In figure 3.6a), the pressure dependent O_3 to NO transition temperature for all model versions is compared to the respective results from the measurement.

Influence of the temperature distribution on the model

In the experiment, the gas temperature is not measured directly, but instead the surface temperature of the inner electrode is determined 3 mm behind the active zone in flow direction using a pyrometer. Resulting from the distance to the active zone and the cooling of the inner electrode caused by the driving gas flow through its center, the measured temperature is most likely lower than the peak gas temperature in the active zone. Moreover, the temperature distribution in the active zone is allowed for neither in the measurement nor in the simulation; due to the continuous energy input during the residence in the active zone, a temperature increase in flow direction can be assumed until the end of the active zone. This motivates an investigation of the sensitivity of the model to an inhomogeneous temperature distribution.

A further model version aimed at investigating this aspect was created assuming ambient temperature at the input and a linear temperature increase in flow direction until the end of the active zone. Thereafter, the assumed temperature linearly decreased to ambient again in the same timespan, however the system was significantly less sensitive to temperature changes in this section than in the active zone. Figure 3.6b) compares the model versions regarding the calculated pressure-dependent O_3 to NO transition temperature.

It becomes apparent that the maximum temperature during transition is distinctly higher than the value obtained from the original model assuming a constant temperature. However, the latter value is in good agreement with the average temperature prevailing in the case with linearly increasing temperature. More important, the qualitative evolution of the transition temperature over pressure is identical in each case and the deviations decrease with falling pressure. This supports the primary result of the investigation that a NO production is possible close to ambient temperature under reduced pressure.

3.3.2. Implications from the results

The described model is well-suited to emphasize which reactions have the most pronounced influence on the generated species composition. This is facilitated by its simplicity, what comes at the expense of its usefulness for a reliable extrapolation of results beyond the measured parameter ranges. However, the combination of experiments and model provides an insight into the way pressure and temperature influence the species composition. This is shown in figure 3.7 and allows deducing suitable operating strategies for the VDBD concept. In general, an adaption of pressure to switch from an O_3- to a NO_x-dominated plasma chemistry is equivalent to an adaption of temperature, however under practical standards some peculiarities need to be taken into account.

To constructively enhance the usable pressure range downwards while preserving the flow rate, a more powerful pump is required and consequently the production costs rise. To increase the operating pressure, a higher minimum voltage is required for operation. For this, the supply circuit as well as clearances and insulations to prevent spark-overs in the device need to be constructed accordingly. Within the constructive boundaries of the device, a pressure variation can be realized instantaneously and monitored by an economic and reliable sensor. In contrast, a temperature variation is time-consuming and requires a variation of power in order to limit the flexibility demanded from the cooling system. Due to the strong temperature inhomogeneity, a reliable measurement is challenging. Perspectively, the user would certainly prefer a device that instantaneously switches between the two modes. This implies a usage of pressure as the primary control mechanism to avoid the necessity to wait for a temperature adaptation for practical reasons. However, neither the O_3- nor the NO-production is efficient at temperatures

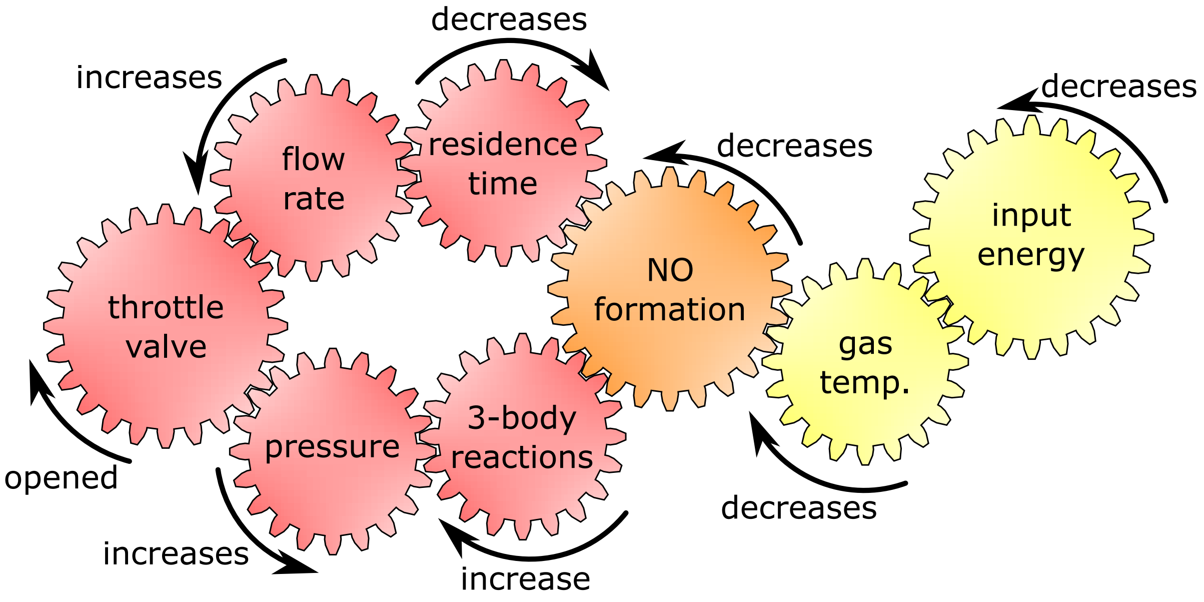

Figure 3.7.: Central mechanisms influencing the species production.

near the transition temperature. Therefore, depending on the actual application requirements, an additional temperature variation might be unavoidable to increase the $[O_3]/[NO_2]$ ratio or the $[NO]/[NO_2]$ ratio, respectively.

The presented correlations are valid for a process gas consisting of ambient air near room temperature and intermediate relative humidity. An additional humidification of the process gas requires a dedicated investigation of the produced reactive species using a water separation at the MPC inlet and complementary liquid diagnostics [57, 109]. In any case, for a reliable process control both pressure and temperature need to be measured reliably. While the pressure measurement does not seem to be difficult, the determination of gas temperature needs to be improved vastly before the concept can be implemented in a convincing prototype.

4. Monitoring and controlling the process

Essential correlations between the different input parameters and the species composition produced by the VDBD have been found at this point. Furthermore, the underlying mechanisms are well enough understood to purposefully use them as a basis for a monitoring and control process. Pressure and temperature are crucial for the output gas composition, but only the former can be measured in a simple way. Therefore, the main focus for the further development will be set on the temperature determination.

The initial prototype has not been constructively prepared for a gas temperature measurement, and the unwieldy indirect pyrometer-based measurement obstructs a flexible application of the system in the medical practice. Therefore, a subsequent prototype featuring a suitable measurement facility had to be developed. The device is depicted in figure 4.1 and in detail presented in section 1.2. It is intended to evaluate a manufacturing primarily based on a laser cutting process. Moreover, the new geometry allows a more efficient simulation of gas flows and the temperature distribution. This information allows comparing temperature values measured at different locations and therefore helps developing new measurement strategies. On this basis, it will be investigated whether the gas temperature can be deduced from electrical quantities.

4.1. Simulating the temperature distribution

As a tool to assess the temperature distribution in the discharge zone, a three-dimensional computational fluid dynamics (CFD) simulation has been set up using COMSOL Multiphysics®. The simulation software includes the "Conjugate Heat Transfer" module that has been used as the basis for the present model. The problem is considered laminar, because the Reynolds number Re at the narrowest sections is only around 1000, while a transition to a turbulent flow can be expected when Re is not distinctly below 2300 [110]. Moreover, no geometrical features critical for turbulences such as steps are present. Details regarding the CFD simulation can be found in appendix A.

Figure 4.2 shows the geometry used to simulate the actual device and highlights the gas in- and outlets. The inlets of both process gas and cooling gas are specified as boundaries with both a specified temperature and a specified flow rate. The laminar inflow boundary condition is used to realize the latter condition as it allows obtaining a fully developed flow profile at the inlets. The specification of a flow rate causes the software to include an additional equation that calculates the inlet pressure to achieve the desired flow rate [111]. For the outlets, a fixed pressure value is specified instead.

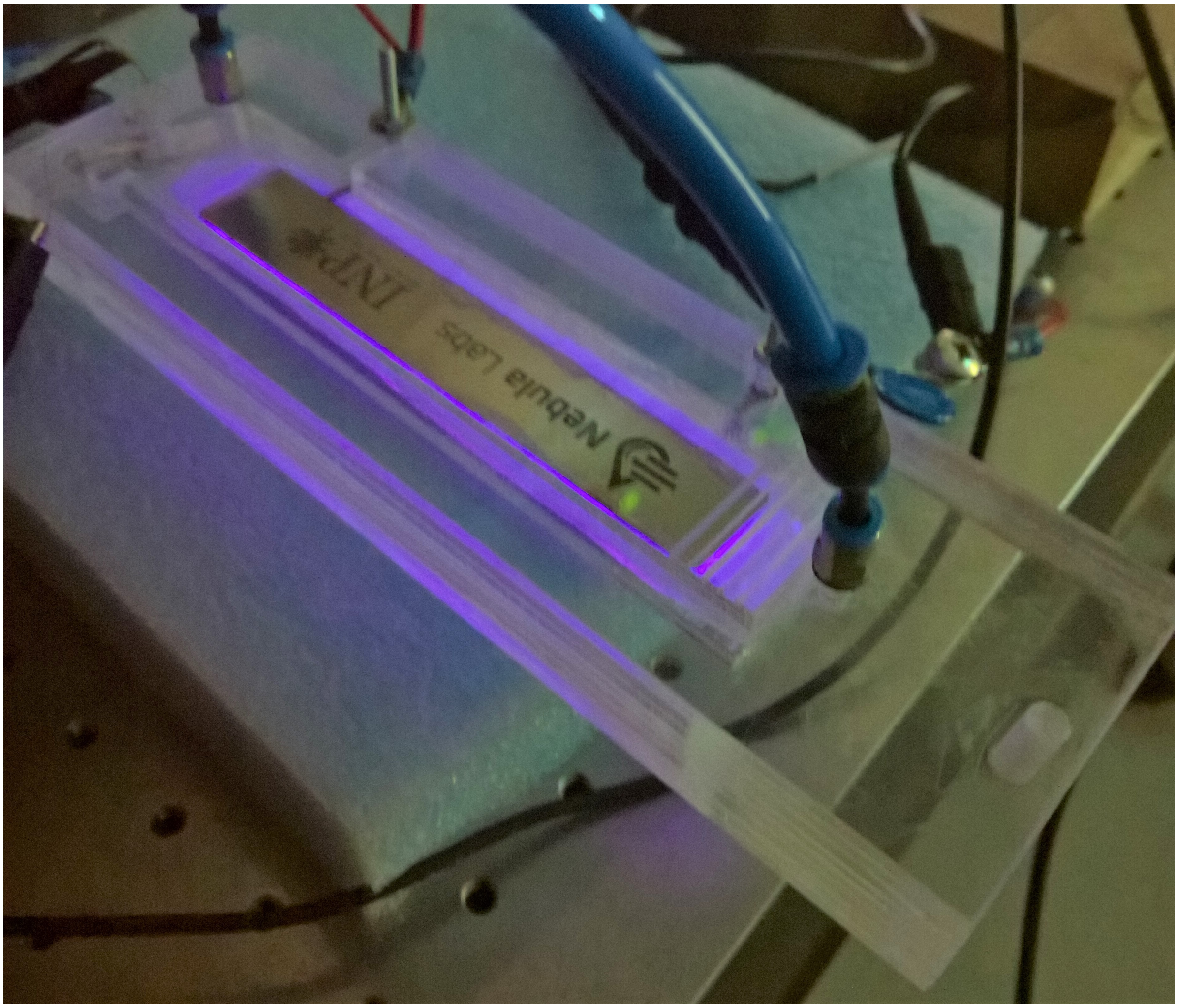

Figure 4.1.: Prototype optimized for efficient manufacturing and calculations.

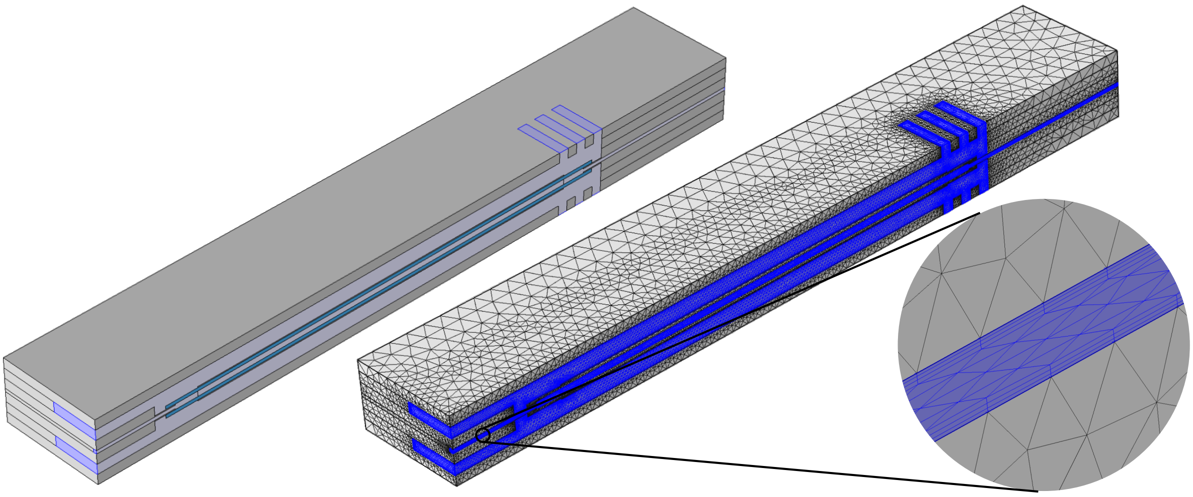

Figure 4.2.: Geometry used to model the VDBD prototype. Left: Overview, inlets and outlets highlighted in blue. Right: Mesh used in CFD simulation, regions highlighted in blue correspond to fluid.

The Venturi pump itself is not calculated, because its only relevant effect in this context is that it provides a technical way to realize the desired process gas outlet pressure. For the cooling gas outlet, a pressure of 1 atm has been set. Natural convective cooling boundary conditions were specified for the outer sides of the device. This facilitates a good agreement between simulated and actual system behavior, however it obstructs the usage of a horizontal symmetry plane to speed up calculations. While the assembly is geometrically symmetric, the convective cooling properties of top and bottom sides differ considerably. A vertical symmetry can be exploited nevertheless. The discharge is considered as a region where a constant power density is heating the process gas that is initially calculated from the actually dissipated electrical power.

The model is solved for the time-dependent flow velocity field and temperature considering an overall operation time of 2200 s to ensure reaching stationary conditions. In advance, the stationary flow velocity field for the isothermal case is calculated and used as a set of initial values for the time-dependent calculation. This avoids issues in finding suitable initial values and speeds up parameter sweeps using different input power values; the stationary field does not need to be recalculated meanwhile. The time-dependent solution for one input power value then requires a computation time of approximately 5 h on a platform featuring two Intel® Ivy Bridge-EP microprocessors with 12 physical cores each and 128 GB of RAM. For the geometrical discretization, 2 million elements are used in total. The largest part of the volume is discretized using tetrahedrally shaped cells, while three layers of flat prism cells were used as boundary layers in the fluid regions adjacent to walls as depicted in figure 4.2. Pyramid-shaped cells provided a geometric transition between the two other cell shapes. The motivation for choosing the described cell structure arises from the fact that the model solves the Navier-Stokes momentum equation for the velocity field. Figure 4.3a) depicts a parabolic flow velocity field typical for a laminar tube flow. Moreover, the resulting derivative of the velocity to the radius

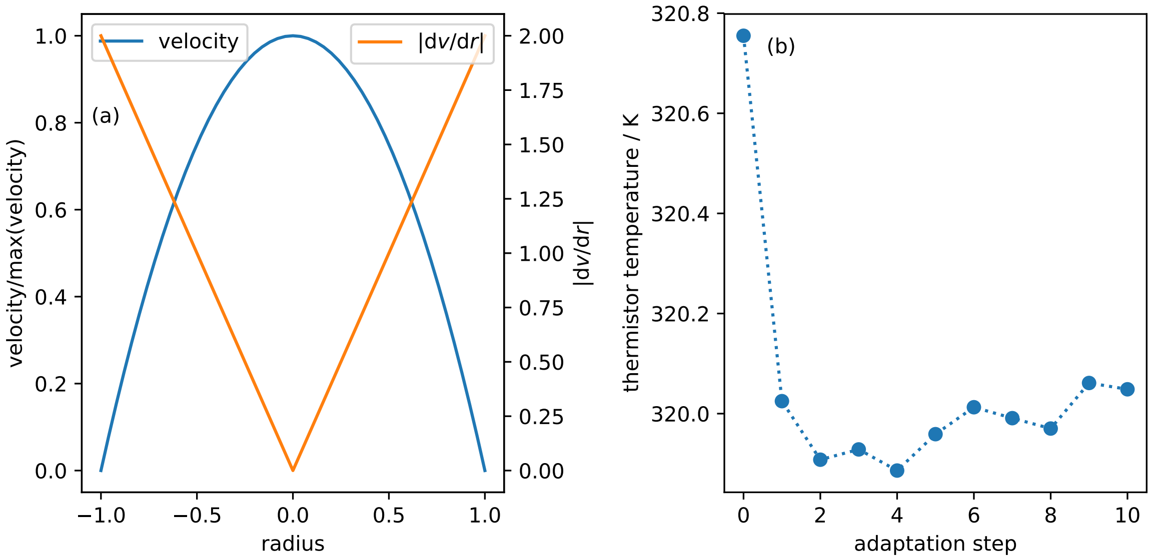

Figure 4.3.: (a) Idealized flow velocity profile and derivative of velocity to radius. (b) Calculated stationary temperature at the thermistor with the original mesh (step 0) and for ten subsequent mesh adaptation steps.

is shown. In order to both accurately model the properties of the flow and facilitate the solution to converge, the regions with a larger velocity gradient need to be meshed finer. Hence it is suggestive to use thin, slightly elongated boundary layers in the outer region of the channel while keeping the elements in the middle of the flow a little larger.

The mesh quality has been assessed using a sample calculation at a pressure of 200 mbar and an input power of 3.7 W with the automatic mesh adaptation implemented in COMSOL Multiphysics® in ten subsequent steps. The resulting stationary temperature values at the thermistor deviate only to a negligible extent from the results obtained with the original mesh. From this finding depicted in figure 4.3b), it is concluded that the no relevant discretization error is introduced by the mesh.

In order to use the simulation as a tool to assess a new temperature measurement method, it needs to be verified itself before. This requires a proven temperature measurement method that can be used as a benchmark for the computational temperature determination. This proven temperature measurement method complementary to the new approach to be developed could also provide an additional control parameter in a later application. Therefore, the actual device needs to be equipped with a measurement facility that can both benchmark the simulation during the development and perspectively be part of a reasonably simple and economic further prototype.

4.2. Measuring the gas temperature in a dielectric barrier discharge

In the discussion about the development of a temperature measurement for the initial VDBD prototype in section 3.2, two standard methods for temperature measurement in non-equilibrium discharges have been named. These are the application of fiber-optical probes as well as optical emission spectroscopy (OES). Both methods can be suitable for laboratory investigations, but not as a constructive means that can be adapted to an integrated, marketable product. Integrating an OES-based temperature measurement in a device is not conceivable under practical standards. Both the development effort to automatize the evaluation of emission spectra and the financial expenses for the manufacturing would be unacceptably high. Moreover, the common assumption that the actually measured rotational temperature equals the gas temperature is not necessarily justified for low temperatures [98]. If properly installed, commercially available fiber-optical probe systems reliably deliver gas temperature values without the necessity of any post-processing. However, they are expensive and the probe tips can be dismanteled by the plasma, which can reduce the lifetime below a threshold acceptable for a daily-use product. Measuring outside the discharge circumvents this issue, but yields flow rate-dependent results that are futile as soon as the gas flow is switched off completely. Consequently, in order to direct the further development to a versatile prototype rather than to a laboratory-specific setup, both the standard methods have been discarded.

4.2.1. The thermistor as complementary device

A reliable and adequately exact gas temperature measurement that is proven for a variety of process control applications can be performed using a thermistor. Compared to a fiber optical probe or the application of emission spectroscopy, one central drawback of thermistors needs to be taken into account though. While parts providing a high chemical resistance, e.g. by a glass encapsulation, are available, a thermistor can generally not be used for measurements directly in the discharge zone. In such a setup, the thermistor would act as an unwanted electrode, strongly disturbing the voltage drop over the component and hence render the measurement invalid, if not destroy the thermistor or parts of the connected circuit.

In the outlet channel in proximity to the process chamber, the thermistor can be integrated. The small dimensions of the chosen TDK B57540G1 part simplify this process. Changes in the heat transport from the discharge to the thermistor can lead to variations in the measured value. This is in particular relevant for a varying gas flow that accompanies the constructively envisaged pressure variations. In the case of a closed inlet valve and therefore a prevented gas flow, a thermistor in the outlet cannot deliver any valid data. However, it can be suitable as a complementary method to validate the CFD simulation and another measurement method in the flow-enabled case.

4.2.2. Deduction and discussion of a new hypothesis

In order to determine the gas temperature, electrical parameters of the discharge will be evaluated. A simple but proven electrical model for DBDs is well-known and allows calculating the voltage drop over the discharge $u_\mathrm{g}(t)$. As a prerequisite for the inception of a discharge, u_g needs to reach a certain value to generate a sufficiently strong reduced electric field $|\vec{E}|/N$. The latter is necessary to ensure that Townsend's ionization coefficient α is high enough for a self-sustaining discharge (cf. appendix B).

For the initial start-up after the device was switched off for a long time, the reduced electric field in the gap can even be stated analytically as

$$\left(\frac{|\vec{E}|}{N}\right)_\mathrm{init} = \frac{u_\mathrm{g} \cdot k_\mathrm{B} \cdot T}{d \cdot p} \propto \frac{u_\mathrm{g} \cdot T}{p}. \tag{4.1}$$

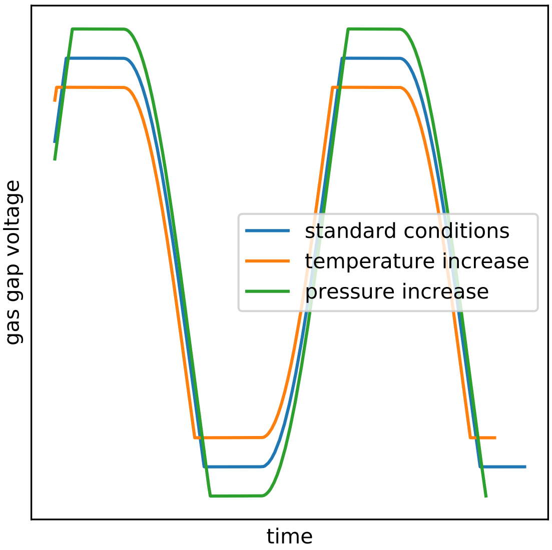

Figure 4.4.: Expected influence of temperature and pressure on the gas gap voltage u_g.

This requires the Boltzmann constant k_B, the temperature T and the distance between the dielectrics d as well as the pressure p. As it is highlighted in equation 4.1, for a given geometry the combination of u_g, T and p determines the discharge inception. Particularly important in the present context is that a rising temperature allows an ignition at lower voltage while the pressure remains constant.

After the device has started, it operates in the self-pulsing mode that is typical for sine-driven DBDs. This involves two re-ignitions in each voltage cycle, however a description of $|\vec{E}|/N$ necessary to initiate the re-ignition using equation 4.1 would not be valid. Due to the short time between two subsequent active phases in the self-pulsing operation, a residual ionization needs to be taken into account for re-ignition [78]. Moreover, an accumulation of charges at the dielectrics surfaces substantially influences the externally imposed electrical field [112].

Nevertheless, an influence of pressure and temperature on the gas gap voltage in the active phases can be observed also during the self-pulsing operation. This is exemplarily depicted in figure 4.4. If the influence of residual ionization and charge accumulation on the correlation of u_g, T and p is only weakly dependent on T and p themselves, this could be used for a gas temperature determination during operation. The factor $u_\mathrm{g} \cdot T/p$ could probably be used to approximately describe the system, although it would quantitatively differ compared to the initial inception. As shown in section 4.3, it can still be used to calculate the temperature from a calibration constant c_cal recorded at a

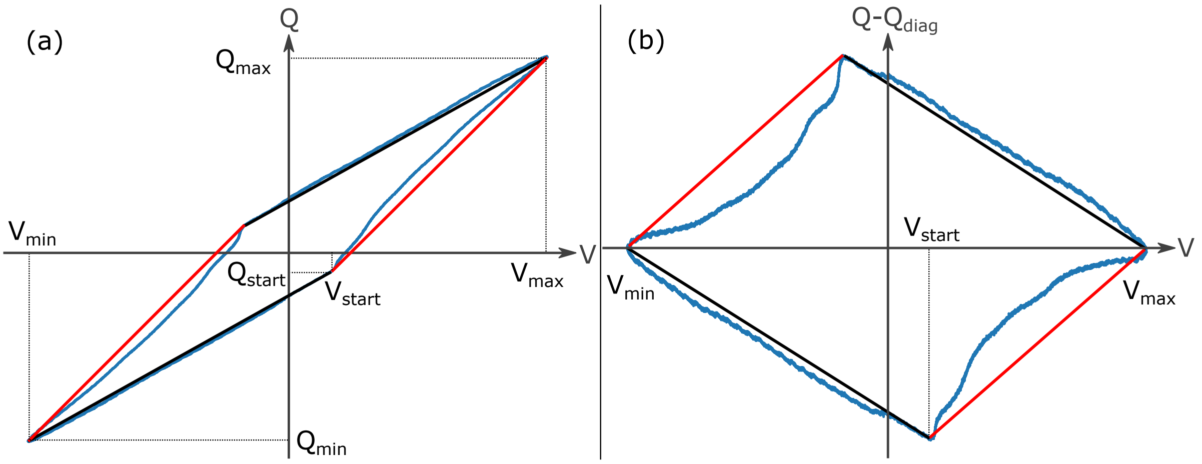

Figure 4.5.: (a) Example of a measured Q(V)-plot in blue, idealized plot in black (inactive phases) and red (active phases). (b) Distorted Q(V)-plot obtained from subtracting the values Q_{diag} on a line through $(V_{\mathrm{min}}, Q_{\mathrm{min}})$ and $(V_{\mathrm{max}}, Q_{\mathrm{max}})$ from Q. Taken with permission from [62], © IOP Publishing Ltd.

defined temperature T_{cal}

$$c_{\mathrm{cal}} = \frac{u_{\mathrm{g}} \cdot T_{\mathrm{cal}}}{p} \tag{4.2}$$

and the quantities u_{g} and p, i.e.

$$T = \frac{c_{\mathrm{cal}} \cdot p}{u_{\mathrm{g}}}. \tag{4.3}$$

4.3. Testing the new hypothesis

In order to put the hypothesis that eventually lead to equation 4.3 on a sound theoretical basis, a considerable expenditure for modeling basic plasma processes would be necessary. This effort would not be sustainable for an idea that in the worst case does not work in practical terms, which is why an experimental validation has been preferred. Thus, the investigations covered below were performed on the thermistor-equipped VDBD prototype using simple Python-based process control scripts implementing the basic hypothesis for temperature determination.

4.3.1. Preliminary considerations

A first step to make a temperature measurement based on u_{g} usable is a reliable measurement of it. Although it cannot be directly measured, u_{g} is in principle easily accessible provided that voltage and charge can be measured. Section 2.4.2 presents a simple equivalent circuit that allows calculating u_{g} by subtracting the voltage drop over the dielectrics from the overall voltage. An expedient usage of u_{g} to diagnose and monitor the discharge however requires that the self-pulsing operation of DBDs is taken into account; inactive and active phases are alternating. The value of u_{g} crucial for diagnostics

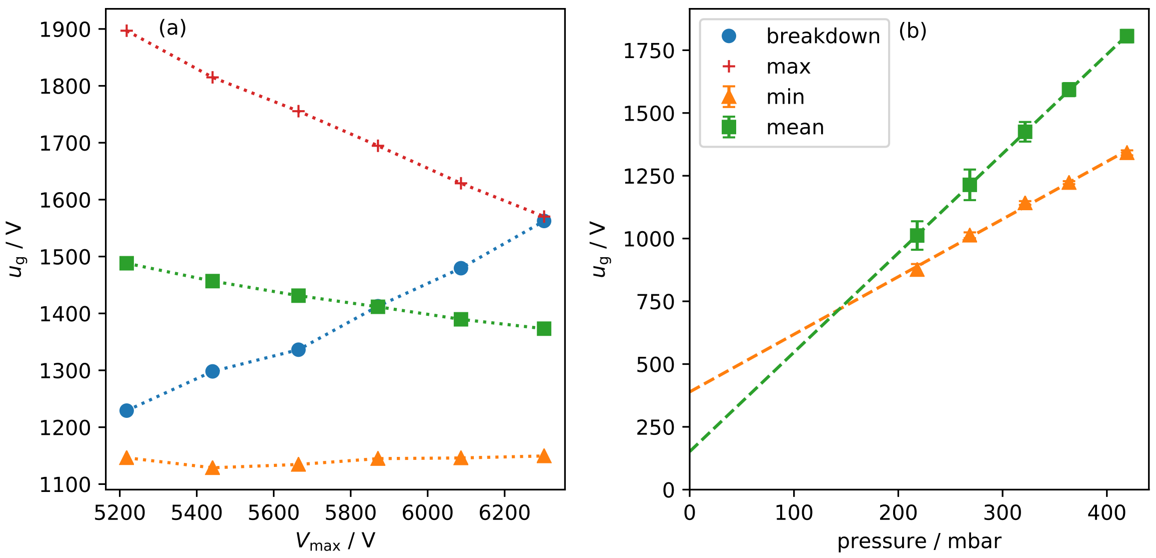

Figure 4.6.: (a) Development of characteristic values of u_g in the rising active phase over the external amplitude at 300 mbar. (b) Characteristic values of u_g averaged over all considered voltage amplitudes for different pressure levels. Taken with permission from [62], © IOP Publishing Ltd.

purposes is the value within the active phases, when it represents the voltage drop over the discharge. Therefore, start and end time of the active phases need to be detected reliably and reproducibly first.

Figure 4.5 depicts an example of a Q(V)-plot that was distorted by subtracting the values on a line through $(V_\mathrm{min}, Q_\mathrm{min})$ and $(V_\mathrm{max}, Q_\mathrm{max})$ from Q. The benefit of this procedure is that it maps the “corners” of the Q(V)-plot marking the beginning of active phases to an extremum problem; the active phases *start* when $Q - Q_\mathrm{diag}$ reaches its global maximum or minimum. In view of the fact that the *end* of active phases can easily be found as minimum or maximum of Q, the distorted Q(V)-plot can serve as a key tool to computationally distinguish inactive and active phases in the voltage cycle.

A handy side effect of this method being available is that it can be used to determine the capacitance of the dielectrics C_d as well. For the calculation of u_g, this value is crucial. Q(V)-plots have been recorded at different external voltage amplitudes and a constant pressure of 200 mbar in a preliminary investigation. By evaluating the slope between beginning and end of the active phases in these plots, $C_\mathrm{d} = 24.3\,\mathrm{pF}$ has been measured for the DUT.

During the active phases, u_g is not constant in the present system. Instead, it decreases after discharge inception and increases again towards the end of the active phase. In order to use u_g for temperature determination, a value characteristic for the system state needs to be found. Figure 4.6a) shows an overview about the unwanted influence of the external voltage amplitude on four characteristic values of u_g in the active phase. The values in question are the one directly at the

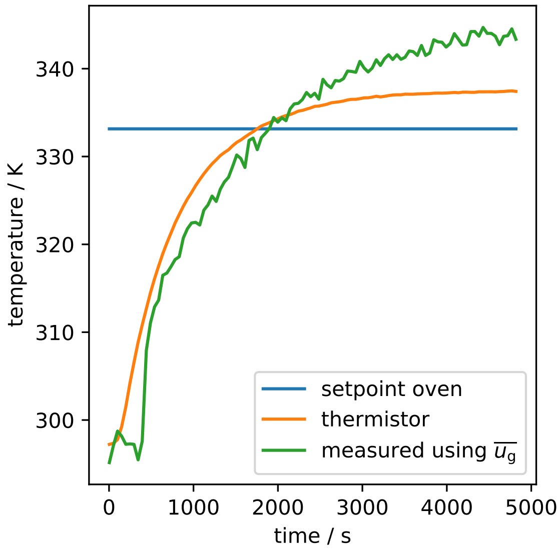

Figure 4.7.: Comparison of the temperature measured using the thermistor and the respective value calculated from $\overline{u_{\mathrm{g}}}$ while the DUT is placed in a temperature-controlled oven. Taken with permission from [62], © IOP Publishing Ltd.

beginning of the active phases representing the breakdown as well as the minimum, average and maximum value. While both the “breakdown” and the maximum value distinctly depend on the external amplitude, the minimum and average value can be used without considering an additional dependence for moderate variations of the external amplitude.

In figure 4.6b), the dependence of the characteristic values on the pressure is depicted. To allow an unambiguous assignment, the characteristic values of u_{g} have been averaged over all considered voltage amplitudes for each pressure level before. As this procedure does not seem to be expedient to process the “breakdown” and maximum values due to their pronounced voltage dependence, they have been omitted for this step. All measurements were performed at constant (ambient) temperature by now, consequently u_{g}/p should be constant according to the hypothesis. Regarding the minimum and average as characteristic values of u_{g}, the prerequisite is not fulfilled for the minimum value, because it would require considering an additional axis intercept b in the form $(\min(u_{\mathrm{g}}) + b)/p = \text{constant}$.

As $b \approx 0$ when using the average as characteristic value of u_{g}, it will be used for the temperature calculations. For brevity, it will be referred to as $\overline{u_{\mathrm{g}}}$.

4.3.2. Exemplaric temperature measurements

It has not yet been validated that the proposed method is actually suitable for a temperature determination. Consequently, the first measurement scenario in the present stage of development aims at determining a known temperature. This is achieved by placing the DUT in a temperature-controlled oven, where it was heated from room temperature to 333 K over a time of 75 min. Figure 4.7 depicts the results obtained from this measurement and shows a slight discrepancy between the oven setpoint and the quasi-stationary value measured by the thermistor. This seems to indicate that the temperature sensor integrated in the oven is inaccurate, what has no effect on the present measurement task.

More important is that the temperature tends towards a stationary value that is expected to be spatially constant all over the oven. According to the sensor in the oven, the air in it reached the target value after about three minutes of controlled heating.

In the time thereafter, the temperature of the complete DUT slowly adapted to the air temperature. Therefore, the measurement with the thermistor and the one based on $\overline{u_\mathrm{g}}$ should deliver identical values in an ideal case. The quantitative and qualitative agreement between both values is adequate indeed. In order to measure the temperature based on $\overline{u_\mathrm{g}}$, the DUT needed to be switched on. As this leads to an additional heating in the discharge zone, the device was only operated every 45 s for about 2 s. Using an operating pressure of 200 mbar allowed restricting the dissipated power to 5 W. Therefore, no significant influence of the discharge on the temperature distribution is expected. With regard to the promising results in the measurement of a known temperature, the new method is now applied to monitor the temperature increase during normal operation. Figure 4.8 shows both the values calculated from $\overline{u_\mathrm{g}}$ in this setup as well as the temperature measured simultaneously using the built-in thermistor. During this measurement, the Venturi pump was operated directly at the main gas supply for pressurized air. The latter is fed by a compressor via a reservoir. The system provides a pressure of 5.5 bar, resulting in a high main gas flow of 23 slm. Due to the high flow rate, the reservoir pressure decreased in intervals of about 500 s to the threshold pressure that lets the compressor start. During the compressor operation, the line pressure is slightly higher.

The described pressure variations cause a concomitant variation in the performance of the Venturi pump and therefore lead to slight pressure variations in the DUT's process chamber. To what extent this phenomenon occurs depends on the nominal pressure setting, and in addition it is superimposed on a slight pressure increase observable with rising temperatures. These effects cause the pressure to deviate from the nominal value and thus vary by 13...46 mbar depending on the operating parameters. Therefore, the software implementing the proposed measurement method reads the data from a MKS Baratron® pressure transducer to obtain the currently prevailing pressure value for the calculation.

By using the throttle valve at the process chamber inlet, the nominal pressure was set for each measurement to 200, 300 or 400 mbar. This led to process gas flow rates of 1.2, 1.8 or 2.9 slm. In the outer housing, an additional air flow of 10 slm was lead over the electrodes to provide a cooling effect. During the considered time span of 2000 s for low power measurements and 1200 s for measurements using high input power values, the device was operated continuously. For calibrating the $\overline{u_\mathrm{g}}$-based measurements, the temperature measured by the thermistor at the beginning of the measurement were used.

4.3.3. Verification of the results

Analyzing the reaction on pressure variations

In figure 4.8, artifacts are apparent on the curves that seem to correlate with the described pressure variations, necessitating a sensitivity analysis aiming at the correlation between pressure and calculated temperature. For this, the Venturi pump at the DUT was operated using a flow controller to allow simulating the varying performance of the main line in a controlled way. In order to keep the actual temperature of the device

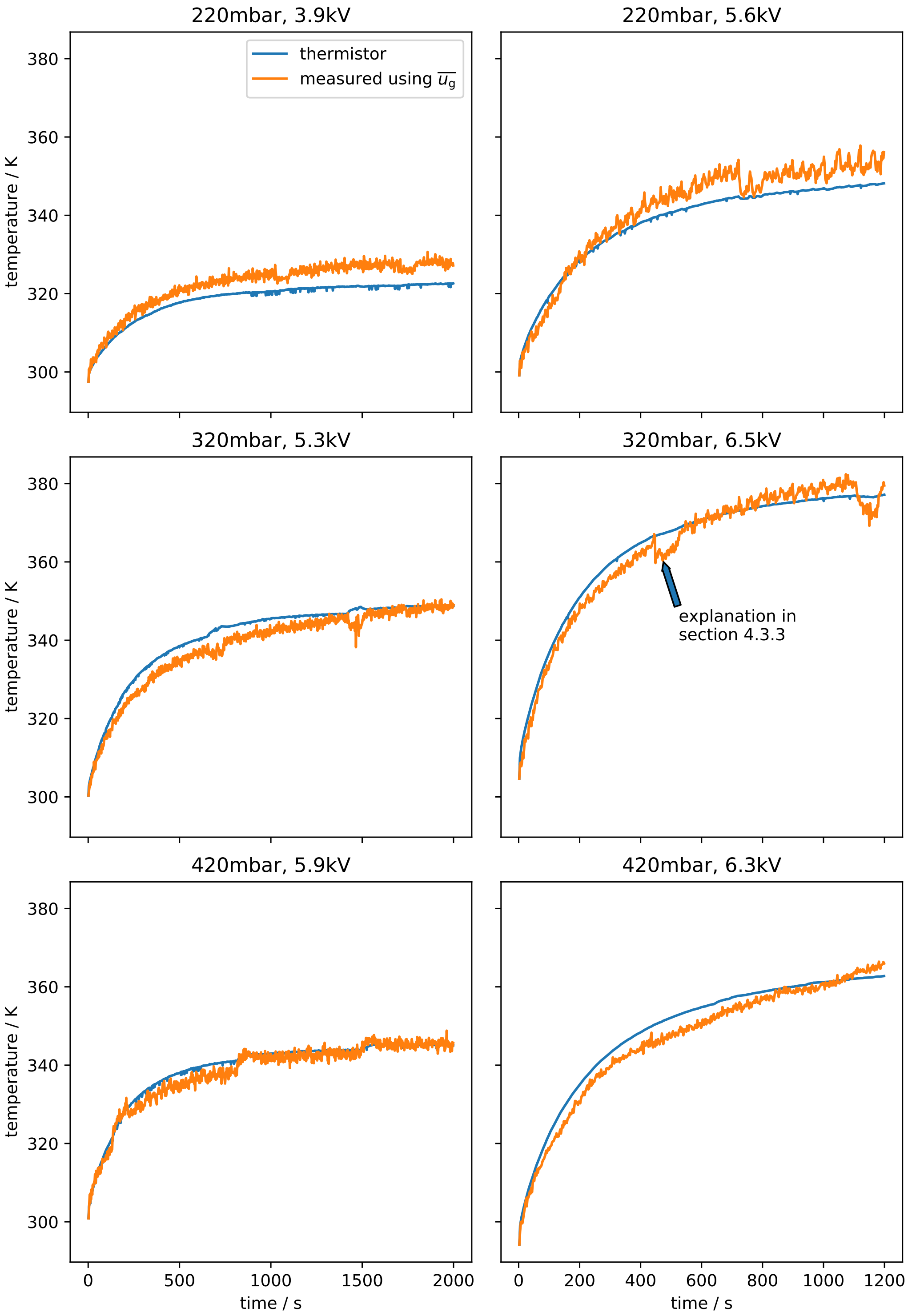

Figure 4.8.: Comparison of temperature values measured using the thermistor and calculated from $\overline{u_g}$ during the heat-up process of the DUT in normal operation. Taken with permission from [62], © IOP Publishing Ltd.

constant, it was operated for only two seconds to enable a single measurement. Between two subsequent measurements, a waiting period of 60 s was included. Figure 4.9 depicts the response of the calculated temperature values to the controlled pressure variations. Both a pressure decrease by 18 % and an increase by 13 % lead to a distortion of the calculated temperature values by approximately 2 %.

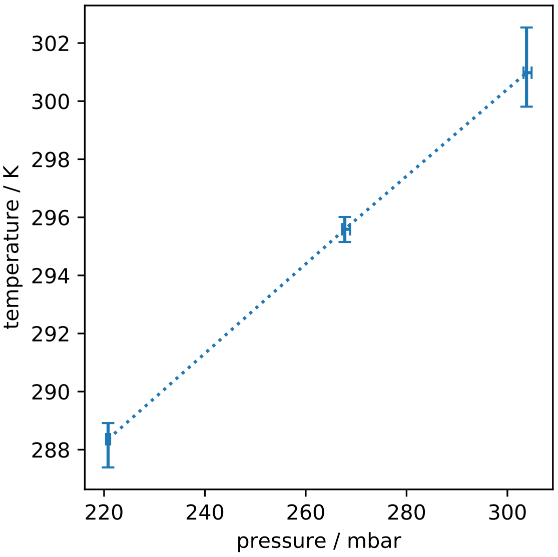

Figure 4.9.: Controlled pressure variation and its unwanted influence on the measured temperature value. Taken with permission from [62], © IOP Publishing Ltd.

Therefore, the artifacts present on the curves in figure 4.8 can be slightly intensified by a direct, undesired influence of pressure, but beyond this they seem to represent actual temperature variations. As a decreasing pressure is accompanied by an increasing flow rate, it can plausibly be linked to a temperature decrease. A decreasing pressure furthermore influences the dissipated power. At a constant voltage amplitude, the power tends to decrease as well (this is depicted for the old prototype in figure 1.3), but depending on the operating point an influence on the high voltage supply is possible. This leads to an increase of the amplitude and eventually of the power, particularly apparent in the dataset for 420 mbar/5.9 kV. With a rising power, the temperature can plausibly rise as well. Coincident reactions of the thermistor also indicate that the artifacts on the curves are linked to actual temperature variations.

Assessing the quantitative reliability

The values calculated from $\overline{u_\mathrm{g}}$ deviate to a certain extent from the values measured with the thermistor. This could indicate a limited precision of the proposed method, however an exact agreement cannot be expected even in an idealized case. This is caused by the spatial distance between the measurement spots. While the thermistor is located in the outlet channel, the $\overline{u_\mathrm{g}}$-based method is supposed to measure a temperature prevailing in the active zone.

The thermistor mounted in the DUT can not only be used to benchmark the $\overline{u_\mathrm{g}}$-based temperature measurements, but the CFD simulations described in section 4.1 as well. While the very small thermistor itself is not geometrically modeled, the temperature prevailing at the respective location is evaluated. This reveals that the heating is overestimated first. Comparing the complete physical system to the substantially simplified model reveals a highly probable reason for this observation: The dissipated electrical

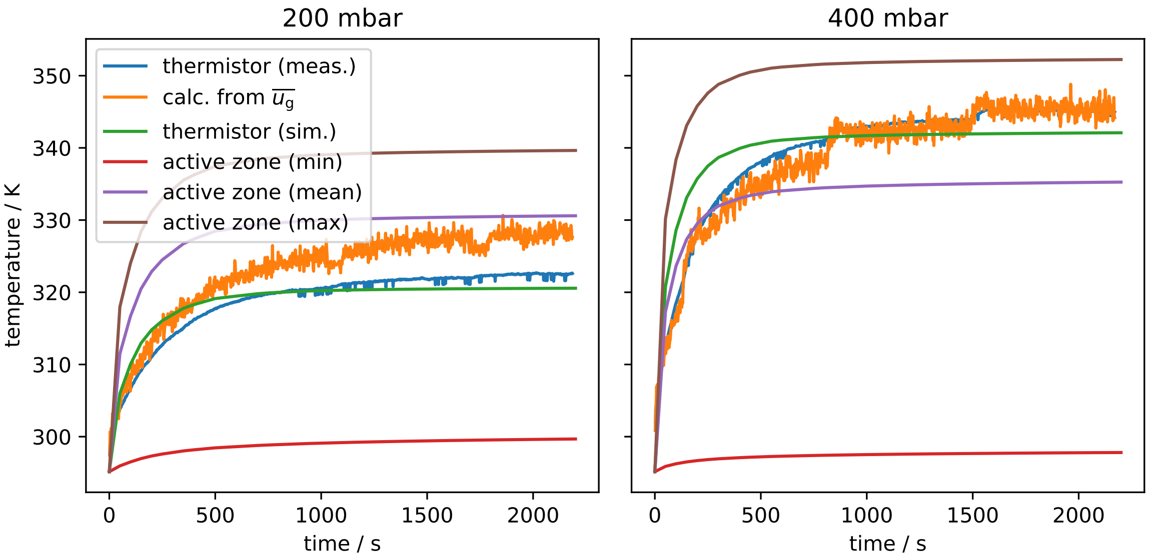

Figure 4.10.: Temperature values calculated from $\overline{u_g}$ in comparison with the temperature distribution calculated by a computational fluid dynamics simulation for the process chamber. Taken with permission from [62], © IOP Publishing Ltd.

power is not only used for heating (a usual assumption in electronics), but also converted to radiation and, according to the purpose of the device, transferred to chemical reactions. To avoid modeling these processes, the temperature at the thermistor is fitted to the measured data using the input power as a parameter. This results in a value for the power that is expected to be in better agreement to the actual heating power than the overall dissipated electrical power.

Figure 4.10 compares two of the previous time-dependent measurements with the respective simulations. In addition to the temperature data calculated from $\overline{u_g}$ and both the measured and the simulated thermistor temperature, the temperature span calculated for the active zone is depicted. It becomes apparent that the measurement based on $\overline{u_g}$ is in the temperature range prevailing in the active zone and coarsely resembles its average value. The simulated spatial temperature distribution in the device after an operation time of 2200 s is shown in figure 4.11.

Reviewing the effective capacitance of the dielectrics

An improvement of the quantitative reliability could facilitate a better detection of characteristic values in the temperature range in the active zone. In order to preclude a negative influence of a possibly inaccurate determination of the effective capacitance of the dielectrics C_d, its value is validated with complementary methods. For the determination of C_d, different approaches can be used as described in section 2.4.2. Analytically, it can simply be calculated from the dimensions and the permittivity as two idealized

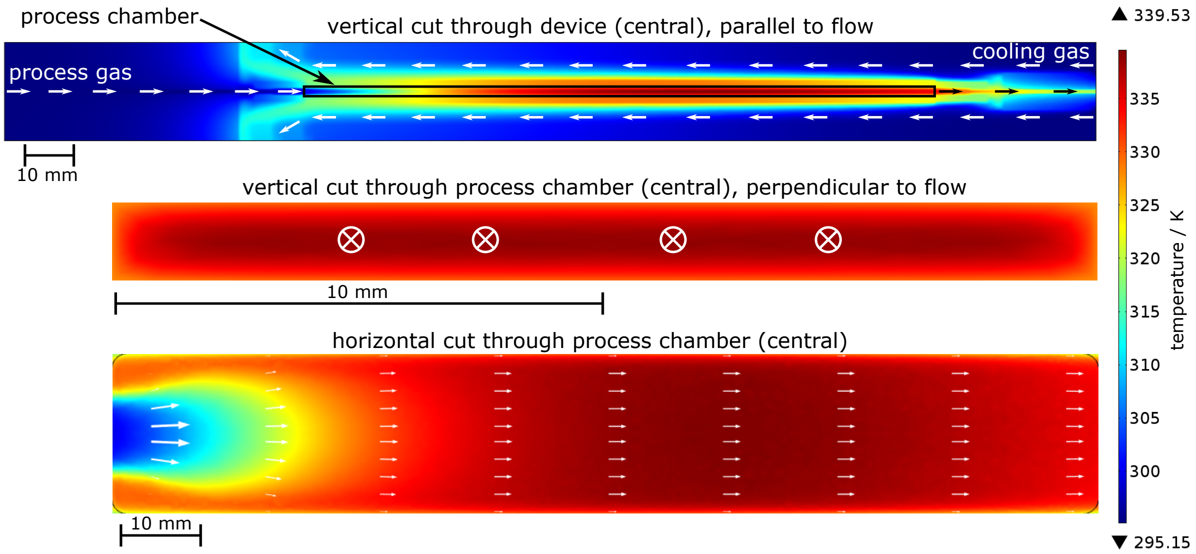

Figure 4.11.: Simulated temperature distribution after 2200 s at a pressure of 200 mbar. Taken with permission from [62], © IOP Publishing Ltd.

plate capacitors in series, what leads to a value of $C_\mathrm{d} = 20.2\,\mathrm{pF}$. Using this method, edge effects are not considered, and neither are technologically unavoidable influences of the manufacturing process. In addition to conventional production tolerances of the individual parts, the silicone sealant used to fix the electrodes on the dielectrics can affect the actual value in the pF range.

Therefore, the difference to the measurement-based approach used before to obtain $C_\mathrm{d} = 24.3\,\mathrm{pF}$ is plausible, where the latter value seems more credible. Alternatively, the method presented by Pipa *et al.* based on multiple Q(V)-plots [92] can be used. It seems to be useful because it allows to average out statistical deviations on the measurement of single Q(V)-plots. The results however are inconsistent, what most likely indicates that the discharge extinction voltage (u_g at the end of the active phase) is not constant over the external voltage amplitude. Using the more extensive equivalent circuit by Peeters and van den Sanden [87] could also potentially improve the quantitative reliability of the proposed method. A comparison of previously measured temperature values with results calculated from the same data using the more detailed equivalent circuit is depicted in figure 4.12. It shows that using the more extensive model does not substantially influence the obtained results in the investigated system.

4.4. Controlling the main operating parameters

Up to now, the $\overline{u_\mathrm{g}}$-based temperature measurement has only been applied to the VDBD while a gas flows through it. This allows comparing the results to the values generated using the thermistor, but does not cover all operating points necessary for an actual application in the VDBD. Instead, in the case that an NO_x-dominated chemistry is requested by the application, an intermediate release of O_3 during the heat-up might be

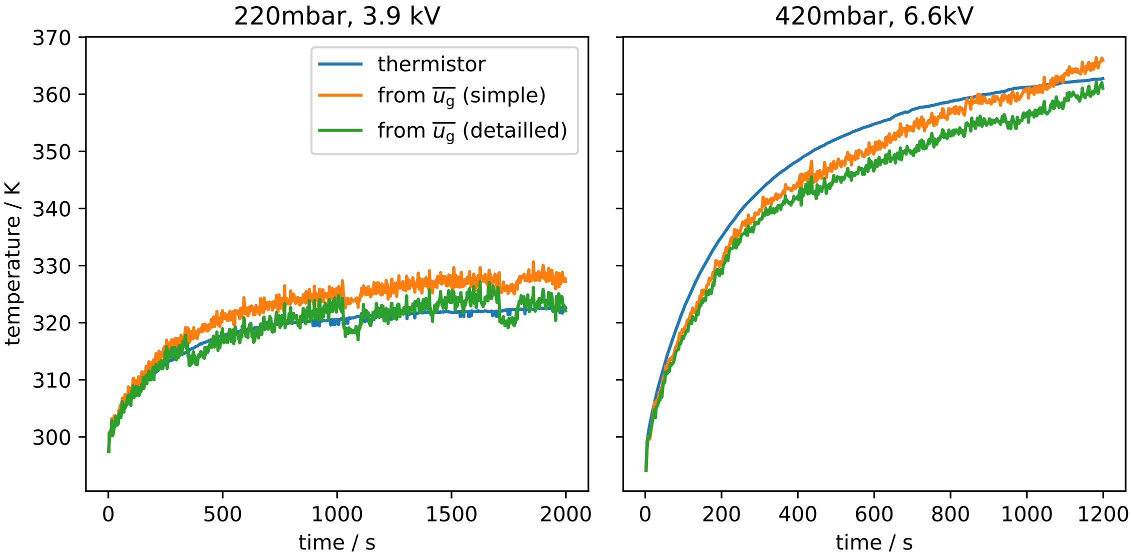

Figure 4.12.: Comparison of the previous approach to the more extensive equivalent circuit proposed by Peeters and van de Sanden.

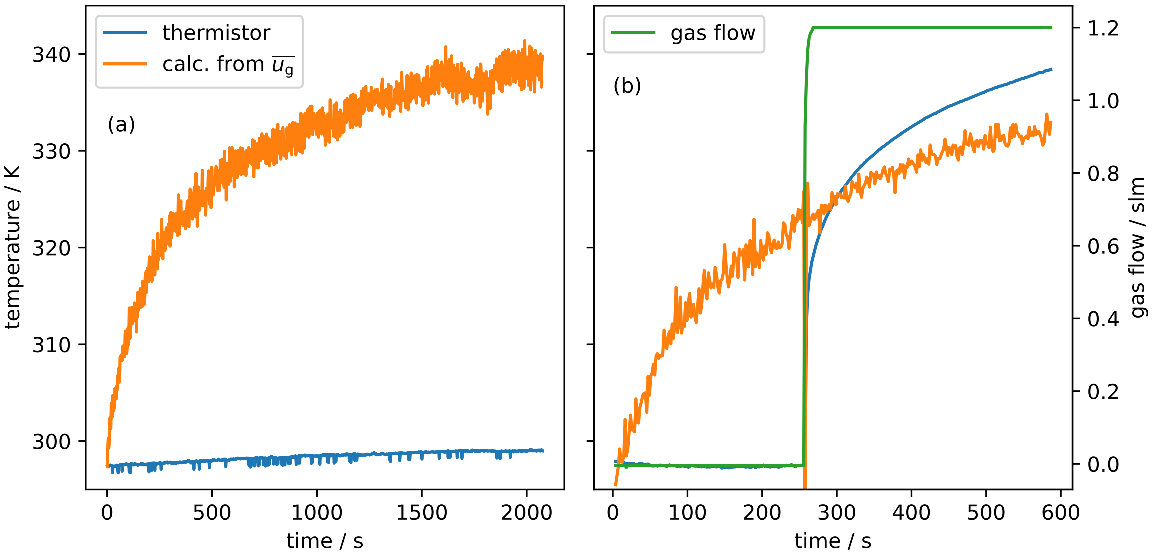

Figure 4.13.: (a) Comparison of temperature when calculated from $\overline{u_g}$ and measured with the thermistor without gas flow. (b) Complete process with heat-up phase without gas flow and usage with gas flow. Taken with permission from [62], © IOP Publishing Ltd.

undesirable. To prevent this, the heat-up could be performed without gas flow, however it is unlikely that the thermistor can deliver any expressive values in this case. Instead, the $\overline{u_\mathrm{g}}$-based temperature measurement could close this crucial information gap.

Operating the VDBD without gas flow basically requires only that the throttle valve at the process gas inlet is completely closed, however this leads to a pressure decrease and therefore reduces the power that can be dissipated for heating. A second throttle valve in the main gas supply overcomes this limitation by reducing the efficiency of the Venturi pump and therefore increasing the process gas pressure. The described setup has been used to measure the temperature without gas flow at a process gas pressure of 200 mbar and an external amplitude of 4.4 kV. Figure 4.13(a) shows the results calculated from $\overline{u_\mathrm{g}}$ and measured with the thermistor, whereas the latter does not detect the temperature increase. The $\overline{u_\mathrm{g}}$-based measurement in contrast delivers plausible results, however it operated using a higher calibration constant compared to the flow-enabled operation. For the present case, the value of $c_\mathrm{cal} = 17.5\,\mathrm{VKPa}^{-1}$ is 7 % higher than the usual values determined in course of the earlier investigations. Consequently, c_cal cannot necessarily be treated as a constant regarding the gas flow rate.

Proceeding from these findings, the method is now incrementally transferred to the envisaged application for temperature measurement in the VDBD. While a thermistor already fulfills this task during operation with gas flow, controlling the heat-up requires the new approach. Consequently, the first step for the transfer to application is the usage in a VDBD heat-up cycle. The latter starts with an operation without gas flow that cannot be monitored by the thermistor. As soon as the $\overline{u_\mathrm{g}}$-based temperature measurement detects that the pressure-specific O_3- to NO-transition temperature is reached, the gas flow is switched on.

In order to implement the described procedure, several enhancements to the basic measurement script are necessary. To take the significant difference of c_cal between the operation with and without flow into account, one calibration constant for each case is provided. This in turn implies that information suitable to programmatically chose c_cal needs to be available during operation. In the laboratory investigation, the flow rate has been measured using a MKS 1179B gas flow controller and then compared to a threshold value to chose the correct c_cal. In later applications, a lock valve with an electrical contact could fulfill a similar task. Another information to be processed is the pressure-dependent temperature that marks the transition from O_3 to NO production. The system needs to be equipped with a pressure sensor anyway, therefore the transition temperature at the present operating point can efficiently be calculated. The outcome could be used to operate a valve, however in the present implementation the operating mode (O_3 or NO) is only displayed. Figure 4.13(b) depicts the essential quantities during the complete procedure.

Compared to a simpler timing-based warm-up strategy, the presented system has the potential to achieve a better compromise between a short warm-up time and a convincing reliability. Pre-heated conditions when restarting the device can be taken into account as well as varying operating parameters. After reaching the desired temperature, the system can still be monitored and diagnosed.

5. Implementing the developed method in a prototype

All necessary basics for a device selectively producing O_3 or NO have been elaborated to this point. Crucial mechanisms have been understood and technological processes for an effective and efficient control have been developed. The latter rely on an oscilloscope operated at 1 GS/s, a type of device that is commercially available for a price of several hundreds or even thousands of Euros. This is not an issue for laboratory applications where suitable oscilloscopes are available anyway, but in laboratory applications a selective O_3 or NO production has already been established before [35, 54].

Distinct advantages of the new process compared to established ones can be expected in applications where neither laboratory equipment nor technical gases are available, thus preferably in an end-user device. This precludes using any type of oscilloscope, even low-performance models without a dedicated user interface are too expensive for an integration in a competitive device. Cost-effective alternative concepts are available [56].

Without an oscilloscope, the voltage and charge waveforms used to calculate the gas gap voltage u_{g} cannot be recorded synchronously. The signals can be synchronized afterwards assuming that the extrema occur at the same temporal positions for both signals. This is exemplarily depicted in figure 5.1(a). Figure 5.1(b) reveals that these points can be attributed to the active phases of the discharge process. At voltage and charge extrema, the discharge extincts, which is why the gas gap voltage value in this point will be called $u_{\mathrm{g,ext}}$ hereafter. In order to use $u_{\mathrm{g,ext}}$ as a basis for a temperature measurement rather than $\overline{u_{\mathrm{g}}}$, only the minima or maxima of voltage and charge need to be known, not the complete Q(V)-plot. This would avoid the necessity to use an analog-digital-converter (ADC) fast enough to resolve the waveforms in detail. Instead, the built-in ADC of an Arduino single-board microcontroller is sufficient. In real-time, it is only capable of providing about 10 kS/s, which equals less than one sample per period at 30 kHz. Despite the long time between two subsequent samples, it is possible to determine the signal value adequately exact at any time; it is however uncertain at which point of time. This is possible due to the working principle of the ADC using a very fast sample-and-hold circuit at the input - the long delay between subsequent samples is caused by other parts of the ADC when the value to sample has already been fixed. This results in the distribution of values measured by the ADC as shown in figure 5.2 for a signal proportional to the charge in the VDBD prototype. Values below the reference potential of 0 V are determined as 0 V, the maximum value is detected reliably. Therefore, the maximum charge can simply be measured over a capacitor and a voltage divider via the ADC by recording sufficient samples and using their maximum. The same concept could be used to determine the voltage maximum, however the good

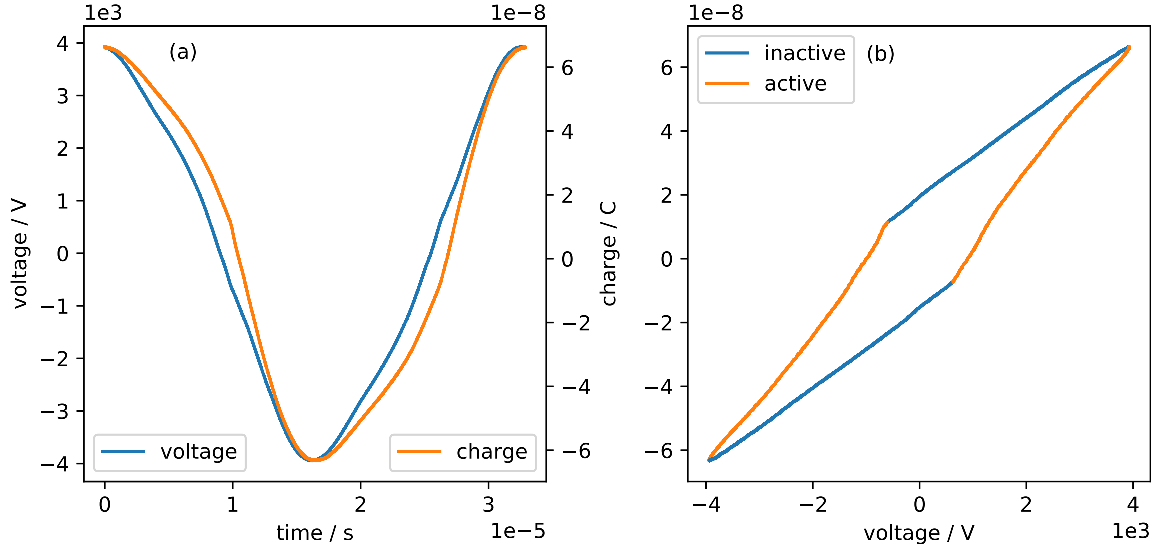

Figure 5.1.: (a) Temporal evolution of voltage and charge in an example measurement. (b) Resulting Q(V)-plot.

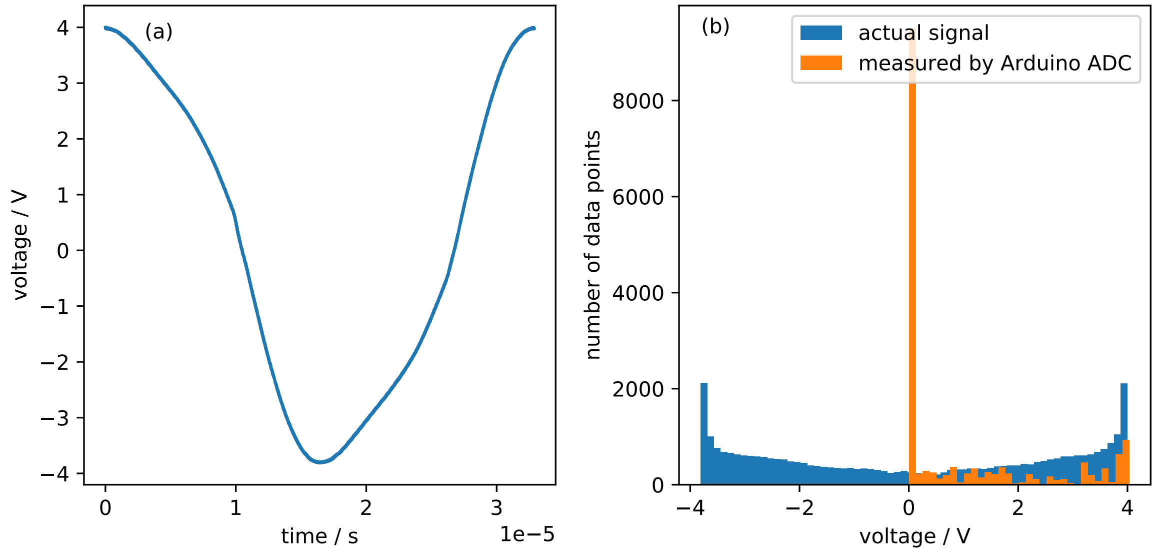

Figure 5.2.: (a) Exemplaric charge-proportional signal of the VDBD prototype scaled to a maximum of 4 V. (b) Histogram of the actual signal and its sampling by the Arduino ADC.

stability of the high-voltage generator allows deducing the voltage maximum from the input voltage as well. Consequently, a voltage divider at the high voltage source input can serve as a measurement facility for the Arduino ADC.

5.1. Adapting the measurement method

Instead of the capacitance C_{d}, a more general weighting factor w can be used to calculate a characteristic voltage

$$u_{\mathrm{char}} = V - \frac{Q}{w}. \tag{5.1}$$

To determine w, the variation of u_{char} over the voltage amplitude at constant temperature for different pressure levels is minimized using w as a parameter. This yields a value of $w = 3.04 \cdot 10^{-11}\,\mathrm{C/V}$. A temperature determination based on u_{char} works comparable to the procedure based on $\overline{u_{\mathrm{g}}}$ with $C_{\mathrm{d}} = 24.3\,\mathrm{pF}$.

This is exemplarily depicted in figure 5.3(a). The figure also shows the motivation for introducing w: Without any alteration, the measurement method presented in chapter 4 cannot be used to determine the gas temperature in the DBD based on $u_{\mathrm{g,ext}}$. Figure 5.3(b) outlines an idea why the results are implausible; $u_{\mathrm{g,ext}}$ is not only dependent on temperature and pressure when calculated using the previously determined value $C_{\mathrm{d}} = 24.3\,\mathrm{pF}$. Instead, an additional dependency on the external voltage amplitude can be observed. The voltage amplitude in the measurement shown in figure 5.3(a) does not vary by more than $0.2\,\%$, hence this does not directly explain why the temperature measurement does not deliver plausible results. However, it seems to indicate that additional dependencies influence $u_{\mathrm{g,ext}}$. Using w instead of C_{d} when working with u_{char} instead of $\overline{u_{\mathrm{g}}}$ overcomes this.

5.2. Implementation in a stand-alone prototype

Using a charge weighting factor $w = 3.04 \cdot 10^{-11}\,\mathrm{C/V}$, a temperature measurement based on u_{char} can provide results equivalent to the ones obtained from the method presented in section 4. With that, the primary challenge for a temperature determination based on electrical parameters using a microcontroller has been overcome, because u_{char} can be determined without a synchronized time-resolved measurement of two quantities. This motivates developing an Arduino-based measurement board to be integrated in a stand-alone prototype.

5.2.1. The measurement board

The measurement board has been developed around an Arduino Pro Mini single-board microcontroller. The latter is placed on a printed circuit board together with a NCV78M05 voltage regulator used to supply the operating voltage of 5 V to the microcontroller. This allows feeding the device from a DC voltage up to 35 V, while the voltage regulator integrated in the Arduino is specified for not more than 12 V. An adjustable LM350T

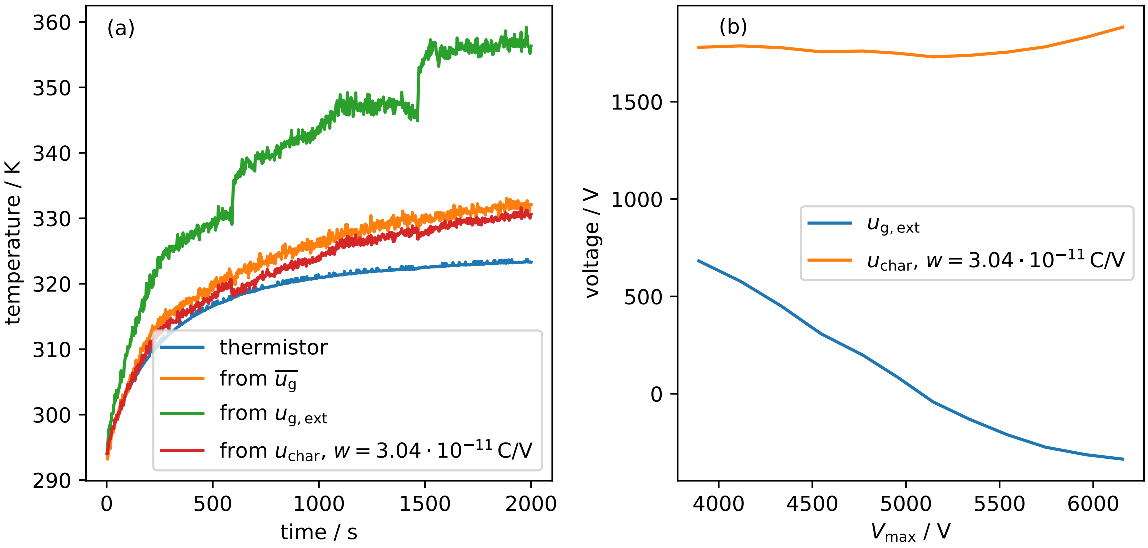

Figure 5.3.: (a) Temperature determined using a thermistor, the original method from chapter 4, the same method using $u_{g,ext}$ instead of $\overline{u_g}$ and using u_{char}. (b) Evolution of $u_{g,ext}$ and u_{char} over the external voltage amplitude.

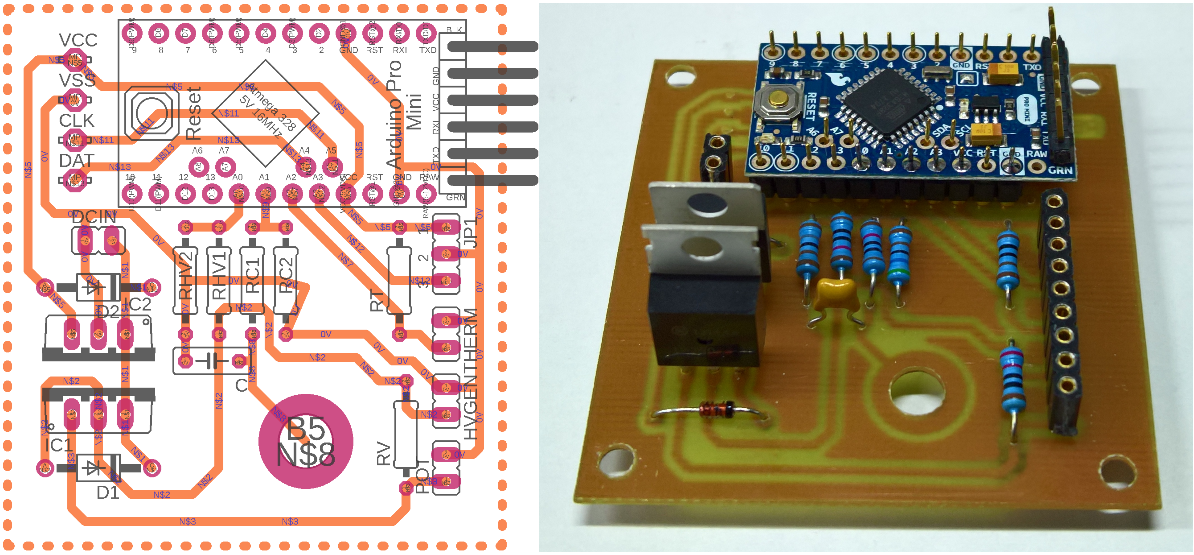

Figure 5.4.: Layout of the measurement board and actual device.

voltage regulator is used to power the high-voltage generator. To deduce the DBD operating voltage, the input voltage supplied to the high-voltage generator is measured over a resistive voltage divider using the Arduino ADC. For charge measurement, a 10 nF capacitor is built in and also connected to the Arduino via a voltage divider. Pin sockets allow connecting a DC power connector for a laptop power supply, the high-voltage-source, a potentiometer for the voltage regulation as well as the DBD ground electrode, a thermistor and a pressure sensor. The resulting circuit board is depicted in figure 5.4.

5.2.2. The complete assembly

As a basis to attach the VDBD prototype with a Venturi pump, the high voltage source and the measurement board, a base plate has been manufactured. It measures $(295 \times 178)\,\mathrm{mm}^2$ and is made of PMMA with a thickness of 10 mm. Side panels can be mounted using screws to form a housing around the system. A top plate is then mounted using a form-fit connection to the side plates made of interlocking tabs. Figure 5.5 shows the complete device.

Heatsinks mounted to the voltage regulators on the measurement board allow a continuous operation, and a LCD display connected via the I^2C-bus is used to output pressure, voltage and temperature values. A switch in the supply line of the high voltage generator can disable the high voltage generator independent of the measurement board. For setting the operating voltage, a rotary knob adjusting a $5\,\mathrm{k}\Omega$ potentiometer is provided. Tubes made of polytetrafluoroethylene (PTFE) with 6 mm outer diameter as well as 4 mm polyurethane (PUR) tubes are used to supply driving and cooling gas. Moreover, they make up the operating gas inlet. The latter requires a throttle valve and a lock valve that need to be connected externally. A button connected to a digital input of the measurement board microcontroller allows switching between different characteristic maps for different gas flow regimes. The system is combined with an external DC power supply (RS PRO JYH32) providing only 24 V to prevent overheating the voltage regulators in the non-ventilated housing during continuous operation.

5.3. Characterization

In order to allow an u_{char}-based temperature measurement, u_{char} needs to be measured reliably first. This is validated in two steps: First, the setup is calibrated to measure the external voltage amplitude and the charge amplitude correctly. On this basis, the temporal evolution of u_{char} is measured both with the measurement board and with a DPO4104 oscilloscope. In principle, the calibration step is optional. Instead, the correlation of the actual values and the “counts” measured by the Arduino ADC could also be calculated from the ADC characteristics, the voltage divider ratio on the measurement board and the characteristics of the high-voltage generator. An actual calibration is performed anyhow to provide an additional verification and to allow for tolerances in the components.

Figure 5.6 depicts the calibration results in comparison to the constructively expected

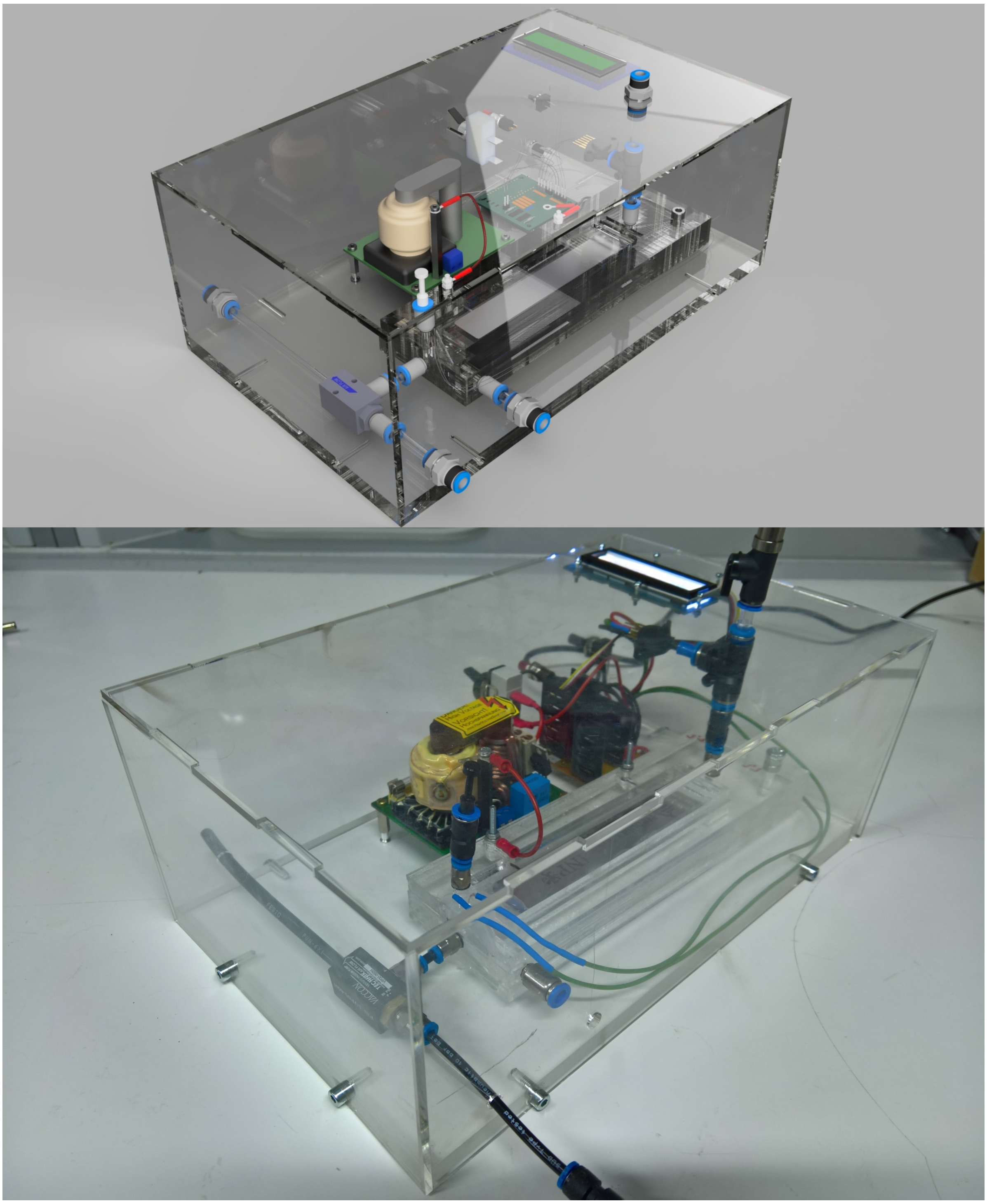

Figure 5.5.: Rendering of the complete prototype in comparison to the manufactured device in operation.

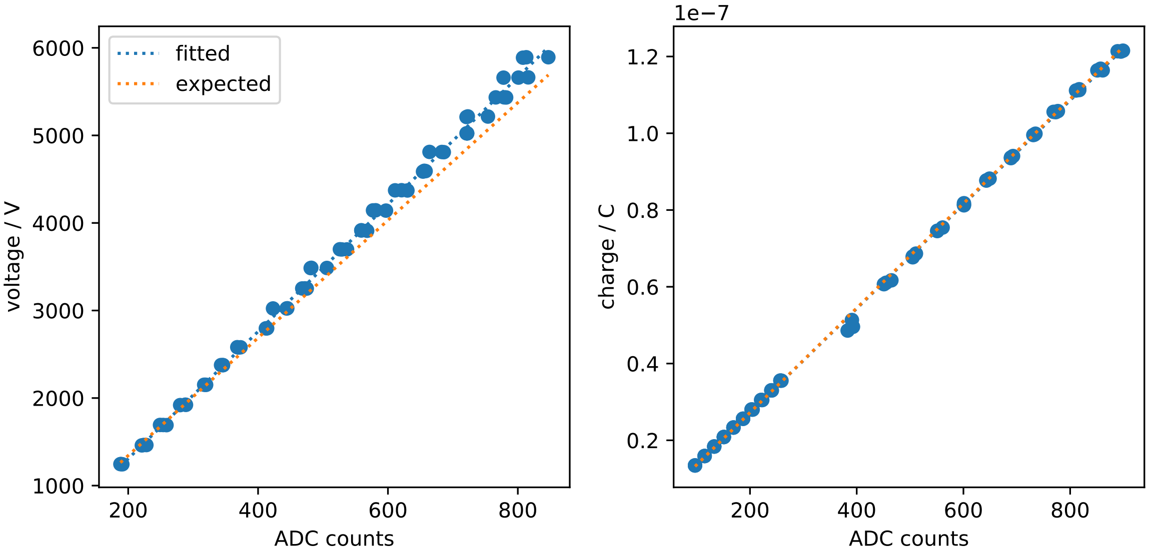

Figure 5.6.: Relation between voltage and charge amplitude measured by an oscilloscope and the ADC counts on the measurement board.

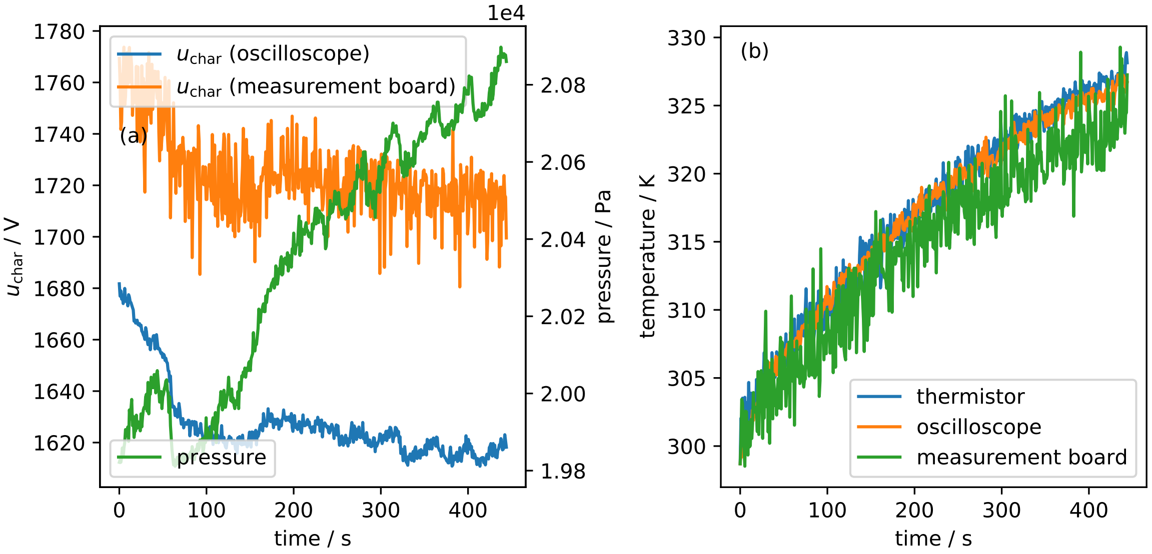

Figure 5.7.: (a) Temporal evolution of u_{char} measured by the oscilloscope and by the measurement board. (b) Resulting temperature evolution in comparison to the thermistor.

correlation. In each case, there is a linear connection between the number of counts in the ADC and the value to be measured. The charge amplitude is determined as expected, whereas the actual voltage amplitude is slightly higher. This can most likely be attributed to deviations of the high-voltage-generator characteristics from its nominal characteristic.

Using linear functions fitted to the measured data in figure 5.6 and a charge weighting factor of $3.04 \cdot 10^{-11}\,\mathrm{C/V}$, a test measurement yields the temporal evolution of u_{char} shown in figure 5.7(a). An offset compared to the value simultaneously obtained from the oscilloscope is apparent, however its influence on the actual temperature determination is acceptable. The temperature values depicted in figure 5.7(b) have been calculated using a calibration constant determined from the first measurement points obtained from the oscilloscope and the measurement board, respectively. In order to allow a convenient application of the device, this procedure needs to be replaced by an automatic choice of an appropriate temperature calibration factor depending on the operating conditions.

5.3.1. Initial operation and basic calibration

After the characterization of components and assembly of the complete setup, its crucial functionality has been tested. For this, the device has been connected to the FTIR setup described in section 3.2 and operated using the highest possible voltage and peak efficiency of the Venturi pump at a process gas pressure of 200 mbar. All parameters accessible to the measurement board have been read out using the universal asynchronous receiver-transmitter (UART) interface of the Arduino. It was found that even at a thermistor-measured temperature of 368 K, no NO could be produced. Consequently, the system misses a key feature when operated under the described conditions. A further temperature increase was avoided to protect the PMMA-made DBD housing.

The reason for the absence of NO despite high temperature and low pressure was found to be an inappropriately high process gas flow rate. According to the simulations described in section 3.3, the flow rate can influence the temperature necessary for a transition from O_3 to NO production. Restricting the Venturi pump performance to provide a pressure-flow rate characteristic comparable to the one used for the investigations from chapter 3 solved the problem. This involves a flow rate of 150 sccm at 200 mbar, and allows a NO production after almost 10 minutes. The noticeably long time needed to reach the NO mode could potentially be decreased by using a higher DC input voltage.

As it might not be desirable to heat the device up with activated gas flow and hence accompanied with a release of O_3, temperature monitoring without gas flow is the main task to be accomplished by the measurement board. In accordance with the results from the investigation of the measurement board outside the assembly, with rising temperature, the characteristic voltage $u_{\mathrm{char}} = V - Q/w$ decreases. Interestingly, this is solely caused by an increase of Q, while V remains constant. As a consequence, the simplest and most straightforward implementation of a temperature monitoring is to measure the charge and calculate the difference from the desired value. The latter is easily to be determined by bringing the device in NO mode, switching the flow off and measuring the charge. It has been found that at a pressure around 200 mbar, the charge corresponding

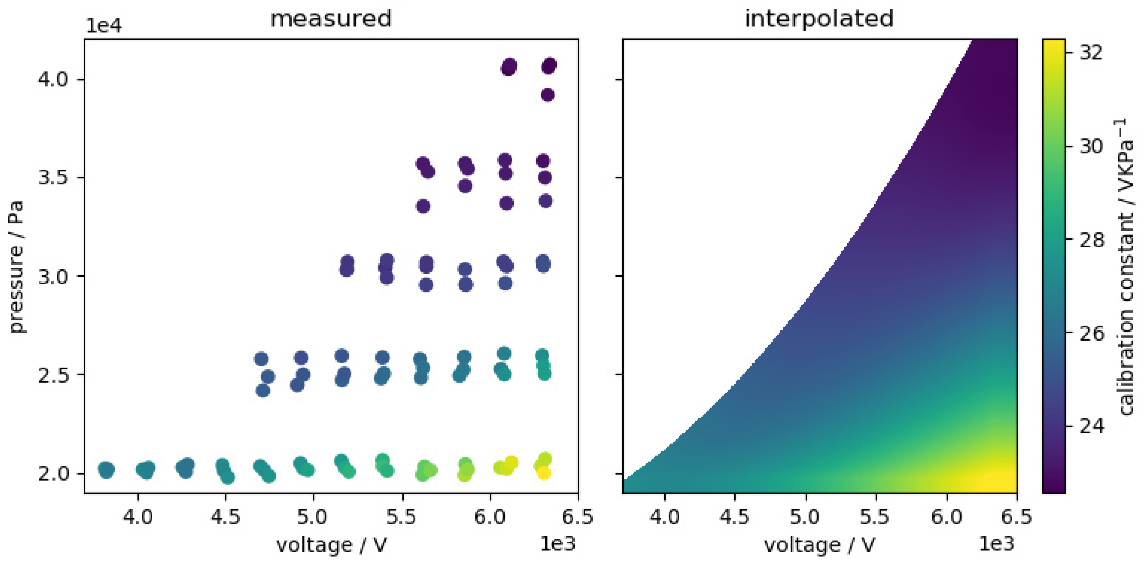

Figure 5.8.: Characteristic map of the calibration constant over voltage amplitude and pressure.

with a transition from O_3 to NO production is about 100 counts of the ADC above the value at room temperature. The conversion to an actual value of charge can be omitted in this case, but a pressure dependency of the "counted" value is taken into account to allow for fluctuations caused by the Venturi pump.

The difference of the ADC counter value to the one at room temperature is displayed to allow controlling the heat-up progress. After the desired value of 100 above the room-temperature value has been measured for at least ten times in a row, the display changes its background color to indicate readiness for switching on the flow. After this is confirmed by the user by pressing a button on the device, the display is used to show a temperature value rather that the heat-up progress. For calculating the temperature, actual voltage and charge values are calculated from the ADC output. Then, the temperature is calculated from u_{char}. In this process, the necessary calibration constant is calculated from a characteristic curve that is hard-coded in the control software based on a measurement at room temperature.

5.3.2. Advanced temperature calibration

Based on the calibration procedure described up to this point, the prototype can be controlled satisfactorily in the narrow parameter range determined by the power supply. For effectively using higher pressure values or reducing the warm-up time, a more sophisticated calibration is necessary. Although the measurement method to be implemented relies on a static connection between pressure p, characteristic voltage u_{char} and temperature T for small changes of said quantities, this connection does not necessarily persist also for larger variations of one or more parameters.

Therefore, dependencies of the calibration constant c_{cal} at least from voltage amplitude and pressure need to be taken into account. For this, c_{cal} has been measured near room temperature for a multitude of parameter combinations. In order to allow an interpolation between the measurement points, a surface defined by basis splines (B-splines) has been fitted to the data. Figure 5.8 shows one set of measured values and the fitted characteristic map. It corresponds to the operation of the Venturi pump at its peak efficiency and a pressure regulation via the input throttle valve. Another map reflecting the operation with a closed inlet valve and a pressure regulation using the pump performance has been implemented as well. This allows choosing the correct calibration for each operating mode.

6. Conclusion and outlook

In this work, a new plasma source concept has been developed, investigated and implemented that can be controlled to switch between an ozone (O_3) and a nitric oxide (NO) production from ambient air during operation. The practical use of CAP in medicine resulted in deeper knowledge regarding the role of RONS. To control the relation between ROS and RNS within one device opens up new options for individual medicine.

As constructive realization, a dielectric barrier discharge (DBD) coupled to a Venturi pump has been chosen. The device is called Venturi DBD (VDBD) and it has been used to enhance the knowledge about air plasma chemistry at intermediate pressure. Among the operating parameters of the device, gas temperature and pressure were identified as the key quantities to influence the balance of O_3 and nitrogen oxides. At lower temperatures, O_3 is produced primarily, while NO is generated at higher temperatures. At intermediate temperature values, nitrogen dioxide (NO_2) is most abundant. The respective temperature necessary to switch from an O_3-containing to a nitrogen-oxides-only output chemistry can be influenced by the operating pressure and ranges from 327 K at 200 mbar to 398 K at 400 mbar. A zero-dimensional reaction kinetics model outlines the most important reaction mechanisms for the observed process. Moreover, it reveals that the constructively given coupling of gas pressure and flow rate additionally promotes the controllability of the output chemistry.

A practical application of the system requires an economic and robust means for process control and gas temperature determination. The system developed for this purpose uses electrical quantities of the discharge to realize a process control mechanism. For the first time, the temperature could be successfully measured with reasonable precision from the voltage drop over the discharge. Although the measurement is based on a very simple hypothesis derived from the ignition voltage in a previously non-ionized gas, the method has proven to be reliable under the prevailing conditions. It relies on a calibration at room temperature and does not need any optical or mechanical access to the process chamber, but provides no spatial resolution. In contrast to a temperature measurement using a thermistor in the outlet channel, it works both with and without gas flow. The temperature measurement could potentially be used as the basis for the improvement of related DBD-based constructions. To facilitate the understanding of its physical background, a hydrodynamic model coupled to Poisson's equation and a plasma chemical reaction model can be set up and investigated for the factors influencing the connection between gas temperature and voltage drop.

The system together with the developed process control mechanism was successfully transferred into an easy-to-use, cost efficient prototype. The device is based on an Arduino microcontroller extended by a simple self-made circuit board. It can be used with different calibration setups and is operated and controlled autonomously except for a power outlet and a pressurized air supply. Many of its parts are manufactured using a laser cutter what allows an efficient implementation of constructive changes and an economic production of different versions. The prototype is completely enclosed, therefore its usage does not require any experience in handling high-voltage systems.

The new device is, in addition to its purpose for basic investigations, intended to be extendable for more complicated operating conditions. In particular, an additional humidification of the process gas could be fit subsequently. The reduced pressure would promote the vaporization of water and therefore contribute to a steady humidification without excessive drop formation at surfaces. The necessary constructive changes would be manageable and easier to accomplish compared to alternative concepts. Still, a substantially more complicated plasma chemistry would increase the effort necessary for investigations, but allow a controlled production of water-based species such as hydroxyl (OH) and hydroperoxyl (HO_2) radicals, hydrogen peroxide (H_2O_2) and peroxynitrous acid (ONOOH). Therefore, disinfection and wound healing application could benefit from the extension.

Moreover, subsequent versions of the device can be combined with more extensive real-time diagnostics targeting electrical, fluid-mechanical and thermal parameters. As part of a complete system, this provides control of the produced species composition coupled to medical imaging for an optimized and individualized treatment process. Consequently, the presented techniques represent a starting point for the development of system solutions realizing personalized medical applications based on CAP.

A. The computational fluid dynamics simulation in detail

A vast number of physical phenomena can be computationally modeled by solving a system of differential equations on the desired domain using appropriate boundary conditions. Usually, the actual problem has to be simplified to obtain a manageable complexity of the computational task. Errors and inaccuracies can emerge in the case of improper simplifications, but also if the domain is unfavorably discretized or if iterative computational procedures do not converge. Therefore, this chapter outlines the considerations regarding the mentioned aspects that lead to the computational fluid dynamics (CFD) model used in section 4.1.

CFD simulations are a common tool in many different fields of application and are implemented in a variety of free and commercial software packages. These differ in basic aspects, starting with the numerical method to solve the equation system. The most commonly used numerical method for CFD simulations is the finite volume method (FVM) that is implemented by software such as ANSYS® FLUENT® and OpenFOAM® [113]. For the present application, COMSOL Multiphysics® was available as a versatile and performant simulation tool based on the finite element method (FEM).

A.1. Notes on the finite element method (FEM)

Using FEM, the solution to a system of differential equations can be reliably approximated even on domains with complex geometrical features. To achieve this, the domain Ω is divided into smaller, non-overlapping subdomains with simple shapes such as tetrahedra. These are called *cells* or *elements*, and the element corners are called *nodes*. On each of the subdomains, the field to be solved for is expressed as a low-order polynomial, the so-called basis function. Consequently, the calculated result does not solve the equations and boundary conditions pointwise. Instead, only the weighted average of the residual is set zero. In general, an equation

$$\tilde{L}\left[f\left(\vec{r}\right)\right] = s\left(\vec{r}\right) \tag{A.1}$$

with an operator $\tilde{L}$, a function f depending on the location $\vec{r}$ and a source s is to be solved for $f(\vec{r})$ on Ω. First, f is approximated by a discrete number $\tilde{N}$ of basis functions φ_i with individual coefficients f_i that are to be calculated, i.e.

$$f(\vec{r}) \approx \sum_{i=1}^{\tilde{N}} f_i \varphi_i(\vec{r}). \tag{A.2}$$

The residuals

$$\tilde{r} = \tilde{L}\left[f\left(\vec{r}\right)\right] - s\left(\vec{r}\right) \qquad \text{(A.3)}$$

are now calculated and weighted using $\tilde{N}$ weighting functions or test functions w_i. It is possible to use $w_i = \varphi_i$, what is then called Galerkin's method of weighted residuals. The weighted residuals are now set to zero. Consequently, to approximate equation A.1 using FEM, the equations

$$\langle w_i, \tilde{r} \rangle = \int_\Omega w_i \tilde{r} \mathrm{d}\Omega = 0,\ i = 1, 2, ..., \tilde{N}, \qquad \text{(A.4)}$$

called the weak form of equation A.1, need to be solved for f_i [114]. A simple example, also closely following [114], shows an application of the FEM in more detail. It is based on the one-dimensional Helmholtz equation

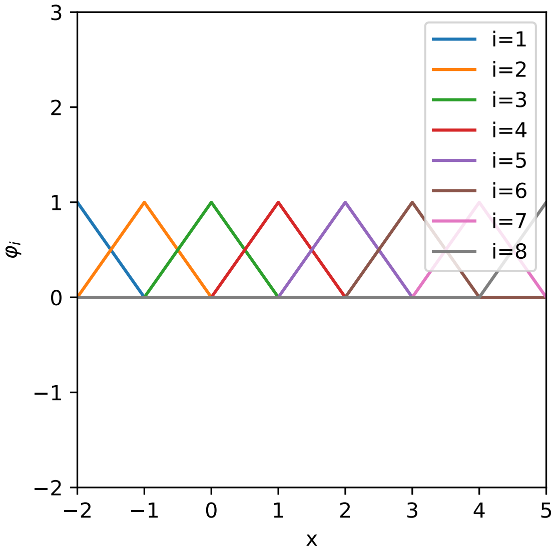

Figure A.1.: Triangular nodal basis functions.

$$-\frac{\mathrm{d}}{\mathrm{d}x}\left(\alpha_\mathrm{m}\frac{\mathrm{d}f}{\mathrm{d}x}\right) + \beta_\mathrm{m} f = s,\ x_\mathrm{a} < x < x_\mathrm{b} \qquad \text{(A.5)}$$

that is used to model electromagnetic waves, among other applications. The boundary conditions $f(x_\mathrm{a})$ and $f(x_\mathrm{b})$ are known as well as the material properties α_m and β_m and the source term s. FEM is now to be used to determine the function $f = f(x)$ on the interval $x_\mathrm{a} < x < x_\mathrm{b}$. The domain, assumed between $x_\mathrm{a} = -2$ and $x_\mathrm{b} = 5$, is divided into 7 equally large elements. Consequently, there are 8 nodes that can be numbered $i = 1, 2, ..., 8$ and given the coordinates $x_i = i - 3$. For each node, a basis function

$$\varphi_i(x) = \begin{cases} 1 - |x - x_i|\,; & |x - x_i| < 1 \\ 0; & \text{otherwise} \end{cases} \qquad \text{(A.6)}$$

as shown in figure A.1 is used. It is apparent that the functions are linear in each interval. The basis functions are now used to approximate the function to be calculated with appropriate coefficients, i.e.

$$f(x) = \sum_{j=1}^{8} f_j \varphi_j(x). \qquad \text{(A.7)}$$

Since the nodal basis function are 1 on the respective nodes, the coefficients represent the values of f at the nodes. From the boundary conditions, $f_1 = f(x_\mathrm{a})$ and $f_8 = f(x_\mathrm{b})$ are known. Using Galerkin's method and hence $w_i(x) = \varphi_i(x)$, the remaining coefficients for $i = 2, 3, ..., 7$ can be calculated. For this, weak form of equation A.5 is determined. This starts with multiplying the residual with w_i, yielding

$$\tilde{r} \cdot w_i = -\alpha_\mathrm{m} w_i f'' + \beta_\mathrm{m} w_i f - w_i s. \qquad \text{(A.8)}$$

Integrating over x from x_a to x_b using integration by parts leads to the weak form that is set to zero:

$$\underbrace{\left[\alpha_\mathrm{m} f' w\right]_{x_\mathrm{a}}^{x_\mathrm{b}}}_{0} + \int_{x_\mathrm{a}}^{x_\mathrm{b}} \left(\alpha_\mathrm{m} w_i' f' + \beta_\mathrm{m} w_i f - w_i s\right) \mathrm{d}x = 0 \tag{A.9}$$

Here, equation A.7 is inserted what, after rearranging, leads to a set of equations in the form

$$\underbrace{\int_{x_\mathrm{a}}^{x_\mathrm{b}} \Big(\alpha_\mathrm{m} \varphi_i' \varphi_j' + \beta_\mathrm{m} \varphi_i \varphi_j\Big) \mathrm{d}x}_{A_{ij}} \cdot \underbrace{f_j}_{z_j} = \underbrace{\int_{x_\mathrm{a}}^{x_\mathrm{b}} \varphi_i s \mathrm{d}x}_{b_i}. \tag{A.10}$$

With $i = 2, 3, ...7$ equations and $j = 1, 2, ..., 8$ coefficients, a matrix $\mathbf{A}$ with 8 columns and 6 rows can be formed from A_{ij}. Because f_1 and f_8 are given by the boundaries, they can be moved to the right side of the equation what yields

$$\begin{pmatrix} A_{22} & A_{23} & \cdots & A_{27} \\ A_{32} & A_{33} & \cdots & A_{37} \\ \vdots & \vdots & \ddots & \vdots \\ A_{72} & A_{73} & \cdots & A_{77} \end{pmatrix} \begin{bmatrix} f_2 \\ f_3 \\ \vdots \\ f_7 \end{bmatrix} = \begin{bmatrix} b_2 \\ b_3 \\ \vdots \\ b_7 \end{bmatrix} - \begin{bmatrix} A_{21} f_1 + A_{28} f_8 \\ A_{31} f_1 + A_{38} f_8 \\ \vdots \\ A_{71} f_1 + A_{78} f_8 \end{bmatrix}. \tag{A.11}$$

Now, $\mathbf{A}$ containing the unknowns is square, i.e. there are as many unknowns as equations.

In the presented example, the boundary conditions $f(x_\mathrm{a})$ and $f(x_\mathrm{b})$ directly specify the value of the sought function at the boundaries and are called *Dirichlet* boundary conditions. If the derivative of the function is given instead, the condition is called *Neumann* boundary condition. A linear combination of both is referred to as *Robin* boundary condition. The case of vanishing function values (Dirichlet) and/or derivatives (Robin/Neumann) at the boundary is known as homogeneous boundary condition.

In the CFD model to be developed for section 4.1, a much more extensive system of equations needs to be solved. Nevertheless, substantial simplifications are unavoidable to limit the computational effort. Hereafter, the considerations that led to the equation system and boundary conditions in use are shown. These will result in a system description as simple as possible that still can cope with the problem to be solved.

A.2. The Reynolds Number

The Reynolds number is the most important parameter in fluid mechanics. It quantifies the ratio of inertial forces to tenacity forces and is defined as

$$\mathrm{Re} = \frac{UL\rho}{\eta} \tag{A.12}$$

[110]. The mass density ρ in the above equation can be estimated based on the density under normal conditions and a pressure of 0.2 atm as $1.293\,\mathrm{kg/m^3} \cdot 0.2 = 0.2586\,\mathrm{kg/m^3}$.

For the velocity U, the mean value at the narrowest cross section is considered. As the geometrical model is built using simplified gas channels for in- and outlet, the narrowest cross section can be found in the outlet with $A_\mathrm{c} = 2 \cdot 10^{-6}\,\mathrm{m}^2$. The measured mass flow through the device is $Q \cdot p = 1.08 \cdot 10^{-2}\,\mathrm{mbar} \cdot \mathrm{m}^3/\mathrm{s}$. Therefore, at a pressure of $p = 200\,\mathrm{mbar}$, the flow rate is $Q = 5.4 \cdot 10^{-5}\,\mathrm{m}^3/\mathrm{s}$. Considering the cross section, this leads to a mean flow velocity of $Q/A_\mathrm{c} = 27\,\mathrm{m/s}$.

As the characteristic length L, the diagonal of the cross section $2.24 \cdot 10^{-3}\,\mathrm{m}$ is used. The dynamic viscosity η of air is considered as $1.71 \cdot 10^{-5}\,\mathrm{Pa} \cdot \mathrm{s}$. Finally, the Reynolds number can be calculated as

$$\mathrm{Re} = \frac{0.2586\,\frac{\mathrm{kg}}{\mathrm{m}^3} \cdot 27\,\frac{\mathrm{m}}{\mathrm{s}} \cdot 2.24 \cdot 10^{-3}\,\mathrm{m}}{1.71 \cdot 10^{-5}\,\mathrm{Pa} \cdot \mathrm{s}} = 913. \tag{A.13}$$

Consequently, the value is low enough to avoid considering sub-grid turbulences: A transition from a laminar to a turbulent flow is often expected under technically relevant conditions around a critical Reynolds number $\mathrm{Re}_\mathrm{krit}$=2300. This number was determined experimentally [115] and must be treated as a guidance value only. The reason is that the setup-specific flow profile at the inlet strongly influences the transition to a turbulent flow. However, Reynolds numbers below 2000 imply a laminar flow even when the inlet flow is strongly perturbed [110]. Therefore, the model uses the Navier-Stokes equation without an additional consideration of turbulences.

A.3. The mathematical model

The mathematical description of a fluid dynamics system is based on the conservation of mass, momentum and energy, hence three formally similar equations need to be taken into account. Hereafter, they are briefly introduced, closely following [113].

The conservation of mass is expressed by the continuity equation

$$\frac{\partial \rho}{\partial t} + \nabla \cdot (\rho \vec{u}) = 0 \tag{A.14}$$

using mass density ρ, time t and flow velocity $\vec{u}$. The conservation of momentum is

$$\frac{\partial}{\partial t}(\rho \vec{u}) + \nabla \cdot (\rho \vec{u}\vec{u}) = \nabla \cdot \tau - \nabla p + \rho \vec{g} \tag{A.15}$$

with shear stress tensor τ, pressure p and gravity $\vec{g}$. The third equation is the conservation of energy

$$\frac{\partial}{\partial t}(\rho H) + \nabla \cdot (\rho \vec{u} H) = -\nabla \cdot \vec{q} + \frac{\partial p}{\partial t} + \nabla \cdot (\tau \cdot \vec{u}) \tag{A.16}$$

containing enthalpy H and heat flux $\vec{q}$.

This leads to a system of three equations with six unknowns, consequently additional correlations need to be taken into account. These are the thermal and caloric equations of state

$$p = \rho R T \tag{A.17}$$

with the gas constant R and temperature T and

$$\mathrm{d}H = c_\mathrm{p} \mathrm{d}T \tag{A.18}$$

using the specific heat capacity at constant pressure c_p. Furthermore, Fourier's law

$$\vec{q} = -\tilde{k}\nabla T \tag{A.19}$$

with the heat conductivity $\tilde{k}$ is taken into account. In a Newtonian fluid, the shear stress is

$$\tau = \eta \left(2\mathbf{S} - \frac{2}{3}\left(\nabla \cdot \vec{u}\right)\tilde{\delta}\right) \tag{A.20}$$

containing the dynamic viscosity η, the velocity gradient tensor $\mathbf{S}$ and the Kronecker tensor $\tilde{\delta}$ with

$$\mathbf{S} = \frac{1}{2}\left(\nabla\vec{u} + \left(\nabla\vec{u}\right)^\mathrm{T}\right) \tag{A.21}$$

and

$$\tilde{\delta}_{ij} = \begin{cases} 1 & (i = j) \\ 0 & (i \neq j) \end{cases} . \tag{A.22}$$

The above equations can be compiled into

$$\frac{\partial \rho}{\partial t} + \nabla \cdot \left(\rho\vec{u}\right) = 0 \tag{A.23}$$

$$\frac{\partial}{\partial t}\left(\rho\vec{u}\right) + \nabla \cdot \left(\rho\vec{u}\vec{u}\right) = -\nabla p + \nabla \cdot \left(\eta\left(2\mathbf{S} - \frac{2}{3}\left(\nabla \cdot \vec{u}\right)\delta\right)\right) + \rho\vec{g} \tag{A.24}$$

$$\begin{aligned} c_\mathrm{p}\left(\frac{\partial}{\partial t}\left(\rho T\right) + \nabla \cdot \left(\rho\vec{u}T\right)\right) = \\ \nabla \cdot \left(\tilde{k}\nabla T\right) + \frac{\partial p}{\partial t} + \nabla \cdot \left(\eta\left(2\mathbf{S} - \frac{2}{3}\left(\nabla \cdot \vec{u}\right)\delta\right) \cdot \vec{u}\right) . \end{aligned} \tag{A.25}$$

In COMSOL Multiphysics®, the Conjugate Heat Transfer model in the CFD module is designated to solve this equation set [111]. By default, the gravity $\rho\vec{g}$ is not taken into account, however it can be explicitly added as an external body force. For the present investigation, it has been neglected. Moreover, the energy conservation from equation $A.25$ is simplified by default to neglect pressure work and viscous heating. This default setting was also used for the simulations discussed in the present thesis.

A.4. Calculations for the convective cooling

At the bottom and top boundaries of the domain, the heat flux in normal direction equals the temperature difference to the environment times a heat transfer coefficient, i.e.

$$-\vec{n} \cdot \left(-\tilde{k}\nabla T\right) = \tilde{h} \cdot \left(T_\mathrm{ext} - T\right) \tag{A.26}$$

with the normal vector $\vec{n}$, the heat transfer coefficient $\tilde{h}$ and the ambient temperature T_ext [111]. Thus, the cooling by natural convection is taken into account. The heat transfer coefficient is calculated as

$$\tilde{h} = \frac{k}{L} \cdot \mathrm{Nu}_\mathrm{L} \tag{A.27}$$

[111,116] from the characteristic length L and the Nusselt number $\mathrm{Nu_L}$. The calculation of the Nusselt number used by COMSOL Multiphysics® [111] is in agreement with [116]. On the top plane for $T > T_{\mathrm{ext}}$ and on the bottom plane for $T \leq T_{\mathrm{ext}}$, it is

$$\mathrm{Nu_L} = \begin{cases} 0.54 \mathrm{Ra_L}^{1/4} & \mathrm{Ra_L} \leq 10^7 \\ 0.15 \mathrm{Ra_L}^{1/3} & \mathrm{Ra_L} > 10^7 \end{cases} . \tag{A.28}$$

For the case $T \leq T_{\mathrm{ext}}$ at the top plate and $T > T_{\mathrm{ext}}$ at the bottom plate, it is instead

$$\mathrm{Nu_L} = 0.27 \mathrm{Ra_L}^{1/4}. \tag{A.29}$$

In both cases, the Nusselt number is a function of the Raleigh number $\mathrm{Ra_L}$:

$$\mathrm{Ra_L} = \frac{g \left| \left. \frac{\partial \rho}{\partial T} \right|_p \right| \rho c_{\mathrm{p}} \left| T - T_{\mathrm{ext}} \right| L^3}{k \eta}. \tag{A.30}$$

Here, g is the gravitational acceleration and $|\partial\rho/\partial T|_p|$ the thermal expansion (called β in [116]). According to [111, 116], L is approximated as the ratio between area a and perimeter f of the plate, hence it is

$$L = \frac{a}{f} = \frac{(0.212 \cdot 0.032)\,\mathrm{m}^2}{(2 \cdot (0.212 + 0.032)\,\mathrm{m})} = 0.014\,\mathrm{m}. \tag{A.31}$$

Because top and bottom side contribute differently to the convective cooling, they correspond to different Nusselt numbers. This prevents introducing an additional horizontal symmetry plane what geometrically would be justified. The fact that the device is placed on a foamed plastic pad and therefore not cooled by free convection uniformly in the experiment is neglected. The convective cooling at the vertical sides is also taken into account. Here, the wall height of 0.019 m is the crucial geometrical parameter.

B. Breakdown processes in DBDs

The process of transforming a nonconducting material into a conducting state as the result of applying a sufficiently strong electric field is called breakdown. If the external field persists, a discharge will occur afterwards. The aim here is to calculate the voltage necessary to establish a self-sustaining discharge. This means that charged particles are not only transported in the form of a current, but are also generated in an extent that at least preserves their number. Thus, the term "breakdown" is specified here as the onset of a self-sustaining discharge. Description and characterization of gas breakdown processes is a very demanding task. The description here should only provide an overview on the basic physical relations. The first thing to mention in this context is that there is not *the* breakdown process. Instead, different mechanisms need to be distinguished. Important for DBD are the Townsend breakdown and the streamer breakdown. Their appearance depends on the operating conditions. Other phenomena like the leader breakdown and corona discharges are physically related, but not covered here.

B.1. Townsend breakdown

The theory on which the breakdown mechanism explained in this section is based on was developed by Townsend beginning around the year 1900. To characterize a Townsend breakdown, named after the British physicist, it is sensible to start considering an electron avalanche. The latter begins with a few electrons appearing for any reason, most likely due to cosmic rays. After applying an outer electric field, the electrons gain kinetic energy that can be transmitted to an atom or molecule during a collision. If that energy is higher than the ionization energy of the respective atom or molecule, the latter will be ionized. Thus, an ion, a new electron and the initial electron will be present. Both electrons are accelerated by the electric field again and, as a consequence, will ionize more atoms or molecules. As this mechanism proceeds, it develops like an avalanche which - in case of a constant electric field - moves in a determined direction. To generate an electron avalanche, an oscillating field can be used as well. For both cases, the generation of electrons in principle works as described. Essential differences arise from the fact that the avalanche is drifting uniformly in a constant field, whereas it is a more local phenomenon in an oscillating field. Obviously, the difference is more pronounced if the oscillating field changes its direction with a higher frequency.

The ionization of atoms and molecules is accompanied by several competing processes. The most notable examples are the excitation of electron states, molecular vibration and rotation. Moreover, there are elastic collisions, i.e. collisions without any "side effects". In electronegative gases, an attachment of electrons to atoms or molecules is important.

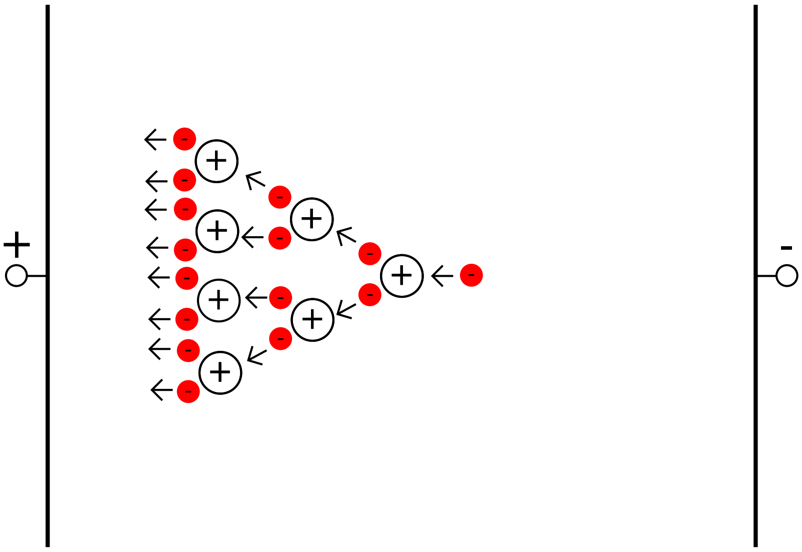

Figure B.1.: Formation of an electron avalanche, based on [117].

In contrast, recombination of ions and electrons does not affect the field strength necessary for breakdown distinctly. This is due to the proportionality of recombination rate to the square of electron density. Thus, attachment as a process scaling linearly with the electron density is more important at low electron densities. Instead, recombination becomes crucial when the gas is already ionized to a substantial extent. Then it limits further ionization.

The electron avalanche

The factor describing the change in the number of electrons $\tilde{N}$ on a path $\mathrm{d}x$ in an electron avalanche is called Townsend's coefficient for ionization α. As a consequence, the approach to describe the avalanche is

$$\mathrm{d}\tilde{N} = \tilde{N} \cdot \alpha \cdot \mathrm{d}x. \tag{B.1}$$

Integrating the equation and exponentiating e with it creates the expression

$$\tilde{N} = \tilde{N}_0 \cdot \exp\left(\int_{x_\mathrm{a}}^{x_\mathrm{b}} \alpha \cdot \mathrm{d}x\right), \tag{B.2}$$

if the process occurs between one electrode at $x = x_\mathrm{a}$ and the other one at $x = x_\mathrm{b}$. Clearly the most convenient case to use equation B.2 is to consider a Townsend's coefficient that is independent from x between two electrodes with the distance d, located at $x_\mathrm{a} = 0$ and $x_\mathrm{b} = d$. Then, it can be simplified to $\tilde{N} = \tilde{N}_0 \cdot \exp(\alpha \cdot d)$. This situation is shown in figure B.1 for $\tilde{N}_0 = 1$ and $\alpha = 1/\text{length unit}$. To determine α, the empirical formula

$$\alpha = A \cdot p \cdot \exp\left(-\frac{B \cdot p}{|\vec{E}|}\right) \tag{B.3}$$

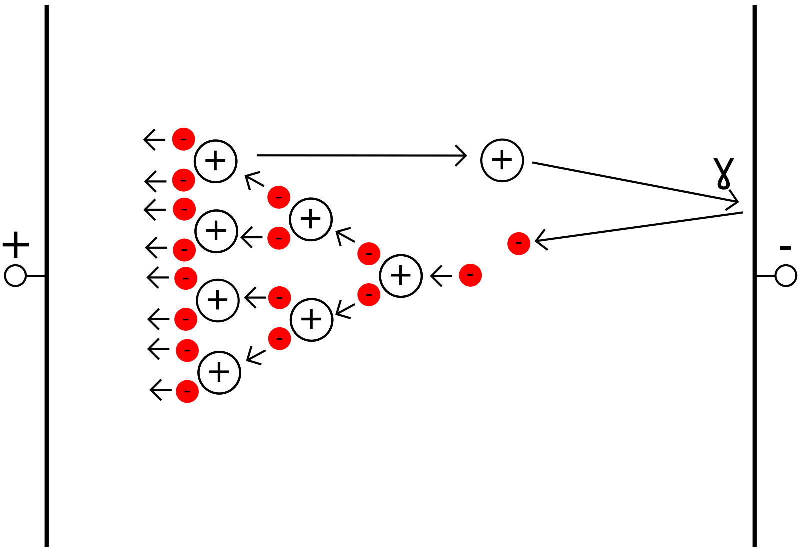

Figure B.2.: Formation of a self-sustaining discharge by an electron avalanche and secondary electron emission due to ion impact on the cathode, based on [117]. γ is the secondary electron emission coefficient.

suggested by Townsend is widely used. It contains the pressure p, the electric field norm $|\vec{E}|$ and in addition two gas constants A and B that can be determined experimentally. The proportionality $\alpha \propto \exp(-1/|\vec{E}|)$ shows that the assumption of a Townsend's coefficient that is independent from x is valid only if $|\vec{E}|$ is constant over x. Thus, the range of electrode configurations that can be investigated with this simplification is limited to large parallel plates. This case also allows the simplification of $\tilde{N} = \tilde{N}_0 \cdot \exp(\int_{x_\mathrm{a}}^{x_\mathrm{b}} \alpha \cdot \mathrm{d}x)$ to $\tilde{N} = \tilde{N}_0 \cdot \exp(\alpha \cdot d)$.

Secondary processes to enable a self-sustaining discharge

Processes that appear as a consequence of the electron impact ionization (the primary process) are called secondary processes. More precisely, the particles generated by the primary process (ions and electrons) get involved in events seen as secondary processes. A notable secondary process at lower pressure is electron emission from the cathode by electron impact, at higher pressure this process is less important. Other electrode emission processes at the cathode, e.g. photo-electric emission, can still occur [82]. To describe the efficiency of secondary emission processes at the cathode, the coefficient γ is used. The number of secondary electrons produced as a consequence of an electron avalanche is $\gamma \cdot \left(\tilde{N} - \tilde{N}_0\right)$, where $\tilde{N} - \tilde{N}_0$ is the number of positive ions generated in the avalanche, which equals the number of generated electrons. To establish a self-sustaining discharge, the secondary electron emission needs to generate at least the amount of electrons that was present in prior to the initial avalanche, i.e.

$$\gamma \cdot (\tilde{N} - \tilde{N}_0) \geq \tilde{N}_0 \tag{B.4}$$

needs to be fulfilled [118]. This is illustrated in figure B.2. Now, equation B.2 can be inserted here, resulting in

$$\gamma \cdot \tilde{N}_0 \cdot \left(\exp\left(\int_{x_\mathrm{a}}^{x_\mathrm{b}} \alpha \cdot \mathrm{d}x \right) - 1 \right) = \tilde{N}_0 \tag{B.5}$$

to express that there are just enough secondary electrons to preserve the discharge. Rearranging equation B.5 leads to

$$\exp\left(\int_{x_\mathrm{a}}^{x_\mathrm{b}} \alpha \cdot \mathrm{d}x \right) = \frac{1}{\gamma} + 1, \tag{B.6}$$

or

$$\int_{x_\mathrm{a}}^{x_\mathrm{b}} \alpha \cdot \mathrm{d}x = \ln\left(\frac{1}{\gamma} + 1 \right). \tag{B.7}$$

Paschen's law

The threshold condition expressed in equation B.7 is also the basis to deduce Paschen's law. As a first step, the empirical formula for Townsend's coefficient B.3 is inserted into the threshold condition B.7 under the assumption of a constant electric field, i.e. $|\vec{E}| = V/d$:

$$\int_{x_\mathrm{a}}^{x_\mathrm{b}} A \cdot p \cdot \exp\left(-\frac{B \cdot p \cdot d}{V} \right) \cdot \mathrm{d}x = \ln\left(\frac{1}{\gamma} + 1 \right) \tag{B.8}$$

The bounds of integration are now set to $x_\mathrm{a} = 0$ and $x_\mathrm{b} = d$ to describe two parallel planes with the distance d. As the integrand is constant over x, after rearranging this leads to

$$V = \frac{B \cdot p \cdot d}{\ln(A \cdot p \cdot d) - \ln\left(\ln\left(\frac{1}{\gamma} + 1 \right) \right)}. \tag{B.9}$$

B.2. Streamer breakdown

The Townsend breakdown preferably occurs in low pressure-gap-width products of roughly $pd < 200\,\mathrm{Torr} \cdot \mathrm{cm}$. The discharge initiated by a Townsend breakdown manifests as a dark or glow discharge. At pd values distinctly above the mentioned range, the breakdown develops faster than expected by an explanation using the multiplication of electron avalanches through cathode emission. Thus, secondary electron emission caused by ions hitting the cathode can be neglected because the ions take too long to reach the cathode due to their inertia. A theory that describes the breakdown under the named conditions very reliably is the one developed by Loeb, Meek and Raether about 1940 based on the streamer. The latter is a thin, moderately ionized channel between the electrodes.

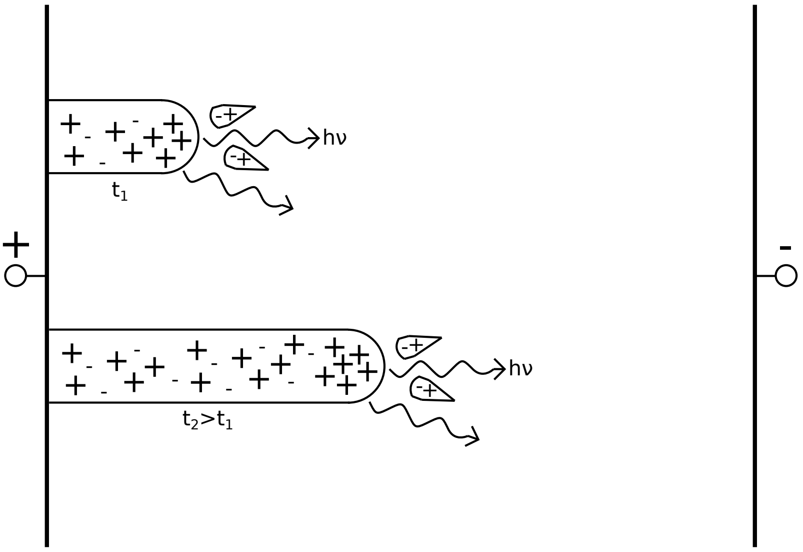

Figure B.3.: Formation of a positive streamer, based on [119].

Formation of positive streamers

Like the Townsend breakdown, the streamer breakdown begins with the formation of an electron avalanche. Thus, the term $\exp\left(\int_{x_\mathrm{a}}^{x_\mathrm{b}} \alpha \cdot \mathrm{d}x\right)$ known from equation B.2 will again occur in the following description, being denoted amplification of the avalanche. For the streamer formation, this term plays an essential role. An avalanche with a high amplification involves a considerable space charge. This is due to the fact that the highly mobile electrons form the "head" of the avalanche, whereas the positive ions remain behind and form a positively charged trail, eventually connected to the anode. Thus, the avalanche acts as a dipole forming a field opposed to the outer one. As a prerequisite to form a streamer, this field must reach about the order of the applied one. Then, subsequent avalanches will be directed to the positively charged trail rather then to the anode. The electrons of these avalanches will intermix with the positive ions and thus form a quasi-neutral conducting channel. As a result, the potential of the trail's end will be almost equalized to the one of the anode and thus form the head of the streamer. Subsequent avalanches are now directed to the streamer head, allowing the streamer to grow in direction of the cathode as shown in figure B.3.

To enable the described mechanism, there must be a process starting electron avalanches. This is given by the fact that besides ionization, the initial avalanche also causes excitation of atoms. During de-excitation, photons are emitted. This leads to photoionization in proximity of the avalanche. Thereby, additional electrons are released that initiate secondary avalanches.

Formation criterion

Starting point is an electron avalanche initiated by a single electron $N_\mathrm{e} = \exp\left(\int_{x_\mathrm{a}}^{x_\mathrm{b}} \alpha \cdot \mathrm{d}x\right)$. A positive streamer can be formed when the field of an avalanche E' is in the order of the external field E_0:

$$E' \approx E_0. \tag{B.10}$$

The former is regarded as the field on the surface of a sphere with the radius r. Thus, it is

$$E' = e_\mathrm{cgs} \cdot \tilde{N}/r^2 = e_\mathrm{cgs} \cdot r^{-2} \cdot \exp\left(\int_{x_\mathrm{a}}^{x_\mathrm{b}} \alpha \mathrm{d}x\right) \tag{B.11}$$

using the elementary charge e_cgs in $\mathrm{g}^{1/2} \cdot \mathrm{cm}^{3/2} \cdot \mathrm{s}^{-1}$. The choice of units should preserve consistency compared to Raizer [119]. Of course, the MKSA-system with $[e] = \mathrm{As}$ could be used as well, in this case the factor $1/4\pi\epsilon_0$ needs to be taken into account.

Due to the accumulation of negative charge in the avalanche's head, the drift of electrons in the field of their own space charge, i.e. their repulsion, needs to be allowed for. In general, the factor between the drift velocity of electrons v_d and its causative electric field is called electron mobility μ_e. Furthermore, the drift velocity is the temporal change of the charge sphere's radius:

$$v_\mathrm{d} = \frac{\mathrm{d}r}{\mathrm{d}t} = \mu_\mathrm{e} \cdot E'. \tag{B.12}$$

Combining equations B.11 and B.12 leads to

$$\mu_\mathrm{e} \cdot E' = \mu_\mathrm{e} \cdot e_\mathrm{cgs} \cdot r^{-2} \cdot \exp\left(\int_{x_\mathrm{a}}^{x_\mathrm{b}} \alpha \mathrm{d}x\right) \tag{B.13}$$

and with equation B.10 to

$$E' = e_\mathrm{cgs} \cdot r^{-2} \cdot \exp\left(\int_{x_\mathrm{a}}^{x_\mathrm{b}} \alpha \mathrm{d}x\right) \approx E_0. \tag{B.14}$$

Combining equations B.12 and B.13

$$r^2 \cdot \mathrm{d}r = \mu_\mathrm{e} \cdot e_\mathrm{cgs} \cdot r^{-2} \cdot \exp\left(\int_{x_\mathrm{a}}^{x_\mathrm{b}} \alpha \mathrm{d}x\right) \cdot \mathrm{d}t \tag{B.15}$$

is the basis to deduce r. This can be done by regarding the motion of the avalanche over time $x = v_\mathrm{d} \cdot t = \mu_\mathrm{e} \cdot E_0 \cdot t$ and integrating equation B.15. This results in

$$r = \left(\frac{3 \cdot e_\mathrm{cgs}}{\alpha \cdot E_0}\right)^{1/3} \cdot \exp\left(\frac{\int_{x_\mathrm{a}}^{x_\mathrm{b}} \alpha \cdot \mathrm{d}x}{3}\right). \tag{B.16}$$

As a rule of thumb, an $\alpha \cdot d \approx 18...20$ (i.e. $\exp(\alpha d) \approx 10^8$) in a constant electric field enables a streamer formation. This is also known as the simplified Meek breakdown condition [82].

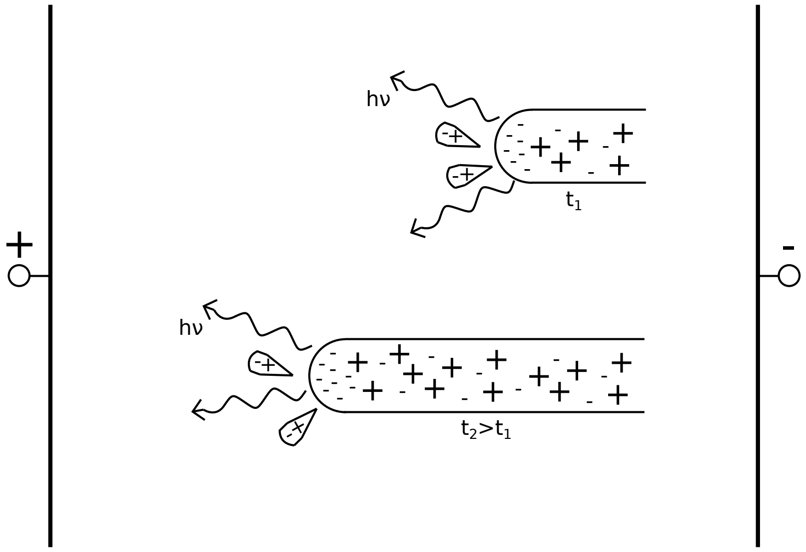

Figure B.4.: Formation of a negative streamer, based on [119].

Formation of negative streamers

A streamer formation is possible also beginning in between the electrodes. This allows negative streamers, i.e. streamers directed to the anode, to be formed as well. This happens when secondary avalanches, e.g. by photoionization, are formed in front of a sufficiently strong electron avalanche. The initial avalanche will then join the ionic trails of the secondary ones and form a plasma as shown in figure B.4.

Bibliography

[1] F. Klemm, *Geschichte der Technik.* B. G. Teubner Stuttgart Leipzig, 2013.

[2] J. Osterhammel, *Die Verwandlung der Welt.* C. H. Beck, 2009.

[3] T. McNichol, *AC/DC.* John Wiley & Sons, 2006.

[4] A. Maddison, *The World Economy: Historical Statistics (Development Centre Studies).* Organization for Economic Cooperation and Development, 2004.

[5] P. C. V. Pettenkofer, "ON CHOLERA, WITH REFERENCE TO THE RECENT EPIDEMIC AT HAMBURG.," *The Lancet*, vol. 140, pp. 1182–1185, Nov. 1892.

[6] Black & Veatch Corporation, *White's Handbook of Chlorination and Alternative Disinfectants.* Wiley, 2010.

[7] U. Kogelschatz, B. Eliasson, and W. Egli, "Dielectric-Barrier Discharges. Principle and Applications," *Le Journal de Physique IV*, vol. 07, pp. C4–47–C4–66, Oct. 1997.

[8] U. Kogelschatz, "Advanced Ozone Generation," in *Process Technologies for Water Treatment*, pp. 87–118, Springer US, 1988.

[9] W. Siemens, "Ueber die elektrostatische Induction und die Verzögerung des Stroms in Flaschendrähten," in *Wissenschaftliche und Technische Arbeiten*, pp. 82–127, Springer Berlin Heidelberg, 1889.

[10] C. F. Schönbein, "Beobachtungen über den bei der Elektrolysation des Wassers und dem Ausströmen der gewöhnlichen Elektricität aus Spitzen sich entwickelnden Geruch," *Annalen der Physik und Chemie*, vol. 126, no. 8, pp. 616–635, 1840.

[11] U. Kogelschatz, "Dielectric-Barrier Discharges: Their History, Discharge Physics, and Industrial Applications," *Plasma Chemistry and Plasma Processing*, vol. 23, no. 1, pp. 1–46, 2003.

[12] H. Becker, "Über die Extrapolation und Berechnung der Konzentration und Ausbeute von Ozonapparaten," in *Wissenschaftliche Veröffentlichungen aus dem Siemens-Konzern*, pp. 76–106, Springer Berlin Heidelberg, 1922.

[13] K. Buss, "Die elektrodenlose Entladung nach Messung mit dem Kathodenoszillographen," *Archiv für Elektrotechnik*, vol. 26, pp. 261–265, Apr. 1932.

[14] T. C. Manley, “The Electric Characteristics of the Ozonator Discharge,” *Transactions of The Electrochemical Society*, vol. 84, no. 1, p. 83, 1943.

[15] Y. Zhang, X. Liang, J. Li, and L. Wei, “Numerical Investigation on the Electrical Characteristics and Electron Energy Transformation of Pulsed Dielectric Barrier Discharge for Ozone Generation,” *IEEE Transactions on Plasma Science*, vol. 46, pp. 103–109, Jan. 2018.

[16] R. Bansemer, A. Schmidt-Bleker, U. van Rienen, and K.-D. Weltmann, “Investigation and control of the O_3- to NO-transition in a novel sub-atmospheric pressure dielectric barrier discharge,” *Plasma Sources Science and Technology*, vol. 26, p. 065005, May 2017.

[17] R. Brandenburg, “Dielectric barrier discharges: progress on plasma sources and on the understanding of regimes and single filaments,” *Plasma Sources Science and Technology*, vol. 26, p. 053001, Mar. 2017.

[18] S. Pekárek, “Experimental Study of Nitrogen Oxides and Ozone Generation by Corona-Like Dielectric Barrier Discharge with Airflow in a Magnetic Field,” *Plasma Chemistry and Plasma Processing*, vol. 37, pp. 1313–1330, July 2017.

[19] K. Nassour, M. Brahami, S. Nemmich, N. Hammadi, N. Zouzou, and A. Tilmatine, “New Hybrid Surface–Volume Dielectric Barrier Discharge Reactor for Ozone Generation,” *IEEE Transactions on Industry Applications*, vol. 53, pp. 2477–2484, May 2017.

[20] G. Vezzu, J. L. Lopez, A. Freilich, and K. H. Becker, “Optimization of Large-Scale Ozone Generators,” *IEEE Transactions on Plasma Science*, vol. 37, pp. 890–896, June 2009.

[21] V. I. Gibalov and G. J. Pietsch, “The development of dielectric barrier discharges in gas gaps and on surfaces,” *Journal of Physics D: Applied Physics*, vol. 33, pp. 2618–2636, Sept. 2000.

[22] F. Massines, N. Gherardi, N. Naudé, and P. Ségur, “Recent advances in the understanding of homogeneous dielectric barrier discharges,” *The European Physical Journal Applied Physics*, vol. 47, p. 22805, Apr. 2009.

[23] K. H. Becker, U. Kogelschatz, K. H. Schoenbach, and R. J. Barker, *Non-Equilibrium Air Plasmas at Atmospheric Pressure (Series in Plasma Physics)*. CRC Press, 2004.

[24] U. Kogelschatz, B. Eliasson, and W. Egli, “From ozone generators to flat television screens: history and future potential of dielectric-barrier discharges,” *Pure and Applied Chemistry*, vol. 71, Jan. 1999.

[25] W. P. Menashi, “Treatment of surfaces,” May 1968. US Patent 3,383,163.

[26] T. von Woedtke, H.-R. Metelmann, and K.-D. Weltmann, “Clinical Plasma Medicine: State and Perspectives of *in Vivo* Application of Cold Atmospheric Plasma,” *Contributions to Plasma Physics*, vol. 54, pp. 104–117, Feb. 2014.

[27] D. B. Graves, “Low temperature plasma biomedicine: A tutorial review,” *Physics of Plasmas*, vol. 21, p. 080901, Aug. 2014.

[28] T. von Woedtke, S. Reuter, K. Masur, and K.-D. Weltmann, “Plasmas for medicine,” *Physics Reports*, vol. 530, pp. 291–320, Sept. 2013.

[29] K.-D. Weltmann, M. Polak, K. Masur, T. von Woedtke, J. Winter, and S. Reuter, “Plasma Processes and Plasma Sources in Medicine,” *Contributions to Plasma Physics*, vol. 52, pp. 644–654, Aug. 2012.

[30] G. Y. Park, S. J. Park, M. Y. Choi, I. G. Koo, J. H. Byun, J. W. Hong, J. Y. Sim, G. J. Collins, and J. K. Lee, “Atmospheric-pressure plasma sources for biomedical applications,” *Plasma Sources Science and Technology*, vol. 21, p. 043001, June 2012.

[31] K. D. Weltmann, E. Kindel, T. von Woedtke, M. Hähnel, M. Stieber, and R. Brandenburg, “Atmospheric-pressure plasma sources: Prospective tools for plasma medicine,” *Pure and Applied Chemistry*, vol. 82, pp. 1223–1237, Apr. 2010.

[32] M. G. Kong, G. Kroesen, G. Morfill, T. Nosenko, T. Shimizu, J. van Dijk, and J. L. Zimmermann, “Plasma medicine: an introductory review,” *New Journal of Physics*, vol. 11, p. 115012, Nov. 2009.

[33] G. Fridman, G. Friedman, A. Gutsol, A. B. Shekhter, V. N. Vasilets, and A. Fridman, “Applied Plasma Medicine,” *Plasma Processes and Polymers*, vol. 5, pp. 503–533, Aug. 2008.

[34] K. Oehmigen, J. Winter, M. Hähnel, C. Wilke, R. Brandenburg, K.-D. Weltmann, and T. von Woedtke, “Estimation of Possible Mechanisms of Escherichia coli Inactivation by Plasma Treated Sodium Chloride Solution,” *Plasma Processes and Polymers*, vol. 8, pp. 904–913, June 2011.

[35] A. Schmidt-Bleker, J. Winter, A. Bösel, S. Reuter, and K.-D. Weltmann, “On the plasma chemistry of a cold atmospheric argon plasma jet with shielding gas device,” *Plasma Sources Science and Technology*, vol. 25, p. 015005, Dec. 2015.

[36] X. Hao, A. M. Mattson, C. M. Edelblute, M. A. Malik, L. C. Heller, and J. F. Kolb, “Nitric Oxide Generation with an Air Operated Non-Thermal Plasma Jet and Associated Microbial Inactivation Mechanisms,” *Plasma Processes and Polymers*, vol. 11, pp. 1044–1056, Aug. 2014.

[37] A. Helmke, M. Franck, D. Wandke, and W. Vioel, "Tempo-spatially Resolved Ozone Characteristics During Single-electrode Dielectric Barrier Discharge (SE-DBD) Operation against Metal and Porcine Skin Surfaces," *Plasma Medicine*, vol. 4, no. 1-4, pp. 67–77, 2014.

[38] G. Morfill and W. Stolz, "Forschungs-Projekt 'Plasma-Medizin' Phase II Niedertemperatur-Argon-Plasma zur in-vivo-Sterilisation chronischer Wunden (Abschlussbericht)," tech. rep., Max-Planck Institut für Extraterrestrische Physik, München, 2013.

[39] J. S. Sousa, G. Bauville, and V. Puech, "Arrays of microplasmas for the controlled production of tunable high fluxes of reactive oxygen species at atmospheric pressure," *Plasma Sources Science and Technology*, vol. 22, p. 035012, May 2013.

[40] A. B. Shekhter, V. A. Serezhenkov, T. G. Rudenko, A. V. Pekshev, and A. F. Vanin, "Beneficial effect of gaseous nitric oxide on the healing of skin wounds," *Nitric Oxide*, vol. 12, pp. 210–219, June 2005.

[41] M. J. Pavlovich, D. S. Clark, and D. B. Graves, "Quantification of air plasma chemistry for surface disinfection," *Plasma Sources Science and Technology*, vol. 23, p. 065036, Oct. 2014.

[42] F. Girard, V. Badets, S. Blanc, K. Gazeli, L. Marlin, L. Authier, P. Svarnas, N. Sojic, F. Clément, and S. Arbault, "Formation of reactive nitrogen species including peroxynitrite in physiological buffer exposed to cold atmospheric plasma," *RSC Advances*, vol. 6, no. 82, pp. 78457–78467, 2016.

[43] P. Lukes, E. Dolezalova, I. Sisrova, and M. Clupek, "Aqueous-phase chemistry and bactericidal effects from an air discharge plasma in contact with water: evidence for the formation of peroxynitrite through a pseudo-second-order post-discharge reaction of H_2O_2 and HNO_2," *Plasma Sources Science and Technology*, vol. 23, p. 015019, Feb. 2014.

[44] M. J. Traylor, M. J. Pavlovich, S. Karim, P. Hait, Y. Sakiyama, D. S. Clark, and D. B. Graves, "Long-term antibacterial efficacy of air plasma-activated water," *Journal of Physics D: Applied Physics*, vol. 44, p. 472001, Nov. 2011.

[45] K. Oehmigen, M. Hähnel, R. Brandenburg, C. Wilke, K.-D. Weltmann, and T. von Woedtke, "The Role of Acidification for Antimicrobial Activity of Atmospheric Pressure Plasma in Liquids," *Plasma Processes and Polymers*, vol. 7, pp. 250–257, Mar. 2010.

[46] S. Arndt, A. Schmidt, S. Karrer, and T. von Woedtke, "Comparing two different plasma devices kINPen and Adtec SteriPlas regarding their molecular and cellular effects on wound healing," *Clinical Plasma Medicine*, vol. 9, pp. 24–33, Mar. 2018.

[47] T. Kisch, S. Schleusser, A. Helmke, K. L. Mauss, E. T. Wenzel, B. Hasemann, P. Mailaender, and R. Kraemer, “The repetitive use of non-thermal dielectric barrier discharge plasma boosts cutaneous microcirculatory effects,” *Microvascular Research*, vol. 106, pp. 8–13, July 2016.

[48] O. Lademann, A. Kramer, H. Richter, A. Patzelt, M. C. Meinke, V. Czaika, K.-D. Weltmann, B. Hartmann, and S. Koch, “Skin Disinfection by Plasma-Tissue Interaction: Comparison of the Effectivity of Tissue-Tolerable Plasma and a Standard Antiseptic,” *Skin Pharmacology and Physiology*, vol. 24, no. 5, pp. 284–288, 2011.

[49] G. Isbary, G. Morfill, H. U. Schmidt, M. Georgi, K. Ramrath, J. Heinlin, S. Karrer, M. Landthaler, T. Shimizu, B. Steffes, W. Bunk, R. Monetti, J. L. Zimmermann, R. Pompl, and W. Stolz, “A first prospective randomized controlled trial to decrease bacterial load using cold atmospheric argon plasma on chronic wounds in patients,” *British Journal of Dermatology*, pp. no–no, Mar. 2010.

[50] “DIN SPEC 91315:2014-06, Allgemeine Anforderungen an medizinische Plasmaquellen.”

[51] C. McArdle, K. Lagan, S. Spence, and D. McDowell, “Diabetic foot ulcer wound fluid: the effects of pH on DFU bacteria and infection,” *Journal of Foot and Ankle Research*, vol. 8, Apr. 2015.

[52] G. Gethin, “The significance of surface pH in chronic wounds,” *Wounds UK*, 2007.

[53] M. Dünnbier, A. Schmidt-Bleker, J. Winter, M. Wolfram, R. Hippler, K.-D. Weltmann, and S. Reuter, “Ambient air particle transport into the effluent of a cold atmospheric-pressure argon plasma jet investigated by molecular beam mass spectrometry,” *Journal of Physics D: Applied Physics*, vol. 46, p. 435203, Oct. 2013.

[54] A. Schmidt-Bleker, J. Winter, S. Iseni, M. Dünnbier, K.-D. Weltmann, and S. Reuter, “Reactive species output of a plasma jet with a shielding gas device—combination of FTIR absorption spectroscopy and gas phase modelling,” *Journal of Physics D: Applied Physics*, vol. 47, p. 145201, Mar. 2014.

[55] C. Douat, S. Hübner, R. Engeln, and J. Benedikt, “Production of nitric/nitrous oxide by an atmospheric pressure plasma jet,” *Plasma Sources Science and Technology*, vol. 25, p. 025027, Mar. 2016.

[56] S. K. Kang, H. Y. Kim, G. S. Yun, and J. K. Lee, “Portable microwave air plasma device for wound healing,” *Plasma Sources Science and Technology*, vol. 24, p. 035020, June 2015.

[57] P. J. Bruggeman, M. J. Kushner, B. R. Locke, J. G. E. Gardeniers, W. G. Graham, D. B. Graves, R. C. H. M. Hofman-Caris, D. Maric, J. P. Reid, E. Ceriani, D. F. Rivas, J. E. Foster, S. C. Garrick, Y. Gorbanev, S. Hamaguchi, F. Iza, H. Jablonowski, E. Klimova, J. Kolb, F. Krcma, P. Lukes, Z. Machala, I. Marinov,

D. Mariotti, S. M. Thagard, D. Minakata, E. C. Neyts, J. Pawlat, Z. L. Petrovic, R. Pflieger, S. Reuter, D. C. Schram, S. Schröter, M. Shiraiwa, B. Tarabová, P. A. Tsai, J. R. R. Verlet, T. von Woedtke, K. R. Wilson, K. Yasui, and G. Zvereva, "Plasma-liquid interactions: a review and roadmap," *Plasma Sources Science and Technology*, vol. 25, p. 053002, Sept. 2016.

[58] Y. H. Na, N. Kumar, M.-H. Kang, G. S. Cho, E. H. Choi, G. Park, and H. S. Uhm, "Production of nitric oxide using a microwave plasma torch and its application to fungal cell differentiation," *Journal of Physics D: Applied Physics*, vol. 48, p. 195401, Mar. 2015.

[59] D. Dobrynin, K. Arjunan, A. Fridman, G. Friedman, and A. M. Clyne, "Direct and controllable nitric oxide delivery into biological media and living cells by a pin-to-hole spark discharge (PHD) plasma," *Journal of Physics D: Applied Physics*, vol. 44, p. 075201, Jan. 2011.

[60] F. Peters, J. Hirschberg, N. Mertens, S. Wieneke, and W. Viöl, "Comparison of Nitric Oxide Concentrations in µs- and ns-Atmospheric Pressure Plasmas by UV Absorption Spectroscopy," *Plasma Science and Technology*, vol. 18, pp. 406–411, Apr. 2016.

[61] D. Yuan, Z. Wang, C. Ding, Y. He, R. Whiddon, and K. Cen, "Ozone production in parallel multichannel dielectric barrier discharge from oxygen and air: the influence of gas pressure," *Journal of Physics D: Applied Physics*, vol. 49, p. 455203, Oct. 2016.

[62] R. Bansemer, A. Schmidt-Bleker, U. van Rienen, and K.-D. Weltmann, "Monitoring of a dielectric barrier discharge-based process using the gas gap voltage," *Plasma Sources Science and Technology*, vol. 28, p. 025002, Feb. 2019.

[63] E. Hering, R. Martin, and M. Stohrer, *Physik für Ingenieure.* Springer, 2008.

[64] W. Demtröder, *Experimentalphysik 3: Atome, Moleküle und Festkörper.* Springer, 2004.

[65] P. R. Griffiths and J. A. de Haseth, *Fourier Transform Infrared Spectrometry.* John Wiley + Sons, 2007.

[66] H. Günzler and H.-U. Gremlich, *IR - Spektroskopie.* Wiley VCH Verlag GmbH, 2003.

[67] I. E. Gordon, L. S. Rothman, C. Hill, R. V. Kochanov, Y. Tan, P. F. Bernath, M. Birk, V. Boudon, A. Campargue, K. V. Chance, B. J. Drouin, J.-M. Flaud, R. R. Gamache, J. T. Hodges, D. Jacquemart, V. I. Perevalov, A. Perrin, K. P. Shine, M.-A. H. Smith, J. Tennyson, G. C. Toon, H. Tran, V. G. Tyuterev, A. Barbe, A. G. Császár, V. M. Devi, T. Furtenbacher, J. J. Harrison, J.-M. Hartmann, A. Jolly, T. J. Johnson, T. Karman, I. Kleiner, A. A. Kyuberis, J. Loos,

O. M. Lyulin, S. T. Massie, S. N. Mikhailenko, N. Moazzen-Ahmadi, H. S. P. Müller, O. V. Naumenko, A. V. Nikitin, O. L. Polyansky, M. Rey, M. Rotger, S. W. Sharpe, K. Sung, E. Starikova, S. A. Tashkun, J. V. Auwera, G. Wagner, J. Wilzewski, P. Wcisło, S. Yu, and E. J. Zak, "The HITRAN2016 molecular spectroscopic database," *Journal of Quantitative Spectroscopy and Radiative Transfer*, vol. 203, pp. 3–69, Dec. 2017.

[68] R. V. Kochanov, I. E. Gordon, L. S. Rothman, P. Wcisło, C. Hill, and J. S. Wilzewski, "HITRAN Application Programming Interface (HAPI): A comprehensive approach to working with spectroscopic data," *Journal of Quantitative Spectroscopy and Radiative Transfer*, vol. 177, pp. 15–30, July 2016.

[69] S. Reuter, J. S. Sousa, G. D. Stancu, and J.-P. H. van Helden, "Review on VUV to MIR absorption spectroscopy of atmospheric pressure plasma jets," *Plasma Sources Science and Technology*, vol. 24, p. 054001, Aug. 2015.

[70] J. Röpcke, P. B. Davies, N. Lang, A. Rousseau, and S. Welzel, "Applications of quantum cascade lasers in plasma diagnostics: a review," *Journal of Physics D: Applied Physics*, vol. 45, p. 423001, Oct. 2012.

[71] J. Röpcke, G. Lombardi, A. Rousseau, and P. B. Davies, "Application of mid-infrared tuneable diode laser absorption spectroscopy to plasma diagnostics: a review," *Plasma Sources Science and Technology*, vol. 15, pp. S148–S168, Oct. 2006.

[72] J. Winter, T. M. C. Nishime, R. Bansemer, M. Balazinski, K. Wende, and K.-D. Weltmann, "Enhanced atmospheric pressure plasma jet setup for endoscopic applications," *Journal of Physics D: Applied Physics*, vol. 52, p. 024005, Nov. 2018.

[73] L. Hansen, A. Schmidt-Bleker, R. Bansemer, H. Kersten, K.-D. Weltmann, and S. Reuter, "Influence of a liquid surface on the NO_x production of a cold atmospheric pressure plasma jet," *Journal of Physics D: Applied Physics*, vol. 51, p. 474002, Sept. 2018.

[74] A. Schmidt-Bleker, R. Bansemer, S. Reuter, and K.-D. Weltmann, "How to produce an NO_x- instead of O_x-based chemistry with a cold atmospheric plasma jet," *Plasma Processes and Polymers*, vol. 13, pp. 1120–1127, Sept. 2016.

[75] D. Jacob, *Introduction to Atmospheric Chemistry.* Princeton University Press, 1999.

[76] G. J. M. Hagelaar and L. C. Pitchford, "Solving the Boltzmann equation to obtain electron transport coefficients and rate coefficients for fluid models," *Plasma Sources Science and Technology*, vol. 14, no. 4, p. 722, 2005.

[77] V. I. Gibalov and G. J. Pietsch, "Dynamics of dielectric barrier discharges in different arrangements," *Plasma Sources Science and Technology*, vol. 21, p. 024010, Apr. 2012.

[78] Y. Sakiyama, D. B. Graves, H.-W. Chang, T. Shimizu, and G. E. Morfill, “Plasma chemistry model of surface microdischarge in humid air and dynamics of reactive neutral species,” *Journal of Physics D: Applied Physics*, vol. 45, p. 425201, Oct. 2012.

[79] T. Murakami, K. Niemi, T. Gans, D. O’Connell, and W. G. Graham, “Chemical kinetics and reactive species in atmospheric pressure helium-oxygen plasmas with humid-air impurities,” *Plasma Sources Science and Technology*, vol. 22, p. 015003, Dec. 2012.

[80] P. Rajasekaran, P. Mertmann, N. Bibinov, D. Wandke, W. Viöl, and P. Awakowicz, “DBD plasma source operated in single-filamentary mode for therapeutic use in dermatology,” *Journal of Physics D: Applied Physics*, vol. 42, p. 225201, Oct. 2009.

[81] T. Shimizu, Y. Sakiyama, D. B. Graves, J. L. Zimmermann, and G. E. Morfill, “The dynamics of ozone generation and mode transition in air surface microdischarge plasma at atmospheric pressure,” *New Journal of Physics*, vol. 14, p. 103028, Oct. 2012.

[82] P. J. Bruggeman, F. Iza, and R. Brandenburg, “Foundations of atmospheric pressure non-equilibrium plasmas,” *Plasma Sources Science and Technology*, vol. 26, p. 123002, Nov. 2017.

[83] L. Niemeyer, “A generalized approach to partial discharge modeling,” *IEEE Transactions on Dielectrics and Electrical Insulation*, vol. 2, no. 4, pp. 510–528, 1995.

[84] L. Stollenwerk, S. Amiranashvili, J.-P. Boeuf, and H.-G. Purwins, “Measurement and 3D Simulation of Self-Organized Filaments in a Barrier Discharge,” *Physical Review Letters*, vol. 96, June 2006.

[85] A. V. Pipa, J. Koskulics, R. Brandenburg, and T. Hoder, “The simplest equivalent circuit of a pulsed dielectric barrier discharge and the determination of the gas gap charge transfer,” *Review of Scientific Instruments*, vol. 83, p. 115112, Nov. 2012.

[86] J. Tepper and M. Lindmayer, “Investigations on two different kinds of homogeneous barrier discharges at atmospheric pressure,” in *HAKONE VII International Symposium on High Pressure Low Temperature Plasma Chemistry*, pp. 10–13, 2000.

[87] F. J. J. Peeters and M. C. M. van de Sanden, “The influence of partial surface discharging on the electrical characterization of DBDs,” *Plasma Sources Science and Technology*, vol. 24, p. 015016, Dec. 2014.

[88] A. V. Pipa, T. Hoder, and R. Brandenburg, “On the Role of Capacitance Determination Accuracy for the Electrical Characterization of Pulsed Driven Dielectric Barrier Discharges,” *Contributions to Plasma Physics*, vol. 53, pp. 469–480, Feb. 2013.

[89] M. Archambault-Caron, H. Gagnon, B. Nisol, K. Piyakis, and M. R. Wertheimer, "Precise energy and temperature measurements in dielectric barrier discharges at atmospheric pressure," *Plasma Sources Science and Technology*, vol. 24, p. 045004, June 2015.

[90] Z. Fang, S. Ji, J. Pan, T. Shao, and C. Zhang, "Electrical Model and Experimental Analysis of the Atmospheric-Pressure Homogeneous Dielectric Barrier Discharge in He," *IEEE Transactions on Plasma Science*, vol. 40, pp. 883–891, Mar. 2012.

[91] U. N. Pal, A. K. Sharma, J. S. Soni, S. Kr, H. Khatun, M. Kumar, B. L. Meena, M. S. Tyagi, B.-J. Lee, M. Iberler, J. Jacoby, and K. Frank, "Electrical modelling approach for discharge analysis of a coaxial DBD tube filled with argon," *Journal of Physics D: Applied Physics*, vol. 42, p. 045213, Jan. 2009.

[92] A. V. Pipa, T. Hoder, J. Koskulics, M. Schmidt, and R. Brandenburg, "Experimental determination of dielectric barrier discharge capacitance," *Review of Scientific Instruments*, vol. 83, p. 075111, July 2012.

[93] H.-E. Wagner, R. Brandenburg, K. V. Kozlov, A. Sonnenfeld, P. Michel, and J. F. Behnke, "The barrier discharge: basic properties and applications to surface treatment," *Vacuum*, vol. 71, pp. 417–436, May 2003.

[94] Z. Falkenstein and J. J. Coogan, "Microdischarge behaviour in the silent discharge of nitrogen - oxygen and water - air mixtures," *Journal of Physics D: Applied Physics*, vol. 30, pp. 817–825, Mar. 1997.

[95] A. Berchtikou, J. Lavoie, V. Poenariu, B. Saoudi, R. Kashyap, and M. Wertheimer, "Thermometry in noble gas dielectric barrier discharges at atmospheric pressure using optical emission spectroscopy," *IEEE Transactions on Dielectrics and Electrical Insulation*, vol. 18, pp. 24–33, Feb. 2011.

[96] G. Nersisyan and W. G. Graham, "Characterization of a dielectric barrier discharge operating in an open reactor with flowing helium," *Plasma Sources Science and Technology*, vol. 13, pp. 582–587, Sept. 2004.

[97] N. K. Bibinov, A. A. Fateev, and K. Wiesemann, "Variations of the gas temperature in He/N_2 barrier discharges," *Plasma Sources Science and Technology*, vol. 10, pp. 579–588, Sept. 2001.

[98] A. F. H. van Gessel, B. Hrycak, M. Jasiński, J. Mizeraczyk, J. J. A. M. van der Mullen, and P. J. Bruggeman, "Temperature and NO density measurements by LIF and OES on an atmospheric pressure plasma jet," *Journal of Physics D: Applied Physics*, vol. 46, p. 095201, Jan. 2013.

[99] S. Jodzis and J. Petryk, "Gas Temperature in an Ozonizer. The Computer Modeling of an Actual Discharge System," *IEEE Transactions on Plasma Science*, vol. 39, pp. 2120–2121, Nov. 2011.

[100] J. Ozonek, S. Fijalkowski, and J. Czerwiński, "Thermodynamic Aspects of Equilibrium Ozone Generation," *Plasma Processes and Polymers*, vol. 4, pp. 701–709, Oct. 2007.

[101] E. Jones, T. Oliphant, P. Peterson, *et al.*, "SciPy: Open source scientific tools for Python," 2001–. [Online; accessed 08$^{\text{th}}$ July, 2018].

[102] A. Meurer, C. P. Smith, M. Paprocki, O. Čertík, S. B. Kirpichev, M. Rocklin, A. Kumar, S. Ivanov, J. K. Moore, S. Singh, T. Rathnayake, S. Vig, B. E. Granger, R. P. Muller, F. Bonazzi, H. Gupta, S. Vats, F. Johansson, F. Pedregosa, M. J. Curry, A. R. Terrel, v. Roučka, A. Saboo, I. Fernando, S. Kulal, R. Cimrman, and A. Scopatz, "SymPy: symbolic computing in Python," *PeerJ Computer Science*, vol. 3, p. e103, Jan. 2017.

[103] W. B. DeMore, S. P. Sander, D. M. Golden, R. F. Hampson, M. J. Kurylo, C. J. Howard, A. R. Ravishankara, C. E. Kolb, and M. J. Molina, "Chemical Kinetics and Photochemical Data for Use in Stratospheric Modeling. Evaluation No. 12," *NASA Technical Report*, 1997.

[104] R. Atkinson, D. L. Baulch, R. A. Cox, R. F. Hampson, J. A. Kerr, M. J. Rossi, and J. Troe, "Evaluated Kinetic and Photochemical Data for Atmospheric Chemistry: Supplement VI. IUPAC Subcommittee on Gas Kinetic Data Evaluation for Atmospheric Chemistry," *Journal of Physical and Chemical Reference Data*, vol. 26, pp. 1329–1499, Nov. 1997.

[105] R. Atkinson, D. L. Baulch, R. A. Cox, J. N. Crowley, R. F. Hampson, R. G. Hynes, M. E. Jenkin, M. J. Rossi, and J. Troe, "Evaluated kinetic and photochemical data for atmospheric chemistry: Volume I - gas phase reactions of O_x, HO_x, NO_x and SO_x species," *Atmospheric Chemistry and Physics*, vol. 4, pp. 1461–1738, Sept. 2004.

[106] H. Hippler, R. Rahn, and J. Troe, "Temperature and pressure dependence of ozone formation rates in the range 1–1000 bar and 90–370 K," *The Journal of Chemical Physics*, vol. 93, pp. 6560–6569, Nov. 1990.

[107] L. Liu and M. Becerra, "Gas heating dynamics during leader inception in long air gaps at atmospheric pressure," *Journal of Physics D: Applied Physics*, vol. 50, p. 345202, Aug. 2017.

[108] D. L. Baulch, C. J. Cobos, R. A. Cox, P. Frank, G. Hayman, T. Just, J. A. Kerr, T. Murrells, M. J. Pilling, J. Troe, R. W. Walker, and J. Warnatz, "Evaluated Kinetic Data for Combustion Modeling. Supplement I," *Journal of Physical and Chemical Reference Data*, vol. 23, pp. 847–848, Nov. 1994.

[109] A. Pogoda, "Etablierung von absorptionsspektrometrischen Methoden zur Untersuchung einer aerosolbetriebenen Plasmaquelle," Master's thesis, Universität Greifswald, 2019.

[110] J. H. Spurk and N. Aksel, *Strömungslehre: Einführung in die Theorie der Strömungen (Springer-Lehrbuch) (German Edition).* Springer, 2005.

[111] COMSOL, Inc, https://www.comsol.com, *CFD Module User's Guide, version 4.3a*, Oct. 2012.

[112] R. Brandenburg, Z. Navrátil, J. Jánský, P. St'ahel, D. Trunec, and H.-E. Wagner, "The transition between different modes of barrier discharges at atmospheric pressure," *Journal of Physics D: Applied Physics*, vol. 42, p. 085208, Apr. 2009.

[113] R. Schwarze, *CFD-Modellierung.* Springer-Verlag GmbH, 2012.

[114] A. Bondeson, T. Rylander, and P. Ingelström, *Computational Electromagnetics (Texts in Applied Mathematics).* Springer, 2005.

[115] J. Rotta, "Experimenteller Beitrag zur Entstehung turbulenter Strömung im Rohr," *Ingenieur-Archiv*, vol. 24, no. 4, pp. 258–281, 1956.

[116] A. Bejan, *Convection Heat Transfer.* Wiley, 2004.

[117] O. Guaitella, "Dielectric Barrier and Corona Discharges," in *International School on Low Temperature Plasma Physics*, 2016.

[118] N. S. J. Braithwaite, "Introduction to gas discharges," *Plasma Sources Science and Technology*, vol. 9, no. 4, p. 517, 2000.

[119] Y. P. Raizer, *Gas Discharge Physics.* Springer-Verlag Berlin Heidelberg, 1991.